

SANDIA REPORT

SAND2012-7644

Unlimited Release

Printed December 2012

Final Report on Reliability and Lifetime Prediction

Ken Gillen, Jonathan Wise, Gary Jones, Al Causa, Ed Terrill, and Marc Borowczak

Prepared by
Sandia National Laboratories
Albuquerque, New Mexico 87185 and Livermore, California 94550

Sandia National Laboratories is a multi-program laboratory managed and operated by Sandia Corporation, a wholly owned subsidiary of Lockheed Martin Corporation, for the U.S. Department of Energy's National Nuclear Security Administration under contract DE-AC04-94AL85000.

Approved for public release; further dissemination unlimited.

Note: This report was originally prepared in 1999 under a CRADA agreement with Goodyear. It was issued as SAND99-0465 and was restricted from open distribution under a 5 year CRADA protection clause. The report was approved for unlimited public release in December 2012.



Sandia National Laboratories

Issued by Sandia National Laboratories, operated for the United States Department of Energy by Sandia Corporation.

NOTICE: This report was prepared as an account of work sponsored by an agency of the United States Government. Neither the United States Government, nor any agency thereof, nor any of their employees, nor any of their contractors, subcontractors, or their employees, make any warranty, express or implied, or assume any legal liability or responsibility for the accuracy, completeness, or usefulness of any information, apparatus, product, or process disclosed, or represent that its use would not infringe privately owned rights. Reference herein to any specific commercial product, process, or service by trade name, trademark, manufacturer, or otherwise, does not necessarily constitute or imply its endorsement, recommendation, or favoring by the United States Government, any agency thereof, or any of their contractors or subcontractors. The views and opinions expressed herein do not necessarily state or reflect those of the United States Government, any agency thereof, or any of their contractors.

Printed in the United States of America. This report has been reproduced directly from the best available copy.

Available to DOE and DOE contractors from

U.S. Department of Energy
Office of Scientific and Technical Information
P.O. Box 62
Oak Ridge, TN 37831

Telephone: (865) 576-8401
Facsimile: (865) 576-5728
E-Mail: reports@adonis.osti.gov
Online ordering: <http://www.osti.gov/bridge>

Available to the public from

U.S. Department of Commerce
National Technical Information Service
5285 Port Royal Rd.
Springfield, VA 22161

Telephone: (800) 553-6847
Facsimile: (703) 605-6900
E-Mail: orders@ntis.fedworld.gov
Online order: <http://www.ntis.gov/help/ordermethods.asp?loc=7-4-0#online>



SAND2012-7644
Unlimited Release
Printed December 2012

Final Report on Reliability and Lifetime Prediction

Ken Gillen
Organic Materials Aging and Reliability Department

Jonathan Wise
Proliferation Sciences Department

Gary Jones
Electronic and Optical Materials Department

Sandia National Laboratories
P.O. Box 5800
Albuquerque, New Mexico 87185-MS1407

Al Causa, Ed Terrill and Marc Borowczak

The Goodyear Tire and Rubber Co.
Goodyear Technical Center
1376 Tech Way Drive
Akron, OH 44316

Abstract

This document highlights the important results obtained from the subtask of the Goodyear CRADA devoted to better understanding reliability of tires and to developing better lifetime prediction methods. The overall objective was to establish the chemical and physical basis for the degradation of tires using standard as well as unique models and experimental techniques. Of particular interest was the potential application of our unique modulus profiling apparatus for assessing tire properties and for following tire degradation. During the course of this complex investigation, extensive relevant information was generated, including experimental results, data analyses and development of models and instruments. Detailed descriptions of the findings are included in this report.

CONTENTS

ABSTRACT	1
INTRODUCTION.....	5
EXPERIMENTAL	5
Samples.....	5
Oven Aging	6
Tensile Tests.....	6
Oxygen Permeability	6
Automated Modulus Profiling.....	6
Oxygen Consumption Measurements	6
Oxygen Content Measurements.....	7
Dynamic Oxygen Consumption	7
Micrometer Resolution Interfacial Force Microscopy (IFM).....	7
RESULTS AND DISCUSSION	7
Tensile Tests on Materials 145-148 and 150A.....	7
Modulus Profiles on Materials 145-148 and 150A.....	9
Oxygen Consumption Measurements	12
Arrhenius Analyses of the Shift Factors	14
DLO Modeling of Sheets	14
Oxygen Permeability Measurements	16
DLO Modeling of Sheets of Materials 145-150	18
Solubility Coefficient Estimates	20
DLO Modeling of Laminates	23
Oxygen Content Measurements.....	26
Modulus Profiles on Tires.....	26
Construction & Delivery of Automated Modulus Profiler	28
Construction of Dynamic Oxygen Consumption Apparatus	29
Micrometer Resolution Interfacial Force Microscopy (IFM).....	32
CONCLUSIONS.....	34
ACKNOWLEDGMENTS	37
REFERENCES.....	37
FIGURES	39
APPENDIX 1- GC Procedures for Oxygen Consumption.....	93
APPENDIX 2- Lamx2 software to calculate laminate oxidation profiles....	103
APPENDIX 3- Notes and Block diagram for Modulus Profiler.....	109

TABLES

1 Nominal material compositions	5
2 Empirical shift factors for elongation data	9
3 Unaged modulus results for Material 148	11
4 Unaged modulus results for Materials 145, 146 and 147	11
5 Estimates of O₂ consumption rates & O₂ permeability coefficients	19
6 estimates of the parameter α assuming $\beta = 5$.....	19
7 Time-dependent flux data for an EPDM material at 51°C.....	21
8 Solubility coefficients for Materials 145-150.....	22
9 Parameters input into lamx2 program for 95°C aging of laminate.....	24
10 Parameters input into lamx2 program for 100°C aging of larger tire.....	25
11 Parameters input into lamx2 program for 70°C aging of smaller tire	25
12 Approximate width of apex region.....	28
13 Dynamic versus static results for 40 mil samples of Material 154.....	31

-This page intentionally left blank-

INTRODUCTION

This document highlights the important results obtained from the subtask of the Goodyear CRADA devoted to better understanding reliability of tires and to developing better lifetime prediction methods. The overall objective was to establish the chemical and physical basis for the degradation of tires using standard as well as unique models and experimental techniques. Of particular interest was the potential application of our unique modulus profiling apparatus for assessing tire properties and for following tire degradation. During the course of this complex investigation, extensive information was generated, including experimental results, data analyses and development of models and instruments. The purpose of this report is to summarize the most important aspects of the work. Some of the work was carried out using a combination of the Goodyear CRADA funds and funds from the Enhanced Surveillance Program (ESP). Examples include the development of the ultrasensitive oxygen consumption technique, the improved oxygen permeability capability and the construction of an interfacial force microscope (IFM) capable of mapping mechanical properties with micrometer resolution. These and other joint developments therefore benefited and will continue to benefit the weapon programs as well as American industry in a synergistic manner.

EXPERIMENTAL

Samples

Various rubber compound samples were used in this program, including compression molded sheets of proprietary tire rubber formulations, special composite laminates made from several of these formulations stacked together, and cross-sectional pieces from various locations of new, laboratory-aged and field-aged automobile and truck tires. The compression molded sheet materials were labeled with numbers from 145 to 154 with their general compositions shown in Table 1. For several of the materials, more than one batch was received; for instance, 145 and 145B were different batches of a supposedly identical formulation.

Table 1. Nominal material compositions

Material	Base Polymer Composition
145, 145B	Natural rubber (100)
146, 146B	Natural rubber/ SBR (70/30)
147, 147B	Natural rubber (100)
148, 148B	Natural rubber/ cis polybutadiene (50/50)
149	Halobutyl rubber (100)
150A	SBR/ cis polybutadiene (70/30)
153	Natural rubber/ cis polybutadiene (40/60)
154	Natural rubber (100)

Oven Aging

Oven aging of the tensile samples and the oxygen consumption containers was carried out in air-circulating ovens ($\pm 1^\circ\text{C}$) equipped with thermocouples connected to continuous strip chart recorders.

Tensile Tests

Tensile tests as functions of aging (time and temperature) were done on approximately 0.2-cm thick samples of compounds 145, 146, 147, 148 and 150A and on approximately 0.08 cm thick samples of compound 145. Before oven aging, strips approximately 6 mm wide by ~150 mm long were cut from the compression molded sheets. Tensile testing (12.7 cm/min strain rate, 5.1 cm initial jaw separation) was performed using an Instron model 1000 testing machine equipped with pneumatic grips and having an extensometer clamped to the sample. This technique gave values of the ultimate tensile elongation, e , and the tensile strength at break, the latter reported as the value normalized to the unaged tensile strength at break.

Oxygen Permeability

Oxygen permeation measurements were performed on an Oxtran-100 coulometric permeation apparatus (Modern Controls, Inc., Minneapolis, MN, USA), which is based on ASTM Standard D3985-81. Several modifications, the most important of which was placing the sample holder in an oven, have been made to this instrument to permit data acquisition at higher temperatures (up to $\sim 95^\circ\text{C}$ for the present studies) with minimal temperature gradients (less than $\pm 0.5^\circ\text{C}$) across the sample during the experiment. Details on our new approach for obtaining oxygen permeability coefficients at high temperatures in the presence of important oxygen consumption contributions will be given in the Results and Discussion section below. This approach and the equipment modifications necessary for high temperature measurements were partially funded by both this CRADA and the Enhanced Surveillance Program.

Automated Modulus Profiling

Modulus profiles with a resolution of $\sim 50\ \mu\text{m}$ were obtained on sample cross-sections using our modulus profiling apparatus, which has been described in detail previously [1-2]. This instrument measures inverse tensile compliance, which is closely related to the tensile modulus. A computer-controlled, automated version of this apparatus was developed for this CRADA. Details on this accomplishment will be given below in the Results and Discussion section.

Oxygen Consumption Measurements

This technique monitors the change in oxygen content caused by reaction with polymer in sealed containers using gas chromatographic detection. Since the development of the

approach was partially funded by this CRADA (jointly with the Enhanced Surveillance Program), details will be given later in the Results and Discussion section.

Oxygen Content Measurements

Oxygen content was determined as a function of radial position across the crown of the tire. Slices were prepared with Fortuna rubber slicing instrument. In rubber components containing wires, slices were prepared with a scalpel. The slice depths (profile positions) were determined with calipers. Within each slice, five samples were taken. The oxygen content data for each slice is an average of the five measurements. The typical confidence level is +/- 5%.

Oxygen content was measured with a LECO Oxygen Determinator (Model # RO-478). A sample of rubber about 2 milligram is charged into the furnace chamber and consumed at high temperature (1200°C) under nitrogen. The nitrogen sweeps the off-gases through a calibrated IR detector, which detects CO and CO₂. The analysis determines the total molecular oxygen from the organic compounds in the rubber. Inorganic portions of the rubber compound remain in the furnace as ash. An increase in oxygen content of an aged rubber compound would be a measure of oxidation.

Dynamic Oxygen Consumption

Since tires are deformed dynamically during the time when the bulk of the oxidative degradation occurs, it would be useful to determine whether dynamic cycling during aging increases the oxygen consumption rate relative to static aging conditions. An apparatus capable of achieving this goal as well as having the capability of dynamically aging materials in rigorously anaerobic conditions, was developed for this program. Details on this apparatus and its capabilities will be given below in the Results and Discussion section.

Micrometer Resolution Interfacial Force Microscopy (IFM)

Since modulus profiling (50- μm resolution) proved extremely useful for studying the aging of tires and tire materials, it was concluded that having the capability of monitoring mechanical properties with even better resolution could lead to even more useful results. With this in mind, we began a program whose first goal was to produce an instrument based on building a modified IFM, capable of mapping mechanical properties of materials with resolution of around 1-5 μm . The status of this work will be reviewed in the Results and Discussion section below.

RESULTS AND DISCUSSION

Tensile Tests on Materials 145-148 and 150A

Materials 145-148 and 150A were aged in air-circulating ovens for various times at three different temperatures (80°C, 95°C and 110°C). Typically, three samples were removed

after each aging condition and subjected to tensile testing. Figures 1-6 show the ultimate tensile elongation results for the six materials (both 0.08 mm and 0.2 mm thick samples of 145 were examined). As is often found, the elongation for all six materials drops monotonically with time under all three temperature conditions.

The conventional approach for making predictions from accelerated thermal aging experiments is to obtain an estimate of the failure time or the time to a certain amount of degradation at each accelerated temperature, and then to analyze the results with the so-called Arrhenius model [3]. This model is based on the fact that simple chemical reactions usually have Arrhenius temperature dependence. That is, the reaction rate constant k is given by

$$k = A \exp\left[\frac{-E_a}{RT}\right] \quad (1)$$

where A is a constant pre-exponential factor, R is the gas constant, T is the absolute temperature and E_a is the Arrhenius activation energy. Since the time to a certain amount of damage is inversely related to the rate constant, a plot of the log of this time versus the inverse absolute temperature would be predicted to be linear with the Arrhenius activation energy available from the slope. If the results do indeed give linear behavior and predictions at temperatures lower than the experimental temperature range are desired, one can then extrapolate the Arrhenius functionality (although with no guarantee that the slope (E_a) will remain constant).

There are a number of potential problems with the Arrhenius approach, many of which have been previously pointed out [3]. Most importantly, although a single simple chemical reaction might be described by the relationship given in eq. (1), it is easy to show that, in general, the more complex kinetic reaction schemes appropriate to polymer degradation can have effective activation energies that change with temperature [3].

In the typical Arrhenius analysis, only one data point per temperature (e.g., the failure time) is used. The time-temperature superposition approach [3,4], on the other hand, uses the complete data set to test the Arrhenius or other acceleration models. In this approach, we select the lowest temperature as the reference temperature, T_{ref} . If raising the temperature to a higher temperature T equally accelerates all of the reactions underlying a given degradation variable, then the time decay of the degradation parameter will be accelerated by a constant multiplicative shift factor, a_T . If constant acceleration occurs, the shape of the degradation curves will be the same when plotted versus the logarithm of the aging time. For this reason, we plotted the temperature-dependent results for elongation in Figs. 1-6 versus log of the aging time. A quick glance at these plots indicates that, indeed, for each of the six materials, the shapes of the degradation curves are quite similar as the aging temperature is changed, which offers evidence for the accelerated aging assumption of a constant acceleration in all important degradation reactions.

The time-temperature superposition approach involves empirically finding the multiplicative shift factor that shifts each higher-temperature set of data onto the data set at the reference temperature, such that the best overlap (superposition) of the data occurs. This procedure was applied to the six sets of data, giving the superposed results shown in Figs. 7-12. It is clear from the results that quite good superposition occurs for all six materials, which is not surprising given the constancy of degradation shapes observed for the raw data when plotted versus log time. Table 2 lists the empirical shift factors found for the six materials at 95°C and 110°C (at the reference temperature of 80°C, the shift factor a_T is equal to unity by definition). It is interesting to note that the shift factors for all six materials are quite similar, implying that the temperature dependence of degradation is similar for materials 145-148 and 150, in spite of the differences in formulation (Table 1).

Table 2. Empirical shift factors for elongation data ($a_T = 1$ at 80°C)

Material	a_T at 95°C	a_T at 110°C
145- thick	3.6	14.5
145- thin	3.5	14.5
146	3.6	15
147	3.15	15
148	3.35	13.5
150	3.7	14.5

The normalized tensile strength data for these materials is time-temperature superposed in Figs. 13-18. Given the larger scatter in tensile strength values, the shift factors empirically determined for the elongation results were used for these plots. Superposition appears to be reasonable for materials 148, 150 and the thin samples of 145 although the large scatter in the data clouds this conclusion. For the thick samples of 145 plus material 146 and 147, there is some evidence that the higher temperature results at 110°C give slightly lower tensile strength values at long times.

Modulus Profiles on Materials 145-148 and 150A

Our modulus profiling apparatus [1,2] allows us to quantitatively map modulus values on a cross-sectional face of degraded samples with a spatial resolution of ~ 50 μm . Modulus profiles were run on many of the samples that were oven-aged for the tensile property experiments. Figures 19-33 show modulus profile results for Materials 145-148 and 150A at the three oven aging temperatures of 111°C, 95°C and 80°C. The figures plot modulus values versus the cross-sectional position, where P represents the percentage of the distance from one air-exposed surface of the sample to the opposite air-exposed surface. At the highest temperature of 110°C, heterogeneity in the modulus is evident at the earliest aging times for the 0.2-cm thick sample of 145 and for sample 147; this heterogeneity becomes quite pronounced at later times. Material 146 starts aging relatively homogeneously at 110°C, but later becomes quite heterogeneous. Materials

148 and 150A show relatively homogeneous aging behavior at 110°C. The heterogeneity noted for 145 and 147 (and later in time for 146) is caused by diffusion-limited oxidation (DLO). This occurs when the rate of consumption of the oxygen dissolved in a material is faster than it can be replenished by diffusion from the surrounding air atmosphere. As the results indicate, a reduction in aging temperature leads to reduced DLO effects. This is because the oxygen consumption rate decreases more rapidly with decreasing temperature than the oxygen permeation rate. Thus, all of the materials appear to age relatively homogeneously when the aging temperature is reduced to 80°C.

Given the relative importance of DLO for several of the currently studied materials and the complex way the importance of DLO changes with both time at higher temperatures and with temperature, it is somewhat surprising that the ultimate tensile elongation results show reasonable superposition for all of the materials. However, since oxidation at the sample surface will be the equilibrium oxidation expected under air-aging conditions (DLO effects are absent at the surface), the changes in modulus at the surface reflect oxidation in the absence of DLO. This observation coupled with the fact that the surface modulus increases with aging time faster than the modulus in interior regions indicates that the maximum rate of hardening occurs at the surface. When a sample is tensile tested, one might expect cracks to initiate first at the hardened surface. If such cracks immediately propagate through the material, then the surface properties (equilibrium oxidation conditions) would determine the ultimate elongation. If this supposition is true, then a plot of surface modulus versus ultimate tensile elongation should be correlated for all aging temperatures. Such plots for the six materials, shown in Figs. 34-39, clearly show that such a correlation exists (only 110°C profiles were obtained for the thin sample of Material 145). Thus, the elongation is well behaved because the equilibrium oxidation at the sample surface determines the surface hardening which in turn determines the elongation. It is perhaps interesting to note that all of the materials reach fairly low elongation values by the time the modulus has reached ~100 MPa.

Tensile strength, which results from the same tensile test as elongation, might be expected to behave quite differently since it comes from the force at break, a property that is integrated across the sample cross-section. As such, it should show evidence of the complex DLO effects as the temperature is changed unless the tensile strength happens to have little dependence on the level of oxidation. Even with the relatively large scatter in the tensile strength data, we saw earlier that the three materials with important DLO effects (thick 145, 146, and 147) gave indications of non-superposable tensile strength data for long aging times at 110°C. Figure 40 shows a plot of elongation versus tensile strength for Material 147. The deviation of the data at 110°C reflects the fact that DLO reduces the tensile strength contributions for portions of the material influenced by significant DLO effects.

Modulus measurements on unaged materials led to other interesting observations. Not only do different batches of the same material give different initial values of modulus, but also the unaged modulus can change significantly with time while resting at room temperature. Some representative data will serve to illustrate these effects. Table 3 summarizes unaged modulus results (average of around 10 measurements made across

sample using modulus profiling) for samples of Material 148 from several different compression molded sheets at different times and for samples of Material 148B (a different batch). The initial modulus measured for a sample from batch 148 was 3.4 MPa in February, 1994. A repeat run on the exact same sample four and a half years later gave a modulus value of 4.5 MPa, an increase of approximately 32%. Recent results on four other sheets from this same batch gave values similar to the recently measured value. Recent results on thick and thin samples from batch 148B gave a slightly higher value (4.8 MPa).

Table 3. Unaged modulus results for Material 148.

Material	Date	Modulus, MPa
148 -sheet 1	2/8/94	3.4±0.2
148 -sheet 1 (same sample)	8/27/98	4.5±0.2
148- sheet 2	8/27/98	4.34±0.15
148- sheet 3	8/27/98	4.4±0.4
148- sheet 4	8/27/98	4.13±0.15
148- sheet 5	8/27/98	4.4±0.3
148B- 0.08 cm	8/21/98	4.8±0.25
148B- 0.2 cm	8/21/98	4.8±0.25

Table 4 shows some results for measurements on exactly the same samples of Materials 145, 146 and 147 taken in early 1994 and in September, 1998, as well as some recent measurements taken on materials from batches 145B, 146B and 147B. Again, the modulus values for all three materials increased approximately 30-50%. Modulus values from the second batch of each material agreed reasonably well with the recent measurements on the first batches. Although the observed time-dependent effects for the first batch of materials may be an aging phenomenon caused by four and a half years at room temperature, the more likely cause is postcuring of insufficiently cured materials. Whatever the cause, such changing properties can lead to some complicating effects when trying to quantitatively model material property changes with aging.

Table 4. Unaged modulus results for Materials 145, 146 and 147.

Material	Modulus, MPa (Date)	Modulus, MPa (Date)
145- 0.08 cm	12.7±1 (2/94)	17.8±2 (9/98)
145- 0.2 cm	13.9±1 (2/94)	20±2 (9/98)
146	3.28±0.1 (1/94)	4.49±0.1 (9/98)
147	24±2.5 (2/94)	37±5 (9/98)
145B- 0.08 & 0.2 cm		18±2 (8/98)
146B- 0.08 & 0.2 cm		4±0.3 (8/98)
147B- 0.08 & 0.2 cm		4.8±0.2 (8/98)

Oxygen Consumption Measurements

For several reasons, obtaining oxygen consumption results can be an invaluable aid to understanding both physical and chemical degradation phenomena. First of all, when oxygen is available for reaction, oxidation reactions typically dominate the chemical degradation of elastomeric materials. We saw earlier that equilibrium oxidation at the sample surfaces of oven-aged materials leads to oxidative hardening which determines tensile elongation failure even in the presence of DLO effects. Another benefit of having oxygen consumption results is that such results (in combination with oxygen permeability and solubility measurements) allow models to be developed and tested for determining the importance of DLO effects for both single materials and complex, composite structures entailing several rubber layers of varying thicknesses. Eventually, such approaches should allow whole tires to be analyzed for the importance of oxidation and the location of anaerobically aged regions during typical usage.

We perform our oxygen consumption measurements by sealing (using knife-edge flanges and a silver-plated copper gasket) known amounts of the material under investigation with known amounts of oxygen in glass containers of known volume, typically 5-30 cc. Oxygen backfill pressures are chosen such that the starting pressure would be ~16 cmHg at the temperature of the aging experiment (e.g., we allow for the pressure increase that occurs when the sample cell goes from ambient-temperature fill conditions to the aging temperature). The containers are equilibrated for times greater than $2L^2/D$ (L = sample thickness, D = oxygen diffusion coefficient within the sample) to assure that oxygen dissolved in the sample is in equilibrium with the oxygen surrounding the sample. Additional oxygen is added as necessary to restore the gas pressure to the desired starting pressure. The containers are then thermally aged for time periods chosen to consume ~40% of the oxygen (to make the average partial pressure during aging approximately equal to ambient conditions in Albuquerque (oxygen partial pressure ~ 13.2 cmHg)). With appropriate choices of fill factors (fill factor = volume of sample/ gas volume in container) and time intervals, this technique can be used to measure oxygen consumption rates down to $\sim 10^{-13}$ mol/g/s. This lower limit is achieved using fill factors of ~50%, the maximum practical value, and time intervals of around 6 months.

After aging, the residual gas composition in the containers is measured directly using a Hewlett-Packard model 5890 Series II Gas Chromatograph equipped with a thermal conductivity detector. External standards are used to set up a calibration scale for the gases being analyzed. At a single aging temperature, the container is run through multiple oxygen backfill/aging/analysis cycles, so that the oxygen consumption rates are obtained versus aging time.

Consumption rates of oxygen, ϕ , were calculated as

$$\phi = \frac{d[\text{O}_2]}{dt} = \frac{-\Delta n}{m\Delta t} \quad (2)$$

where m is the polymer mass, and Δn , the gas-phase change in the number of moles of oxygen, is calculated as

$$\Delta n = \frac{p_t V_{free}}{RT_t} - \frac{p_0 V_{free}}{RT_0} + \frac{\Delta p S m}{\rho} \quad (3)$$

using the ideal gas law; V_{free} is the free (gas) volume of the container, p_0 is the oxygen pressure measured at room temperature T_0 at the beginning of the aging interval, p_t is the oxygen partial pressure measured (via gas chromatography) at room temperature T_t after aging, and

$$\Delta p = p_t (T_t / T_0) - p_0 \quad (4)$$

The third term in eq. (3) accounts for evolution of dissolved oxygen as the oxygen partial pressure over the sample decreases due to reaction. S is the solubility coefficient of oxygen in the sample, and ρ is the density of the sample. The magnitude of the correction term for solubility varies linearly with sample mass. For typical S values of $1e-3$ ccSTP/cc/cmHg and maximum fill factors of $\sim 50\%$, it reaches a maximum of typically 4%. By directly measuring changes in the oxygen content of the containers, this approach eliminates questions arising from contributions of volatile oxidative products such as CO and CO₂. In fact, the production rates of CO and CO₂ are also obtained from the gas chromatographic analysis. Further details on our experimental procedures are available in Appendix 1 of this document.

Figures 41-46 give oxygen consumption rate results for Materials 145-150. Results for batches 145, 146 and 149 (Figs. 41, 42 and 45) and some limited results at 65°C for batch 150A (Fig. 46) were obtained several years ago. The results shown for batches 147B, 148B (Figs. 43 and 44) and most of the results for batch 150A (Fig. 46) were generated recently. It appears from Fig. 41, 42 and 46 that samples of material tested shortly after being produced gave oxygen consumption results that had a tendency to initially drop with time before reaching more constant values. Material that was left undisturbed at ambient temperature for a few years (Figs. 43, 44 and 46) gave relatively constant consumption rates, perhaps near the asymptote of the materials that initially dropped with time (see Fig. 46). The early drop for fresher samples may represent reaction with impurities or it may be associated with the apparent postcuring noted in the preceding section that raised unaged modulus values by 30-50%. Whatever the cause, it implies that the oxygen consumption values change with storage at ambient temperature and may also be batch dependent, adding some uncertainty to the use of the values for quantitative modeling purposes.

The oxygen consumption results can be integrated and then time-temperature superposed in the usual manner by choosing the empirical multiplicative shift factor, a_T , for the high temperature data that gives the best superposition with the low temperature results ($a_T = 1$). Figures 47- 52 show the resulting superposed results at a reference temperature of

65°C. The shift factors used to multiply the times at the higher temperatures are noted on each of the figures.

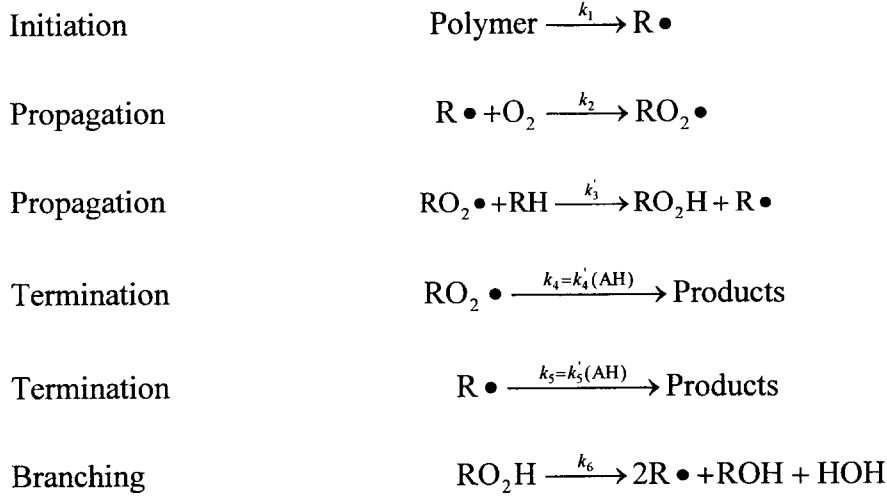
Arrhenius Analyses of the Shift Factors

We can now take the empirically derived, multiplicative shift factors determined for the elongation results (Table 2) and for the oxygen consumption data (previous section) and plot the log of these results versus inverse absolute temperature. This plot will allow us to see whether Arrhenius behavior (linear results) is consistent with the oxidative degradation of these materials. Since the elongation results were derived using 80°C as the reference temperature, we adjust the oxygen consumption results from the previous section so that 80°C corresponds to a shift factor of unity. For the oxygen consumption results of Materials 147B, 148B and 150A, where 80°C was the upper temperature used, this procedure simply requires dividing each shift factor by the 80°C shift factor. For the other materials, where the upper temperature was 96.5°C, the numbers for 65°C and 96.5°C were each divided by a constant such that the resulting straight line between them was consistent with a shift factor of approximately unity at 80°C. Figures 53- 57 show the resulting Arrhenius plots for the five materials; within experimental uncertainty, all of the materials show Arrhenius behavior with very similar Arrhenius activation energies. Since we saw earlier that the surface modulus values are well correlated with the elongation results, we can now conclude that the same temperature dependence holds for the underlying oxidation reactions, the material modulus and the elongation. In fact, essentially the same activation energy holds for all of these materials. It should be noted, however, that the activation energy for Material 149 (a halobutyl compound) is ~20 kcal/mol from the oxygen consumption results (tensile degradation studies were not done on this material).

DLO Modeling of Sheets

Diffusion-limited oxidation was the reason for the complex time and temperature dependent modulus profiles shown earlier. For most polymeric materials, the presence of dissolved oxygen during aging causes oxidation chemistry to dominate the degradation. If the rate at which dissolved oxygen is used by reactions is faster than the rate at which it can be replenished by diffusion from the surrounding air-atmosphere, a reduction in dissolved oxygen concentration will occur. This effect, which can lead to reductions in or elimination of oxidation in the interior regions of the material, is referred to as diffusion-limited oxidation [5-7]. To model this effect, diffusion expressions must be coupled with oxidative reaction rate expressions. A particularly useful and general kinetic rate expression is based on a variant of the basic autoxidation scheme (BAS), which has been utilized for more than 50 years [8-9] to describe the oxidation of organic materials. For stabilized materials, the simplified classical oxidation scheme can be written as follows [3]:

Classical oxidation scheme.



Analysis of this scheme under steady state conditions for the two radical species and the ROOH concentration leads to the following expression for the oxygen consumption rate, ϕ :

$$\phi = \frac{d[\text{O}_2]}{dt} = \frac{C_1[\text{O}_2]}{1 + C_2[\text{O}_2]} \quad (5)$$

where

$$C_1 = \frac{k_1 k_2}{k_5} \quad (6)$$

$$C_2 = \frac{k_2(k_4 - 2k_3)}{k_5(k_3 + k_4)} \quad (7)$$

By combining the expression for oxygen consumption, ϕ , given by eq. (5) with standard diffusion expressions [10], the theory for DLO of sheet material (thickness L) is easily derived [5-7]. Assuming Fickian behavior plus time-independent values for ϕ and for the oxygen permeability coefficient, P_{O_2} , a steady-state solution is obtained in terms of two parameters, α and β , given by

$$\alpha = \frac{C_1 L^2}{D} \quad (8)$$

$$\beta = C_2 S p = C_2 [\text{O}_2]_e \quad (9)$$

where C_1 and C_2 are given respectively in eq. (6) and eq. (7), p is the oxygen partial pressure surrounding the sample, D and S are the oxygen diffusivity and solubility coefficients for the polymer (the permeability coefficient, P_{ox} is the product of D and S) and $[O_2]_e$ represents the equilibrium oxygen concentration at the surface of the sample.

It is clear from eqs. (8)-(9) that β can be changed by changing the oxygen partial pressure surrounding the sample, and that α is a geometry-sensitive parameter, which can be changed by varying the sample thickness. Some representative theoretical oxidation profiles in terms of these two parameters are shown in Fig. 58. Extensive experimental tests on neoprene and nitrile rubber materials aged in thermoxidative environments [7] and a viton elastomer [11] and an EPDM elastomer [6] aged in radiation environments have quantitatively confirmed the above DLO models.

Oxygen Permeability Measurements

Further testing of the above model for diffusion-limited oxidation (DLO) on the current sheet materials requires measurements of oxygen permeability coefficients in addition to oxygen consumption results. Since the permeability measurements are required at high temperatures, we needed to significantly modify a commercial oxygen permeability apparatus (Mocon Oxtran 100). The manufacturer's specifications for the instrument stated an upper temperature limit of 60°C, but the design of the sample holder and temperature control for the as-received commercial instrument was so limited that temperature gradients across the sample were found to be greater than 20°C at 60°C.

Because of such severe temperature limitations, extensive modifications were made to the commercial instrument. The first modification was to eliminate the commercial sample holder and its totally inadequate temperature control approach in favor of a newly designed holder that was placed in an air-circulating oven. The inner workings of the new sample holder are shown in Fig. 59. A disk shaped sample is sealed by compressing between the two plates shown in the Figure with nitrogen gas flowing on one side and gas containing a selected percentage of oxygen flowing on the opposite side. The coulometric detector of the commercial instrument detects the amount of oxygen that permeates through the 3 inch working diameter of the sample. The sample holder also allows an inverted, cup-shaped container to be placed over the sealing area and sealed with bolts (see outside holes in figure) and a copper gasket. By purging this container with flowing nitrogen, this arrangement can be used to limit the amount of oxygen permeating from the edge region where the sample is compression-sealed. Since the entire sample cell is placed in the center of an oven, any desired temperature is available. In addition, the large thermal mass of the sample holder suggests fairly uniform temperatures across the sample. This is confirmed by monitoring thermocouples that are placed near the center of the sample region and in the area where purging is available (approximately one inch outside the sample diameter); these thermocouples typically read within 0.5°C of each other at temperatures up to 150°C.

By allowing measurements at higher temperatures, two new problems arose that had to be dealt with. The first had to do with the inherent limits of the coulometric detector. As

the temperature increases, the permeability coefficient increases, which can lead to excessive oxygen flux levels to the detector. The oxygen flux F to the detector is given by

$$F = \frac{\Delta p A P_{Ox}}{L} \quad (10)$$

where A is the area of permeation of the disk (fixed at 45.6 cm²), Δp is the oxygen partial pressure differential across the disk (selectable by the oxygen percentage flowing on the oxygen side) and L is the thickness of the disk (also selectable). Thus, at first glance, excessive flux can be circumvented in several ways, including the use of thicker samples or lower percentages of oxygen on the oxygen side of the sample. Unfortunately, the second problem (discussed below), involving a reduction in flux at high temperatures caused by oxidative reactions during the permeation process, is minimized through the use of thin samples and high oxygen percentages. Therefore, to accurately control the oxygen percentages and to allow for the measurement of much higher flux rates, several other modifications were made. Accurate flow controllers from MKS (Fig. 60) were used on the oxygen flow side for accurate mixing of oxygen and nitrogen streams, resulting in the capability for accurately determining the oxygen partial pressure differential. Additional MKS flow controllers plus bubble flow meters (Figs. 60-61) were used on the nitrogen flow side of the sample in order to control the nitrogen flow rate past the sample and to accurately divert a selected percentage of the flow away from the detector. This diversion scheme allowed us to measure flux rates up to approximately 10 times the normal detector limit.

The changes discussed above allowed oxygen permeability measurements to be determined at much higher temperatures than are usually reported in the literature. At higher temperatures, it became clear immediately that strange effects were operative. For instance, Fig. 62 shows temperature-dependent, permeability coefficient results for a nitrile rubber material measured with differing percentages of oxygen flowing on the oxygen side of the sample. As the temperature increased, the permeability coefficient began to show an anomalous dependence on the oxygen percentage (Δp). In addition, the permeability coefficient goes through a maximum and then actually appears to decrease above ~100°C.

These anomalies turned out to be due to oxidative reactions. In other words, at high temperatures, the flux coming through the sample was decreased due to reaction of oxygen in the material. We modeled this effect by modifying the DLO models developed earlier for sheet materials, taking account of the differing boundary conditions [12]. The modeling leads to theoretical curves for the fractional reduction in flux (FLUXOUT) relative to the flux expected if no reaction occurred. The results, which are shown in Fig. 63, are obtained as a function of the same two parameters used earlier (α and β). We can see from this plot some of the problems associated with attempting to go to thicker samples (α is proportional to L^2) or lower oxygen percentages (β is proportional to Δp) in order to keep the flux from overwhelming the detector at high temperatures. Both

remedies lead to enhanced reductions in the flux due to reaction and it turns out that relatively large reductions in flux can be difficult to accurately correct.

From the theoretical modeling for flux reductions, knowledge of the oxygen consumption rate and β allows us to correct the experimental results, thereby compensating for oxidative reactions. For instance, knowledge of the oxygen consumption rates and estimates for β allow us to analyze the nitrile results of Fig. 62, leading to the corrected permeability results shown in Fig. 64. It is interesting to note that the final permeability coefficient results show curvature, even though they are plotted on an Arrhenius plot (log of P_{O_x} versus inverse absolute temperature). This curvature is anticipated, based on past experimental results for various gases [13-14] as well as for theoretical reasons [15].

We used the upgraded permeability apparatus in combination with the modeling on flux reductions and applied these capabilities to temperature-dependent measurements on Materials 145-150. The results versus inverse absolute temperature are summarized in Figs. 65-66. Measurements on samples from batches 148B, 146B and 150A are plotted versus temperature on Fig. 65 as the open triangles, diamonds and squares, respectively. The results for each material show the expected curvature to lower slopes at higher temperatures. Some limited measurements (one or two temperatures) were taken on samples from different batches of two of the materials (148 and 146) and a second sheet from batch 150A. The results (solid symbols) were ~30-40% lower than the first set for each material. The results for Materials 145, 147 and 149 (Fig. 66) again show the expected curvature versus temperature. As anticipated, Material 149 (the halobutyl liner) has much lower oxygen permeability coefficients. Similar to the results shown on Fig. 65, Material 145 gives a moderate batch to batch difference. The batch-to-batch variations found for P_{O_x} are consistent with similar batch-to-batch and time variations found earlier for the modulus and oxygen consumption results.

DLO Modeling of Sheets of Materials 145-150

We are now able to use the oxygen consumption and oxygen permeability coefficient results generated for Materials 145-148 and 150 to obtain estimates for these parameters at the temperatures used for the oven aging experiments (80°C, 95°C and 110°C). For the permeability results shown in Figs. 65-66, this entails small extrapolations of the curved results in order to obtain estimates at 95°C and 110°C. For the oxygen consumption results, extrapolations to 110°C (and 95°C for 147, 148 and 150) are done using the Arrhenius activation energies estimated in Figs. 53-57. Table 5 summarizes the resulting estimates.

The theoretical modeling of sheet material discussed earlier and quantitatively confirmed for several materials aged under thermoxidative and radiation-initiated conditions gives the following expression in terms of the two modeling parameters α and β .

$$\alpha = \frac{(\beta + 1)\phi L^2}{pP_{O_x}} \quad (11)$$

Table 5. Estimates of oxygen consumption rates and oxygen permeability coefficients.

Compound	145	146	147	148	150
ϕ at 80°C	1.5e-10	8.3e-11	4.5e-10	1.8e-10	1.1e-10
ϕ at 95°C	6.1e-10	3.2e-10	1.84e-9	6.8e-10	4.5e-10
ϕ at 110°C	2.24e-9	1.1e-9	6.7e-9	2.35e-9	1.64e-9
P_{Ox} at 80°C	8.5e-9	1.15e-8	5.8e-9	1.5e-8	8.8e-9
P_{Ox} at 95°C	1.1e-8	1.6e-8	7.6e-9	2.0e-8	1.2e-8
P_{Ox} at 110°C	1.3e-8	2.0e-8	9.4e-9	2.5e-8	1.6e-8

Units of ϕ are mol/g/s; units of P_{Ox} are ccSTP/cm/s/cmHg

From the general shapes of the modulus profiles (Figs. 19-33), we estimate that β is approximately equal to 5 for the current materials, a value in the range typically found for air aging of elastomers [7]. It turns out that the general conclusions drawn from the modeling do not depend greatly on the precise value of β [6,7]. Using this value for β together with the estimates for ϕ and P_{Ox} (Table 5) allows us to calculate values of α for each material versus temperature. The results, assuming an average sample thickness L of 0.2 cm, are summarized in Table 6; in terms of the units used in Table 5, eq. (11) becomes

$$\alpha = \frac{(\beta + 1)\phi L^2}{\rho P_{Ox}} = \frac{6(0.2cm)^2 (2.24 \times 10^4 \text{ ccSTP / mol})(\rho)(\phi)}{(13.2cmHg)(P_{Ox})} = 407 \frac{\rho\phi}{P_{Ox}} \quad (12)$$

where ρ is the sample density in g/cc (Table 6) and 13.2 cmHg represents the ambient oxygen vapor pressure in Albuquerque where the oven aging experiments were conducted.

Table 6. Estimates of the parameter α assuming $\beta = 5$.

Compound	145	146	147	148	150
α for 110°C	82	25	347	42	49
α for 95°C	26	9	118	15	18
α for 80°C	8.4	3.3	38	5.4	5.9

In comparing the results in Table 6 with the theoretical profiles for $\beta = 5$ generated earlier in Fig. 58, there are several important factors that must be kept in mind. First of all, the scatter found from batch to batch, within batches and versus time for the modulus values, oxygen consumption rates and permeability coefficients implies that there is a relatively large uncertainty in the values derived in Table 6. In addition, the values shown reflect the DLO situation for unaged materials (e.g., early in the aging process); it is known [7] that the edge hardening (modulus increases) caused by aging can lead to significant

reductions in P_{Ox} , in turn leading to more and more important DLO effects. With these points in mind, we can tentatively conclude from Table 6 that, from the very beginning of aging, Material 147 at 110°C ($\alpha \sim 350$) should show large DLO effects, and 147 at 95°C ($\alpha \sim 120$) and 145 at 110°C ($\alpha \sim 80$) should show noticeable DLO effects. For all other combinations of Materials and temperatures, degradation at early times should be relatively homogeneous. These conclusions are in reasonable accord with the experimental modulus profiles shown in Figs. 19-33. For several combinations of material and aging temperature, the importance of DLO effects seems to grow at later stages of the degradation; this is especially noticeable for 145 at 95°C and 146 at 110°C. Since we did not attempt to determine the effect of aging on the experimental values of P_{Ox} , we cannot definitively conclude that decreases in P_{Ox} are responsible for these observations.

Since Material 147 has the largest DLO effects, we will do a more complete comparison of the experimental and theoretical profiles to show the general approach applied. To correlate equilibrium oxidation to modulus, we use the surface modulus values versus time and temperature and superpose them in the usual manner, resulting in the superposed data shown in Figure 67. The shift factors used to superpose the data are virtually identical to those used to superpose the elongation data (Fig. 10); this is not unexpected considering the correlation between surface modulus and elongation (Fig. 37). The superposed data is plotted on a semi-log plot in order to see if the surface modulus grows approximately exponentially with time, a dependence observed for several other materials [7]. Although the superposed surface modulus data is not quite exponential, we approximate the dependence by the exponential straight line shown on the figure. Although this approximation is convenient for data analysis, more complicated functional forms can be easily handled in a similar fashion. Assuming that 1) the oxidation follows this exponential behavior, 2) the oxygen consumption values and the oxygen permeability coefficients do not change with aging and 3) the model parameters estimated in Table 6 are accurate, theoretical modeling at the three temperatures of interest leads to the results shown in Figs. 68-70. Comparing these theoretical results with the experimental results shown in Figs. 25-27 shows that our understanding of DLO effects is quite reasonable. The comparisons imply that the values of α derived in Table 6 might be slightly high, but given the uncertainties in the values caused by batch to batch and time variations, any slight differences are easily explained.

Solubility Coefficient Estimates

Our next goal was to apply DLO modeling to a laminate containing numerous layers of bonded rubbers, each of different thickness and with different oxygen consumption and permeability coefficients. Developing such models is clearly required to eventually understand DLO effects for tire-like structures. For such composite, it turns out that an additional parameter, the solubility coefficient (S), is needed for each layer in addition to the oxygen consumption rates and the permeability coefficients.

Our first attempts to obtain estimates of solubility coefficients came from a method based on measurement of pressure changes over time in a sealed container. For a commercial

EPDM elastomer (SR793B-80), the measured solubility obtained by this method was in close agreement with literature values. However, for the natural rubber and SBR-based elastomers under current study (Materials 145-150), the solubilities derived greatly exceeded literature values (by a factor of ~5 for Materials 145-149 and a factor of ~10 to 15 for Material 150). Because we felt that this discrepancy with literature values called into question the derived values, we decided to use a second approach to estimate the solubility coefficients. This approach uses the oxygen permeability apparatus to monitor the time dependence of the oxygen flux. Before the experiment is started, nitrogen is flowed on both sides of the sample for sufficient time so as to assure that no oxygen is initially in the sample. At time zero, the nitrogen flow on the oxygen side of the sample is abruptly switched to oxygen flow. The oxygen flux detected on the coulometric detector side of the sample is then monitored at selected times until equilibrium flux is eventually reached. The time dependent data allows both the solubility and diffusion (D) coefficients to be determined and therefore P_{Ox} , which is the product of S and D [16]. The procedure involves plotting $\log[F(t^{0.5})]$ versus $L^2/4t$, where F is the flux, t is the time and L is the sample thickness. The plot is predicted to give a straight line, with the diffusion coefficient available from the slope and the solubility coefficient available from the intercept. Representative data for a 0.201 cm thick disk of the EPDM elastomer (SR-793B-80) is given in Table 7 ($\Delta p = 6.6$ cmHg).

Table 7. Time-dependent flux data for an EPDM material at 51°C.

T , min	F , ccSTP/m ² /day	$Ft^{0.5}$	$L^2/4t$
34	42.9	250	2.97e-4
54	70.4	517	1.87e-4
61	76.4	597	1.66e-4
146	95.4	1153	6.92e-5
256	97.6		
358	97.8		

Figure 71 shows a plot of $\log[F(t^{0.5})]$ versus $L^2/4t$ for this EPDM material. The data show excellent linearity, which allows values for D and S (and therefore P_{Ox}) to be obtained. The value of P_{Ox} obtained (3.45e-9 ccSTP/cm/s/cmHg) is virtually identical with the value obtained directly from the equilibrium flux at the end of the experiment (3.44e-9). In addition, the value of D can be obtained in another way as

$$D = \frac{L^2}{6t_{0.614}} \quad (13)$$

where $t_{0.614}$ is the time required for the flux to reach 61.4% of its equilibrium value [17]. Using this approach, D is estimated to be 2.47e-6 cm²/s, again virtually identical to the value obtained from the analysis of Fig. 71 (2.48e-6). Finally, the value of S derived from Fig. 71 (1.39e-3 ccSTP/cc/cmHg) is close to expected literature values for EPDM

materials. Therefore, it is clear that the approach used in Fig. 71 would normally be expected to a viable method for obtaining solubility coefficients.

The situation becomes somewhat more complex when applying this approach to Materials 145-150. For Materials 145-149, moderate inconsistencies (~30%) occur between direct measurements and measurements derived from time-dependent analyses similar to that done in Fig. 71, as well as some small to moderate curvature in the data. Material 150, on the other hand, shows such large curvature in the data that an analysis similar to that done in Fig. 71 is impossible. As an example of results for Materials 147-150, Fig. 72 shows data for a 0.218-cm thick sample of Material 147B at 31.4°C. For this material, the curvature in the data is fairly small. However, the values of the parameters derived from the analysis ($P_{Ox} \sim 1.03e-9$ and $D \sim 9.6e-7$) are moderately different from the results found directly for P_{Ox} ($1.28e-9$) and from $t_{0.614}$ for D ($8.03e-7$). For these reasons, we estimate an uncertainty of perhaps $\pm 25\%$ in the value of S ($1.03e-3$). The results for Materials 145, 146, 148 and 149 are similar (small curvature in the data and discrepancies of 20-30% between the direct and the indirect analyses). Table 8 summarizes the values obtained for S for these materials, which are consistent with expectations based on literature results.

Table 8. Solubility coefficients for Materials 145-150

Material	Temperature, °C	S , ccSTP/cc/cmHg
145B	25.5	1.01e-3
146	31.5	1.03e-3
147B	31.4	1.07e-3
148	31.5	8.1e-4
149B	26.8	9.7e-4
150A	31.6	4.1e-3

The results for Material 150, shown in Fig. 73, show so much curvature that conventional analysis is impossible. For the sake of analysis, we assumed that two components underlie the time-dependent results, a fast component which has the slope governed by the first two data points (right side of figure) and a second (slower) component. Analysis of the fast component (dashed line in Fig. 73) gives the results shown on the figure for S , D and P_{Ox} . By using the dashed line to determine the flux for the fast component and subtracting this contribution from the total flux, values of F for the remaining (slow) component are available; these are plotted in the usual manner on Fig. 74. The fact that the resulting values give quite linear behavior lends some respectability to the two-component assumption. As seen on the figure, the diffusion coefficient for the slow component is approximately three times slower than for the fast component. The sum of the fast and slow values of P_{Ox} ($9.6e-10$) is approximately 15% lower than the direct measurement of P_{Ox} ($1.1e-9$). Since the slow component of P_{Ox} represents ~78% of the sum of the fast and slow components, a first (perhaps naïve) estimate of the effective overall value of S would be given by

$$S = (0.78)(5.06e - 3) + (0.22)(4.8e - 4) = 4.1e - 3$$

This value is approximately four times larger than both values of S for the other materials and typical literature results. Given the large curvature observed in Fig. 73 coupled with the speculative manner in which we derived an effective value for S , this result (shown in Table 8) should be viewed with caution. Clearly, the behavior of Material 150 is non-classical (non-Fickian). Although the other five materials show minor hints of unusual behavior, to a first approximation, we can assume that they follow classical behavior.

DLO Modeling of Laminates

The DLO modeling of single sheet material was extended to laminated sheets of material. For each layer, kinetic expressions based on the earlier-introduced oxidation chemistry were assumed to be valid. In addition the usual assumptions made in such modeling were invoked (e.g., Fickian diffusion, Henry's Law, steady-state conditions). Since constant flux must be invoked at boundaries between sheets, an additional parameter (the solubility coefficient S) is needed for each layer. A program called lamx2, based on the modeling, was written and delivered to Goodyear. A copy of this program is included in Appendix 2. The program calculates profiles for the oxygen concentration and relative oxidation rate in laminates up to 20 layers, each layer having different thickness, oxygen consumption rate, oxygen permeability coefficient, oxygen solubility parameter and value for the parameter β defined in eq. (9). Calculations are solved numerically with the relative oxidation in each inner layer calculated as if that specific layer were at the surface.

An attempt to test the laminate DLO model was done on a specially prepared laminate supplied by Goodyear. This laminate was prepared by curing five sheets of different thicknesses (each sheet had a uniform thickness) together. The position and thickness of each layer and the overall laminate thickness were meant to represent the crown area of a tire. The first two columns of Table 9 give the materials used for each layer and their thickness as a percentage of the overall sample. Figure 75 shows modulus profiling results for the laminate as received. Also plotted (solid lines) are the expected modulus values based on the "equilibrium" values found for the individual materials (see Tables 3 and 4). It is clear from the modulus profiles that the material properties of the layers change substantially when cured as a laminate; similar effects would clearly be anticipated for actual tires. Since internal compounds (e.g., 145) use increased levels of sulfur to improve adhesion to steel belts, transfer of excess sulfur across the various interfaces during cure may be one of the reasons for such effects. The apparent undercuring effect, mentioned earlier for individual sheet materials, could be an important reason for the overall reductions in the laminate modulus values versus the expected single sheet results.

Table 9. Parameters input into lamx2 program for 95°C aging of laminate.

Layer	%	ϕ , mol/g/s	P_{O_x}	S	ρ	Rel. oxid. range
149	12.5	6.8e-11	2.9e-9	9.7e-4	1.133	100 to 42
146	16	3.2e-10	1.6e-8	1.03e-3	1.123	42 to 11
145	37.5	6.1e-10	1.1e-8	1.01e-3	1.171	11 to 1.2 to 13
148	11.5	6.8e-10	2.0e-8	8.1e-4	1.096	13 to 37
150	22.5	4.5e-10	1.2e-8	4.1e-3	1.164	37 to 100

Modulus profiling was also done on the laminate after aging for 28 days at 95°C. To predict the effect of this aging, we utilize the laminate modeling and computer program. Besides overall thickness and the percentage thickness of each layer (Table 9), parameters required are values of ϕ , P_{O_x} , S, ρ and β for each layer at 95°C. These results are summarized in the remaining columns of Table 9; for values of S, the results from Table 8 (taken at ~30°C) were assumed to hold at 95°C since the temperature dependence of S is usually found to be small [7,13]. Because the modulus values for the materials in the laminate are different from those obtained on individual sheet material (Fig. 75), it is likely that the permeability and especially the oxygen consumption values would also change. In the absence of measurements made on thin slices of the laminate versus position in the laminate, we have no choice but to use the values in Table 9 derived for isolated sheets. Figure 76 shows the results obtained from the modeling. The solid curve gives the oxygen concentration profile which is normalized to the equilibrium value for the surface of layer 150 (P=100%). Since the solubility parameter for layer 150 is ~4.2 times higher than for the halobutyl material (layer 149), the relative oxygen concentration at the surface of layer 149 is ~0.24. The relative oxidation values are plotted as the dashed curve on Figure 76. This plot predicts, for instance that layer 149 will range in the amount of oxidation from 100% of equilibrium air at the surface down to ~42% of that found for equilibrium air at its interface with layer 146. The range of oxidation levels predicted for all five layers are summarized in the last column of Table 9.

Figure 77 compares the experimental modulus profile for the aged laminate with that from the unaged laminate. The results from the last column of Table 9 are noted at the top of the figure for each layer. The theoretical predictions appear to correlate well with the experimental results. Oxidation of 149 should be minimal since it is a fairly stable material (the uniform increase in modulus is probably due to the above-noted post-curing phenomenon. Layer 146 does appear to oxidize much more at its interface with 149 (40% oxidation predicted) than at its interface with 145 (11% oxidation). Layer 145 appears to suffer minimal change in modulus (minimal oxidation) consistent with the predicted small amounts from theory (~12% at the interfaces to 1.2% at its center). As predicted the oxidation of 148 at its inside interface appears to increase substantially by the time its outer interface is reached; the oxidation of 150 shows a small increase from its interface with 148 to its air-exposed outer surface. Given the results shown in Fig. 75 and the discussion following this figure, more quantitative comparisons are unwarranted at this time.

Another example of the use of the laminate modeling program involves its application to real tires. We can select a given type of tire and use the program to estimate the importance of DLO effects at a given location by approximating the cross-section at that location as a laminate made up of constant thickness layers representative of the rubber layer thicknesses at that location. We can then input the required variables. For instance, for a typically constructed larger size tire at an “operating” temperature of 100°C, the estimated parameters for a cross-section ending at the groove of the tread would be given by the results shown in the first six columns of Table 10. Inputting these parameters into lamx2, using $\beta = 5$, an oxygen cavity pressure of 125 cmHg and an external oxygen pressure of 15 cmHg, leads to the results shown in Fig. 78. A summary of the relative oxidation ranges (relative to equilibrium oxidation under ambient air (15 cmHg of oxygen)) for each layer is given in the last column of Table 10. It is clear from these results and from Fig. 78 that a large percentage of layer 147 is predicted to age under anaerobic conditions.

Table 10. Parameters input into lamx2 program for 100°C aging of a larger size tire.

Layer	%	ϕ , mol/g/s	P_{Ox}	S	ρ	Rel. oxid. range
149	11	1.06e-10	3.4e-9	9.7e-4	1.133	222 to 98
145	5	9.5e-10	1.2e-8	1.01e-3	1.171	98 to 50
147	73	2.86e-9	8.2e-9	1.07e-3	1.195	50 to 0 to 29
150	11	7e-10	1.3e-8	4.1e-3	1.164	29 to 100

For a typically constructed smaller size tire at an “operating” temperature of 70°C, the estimated parameters for a cross-section ending at the groove of the tread would be given by the results shown in the first six columns of Table 11. Inputting these parameters into lamx2, using $\beta = 5$, an oxygen cavity pressure of 51 cmHg and an external oxygen pressure of 15 cmHg, leads to the results shown in Fig. 79. In this instance, the lower temperatures coupled with the thinner cross-sectional distance, leads to some drop in the oxidation levels for the internal layers but not anaerobic conditions.

Table 11. Parameters input into lamx2 program for 70°C aging of a smaller size tire.

Layer	%	ϕ , mol/g/s	P_{Ox}	S	ρ	Rel. oxid. Range*
149	11	6.2e-12	1.2e-9	9.7e-4	1.133	140 to 94
146	12	3.2e-11	9e-9	1.03e-3	1.123	94 to 76
148	15	6.9e-11	1.2e-8	8.1e-4	1.096	76 to 61
145	41	5.5e-11	7e-9	1.01e-3	1.171	61 to 50 to 69
150	21	4e-11	6.6e-9	4.1e-3	1.164	69 to 100

Constant temperatures were used for the above calculations on the two tires. In reality, temperature distributions occur across the cross-section, with higher temperatures in internal regions and lower temperatures in other areas (clearly the surface of the tread will be close to ambient outside temperature). Thus a more precise estimate of the importance of DLO effects would have to consider the actual temperature distributions in the tire. In principal, such complications can be handled by writing a more sophisticated program that breaks each layer up into a multitude of sub-layers, each with the proper temperature-dependent values of ϕ , P_{Ox} and S . However, since the purpose of the calculations is to get approximate estimates of the importance of DLO effects and areas where anaerobic aging is likely, such an extension is not really called for. In addition, the changes that would result from a more sophisticated attempt to account for the temperature variations across the tire versus the use of a weighted-average temperature would probably not be large.

Modeling such as that done above for the larger tire (Fig. 78 and Table 10) represented the second piece of evidence suggesting that important anaerobic aging effects were likely for internal rubber materials in heavier tires. The first indications of the importance of such anaerobic effects came from modulus profiling results (to be described below). This insight, which was later confirmed by oxygen content analyses at Goodyear (next section), represented one of the most important accomplishments of this CRADA. It has led to a radical reordering of research directions at Goodyear. Currently at Goodyear, there is a heavy emphasis on anaerobic aging effects, an area of research that was hardly being looked at prior to the discoveries made in this CRADA.

Oxygen Content Measurements on New and Worn Tires

To help understand the importance of anaerobic aging on the internal rubber components of heavier tires, oxygen content was determined on new and worn tires. The change of oxygen content during tire testing would provide direct evidence of oxidation in components of interest. The oxygen content radial profiles of the crown area of a new tire and a lab-tested tire are shown in Figure 80. A new tire and a lab-tested tire with the same construction were dissected. Small pieces (~2 mg) across the crown area were analyzed. The difference in oxygen content as a function of position is shown in Figure 81. The internal components did not change in oxygen content, indicating anaerobic conditions. The external components (0-15 relative position) increased in oxygen content, indicating oxidation. A road-tested (in-service) tire was analyzed in a similar fashion (Figure 82). The internal components (15-65 relative position) did not change in oxygen content, indicating anaerobic conditions (Figure 83). The external components (0-15 and 65-100 relative position) experienced oxidation.

Modulus Profiles on Tires

Our modulus profiling apparatus is capable of quickly (~1 minute per modulus measurement) and easily measuring modulus values with approximately 50 μm resolution and typically $\pm 5\%$ reproducibility. It became evident very early in this CRADA that modulus profiling of tire cross-sections led to unique, interesting and

extremely valuable information. For this reason, Sandia ran numerous modulus profiles on various locations of new, laboratory-aged, and field-aged tires supplied by Goodyear. A few representative examples will be described in this section.

Figure 84 compares modulus profile results for an unaged and an aged small tire at the tread-sidewall intersection area. The first thing to note is the richness of information immediately available from the modulus profiling technique. In the tread region of the unaged sample, the modulus is relatively constant. This is not the case, however, across several of the internal layers. As discussed earlier, this is probably due to such things as sulfur transfer between layers during cure. With aging, the modulus values tend to increase at all locations in the cross-section, consistent with the oxidation results noted earlier for the various sheet materials. This is consistent with modeling expectations for these tires, where small to moderate DLO effects are expected for internal layers, but anaerobic aging is not anticipated. The increase in the tread area is fairly uniform, indicating relatively constant oxidation. Further into the tire cross-section, the increases drop indicating reductions in oxidation. At about 3 mm from the inside of the tire, little change in modulus occurs, suggestive perhaps of moderate to important DLO effects.

The same richness of information is immediately observed in Fig. 85, which gives results for an unaged and an aged tire sidewall. Although aging in this instance leads to only minor increases in modulus, the technique does show that a substantial hardening occurs at the surface of the sidewall exposed to outside ambient air.

The results for a larger tire, summarized in Fig. 86, are quite different from the tire results shown above. The first thing to notice is that the layers of the unaged tire have fairly uniform modulus values, implying less washing out of the differences between layers caused by such things as sulfur transfer during cure. More remarkable, however, is the observation that aging tends to lead to reductions in modulus values for all of the internal layers. Since anaerobic aging conditions are expected in such regions, this suggests that anaerobic aging may lead to sufficient reversion so as to reduce the modulus of these materials. In the layer adjacent to the tread (~10-14 mm), the drop is more severe away from the tread interface. It is likely that some oxidation is occurring at the tread interface and that the amount of oxidation drops towards the other side of this layer. Similar effects may be operative in the region from ~3 to 6 mm.

Experiments that focussed on the tread region of tires showed for the first time that slightly enhanced oxidation was occurring at the tread surface of an aging tire. Figure 87 gives a typical result. For these experiments, two pieces of the material were placed in our modulus profiling sample holder with their tread surfaces pressed together (facing each other). The point of contact of the tread surfaces was defined as 0 mm. As indicated in the figure, the modulus increases (typically by about 20-40%) at the tread surface. This indicates a connection between the amount and depth of oxidative hardening of the surface material and the tread life, implying a potential method for optimizing the tread formulation against wear. Experiments at Goodyear are in the process of evaluating the correlation between surface oxidation and abrasion properties of tire materials.

Because of the resolution capability of the modulus profiling apparatus, it can be used to make measurements that are extremely difficult or impossible by other approaches. For instance, in the above tire profiles, this capability allowed measurements to be made in regions not previously accessible, such as between steel cords or in small regions between belts. In another such application, studies were conducted in the apex regions of experimental tires manufactured by Goodyear. Figure 88 shows a crude sketch of the cross-section of the apex region of a tire designated as ER1001. The apex region comprises a relatively hard elastomer in the central triangular-like region whose base starts near the bead. The region is ~76 mm in length; its width variation is shown approximately in Table 12.

Table 12. Approximate width of apex region

Distance from tip end, mm	1	5	12	17	42	76 (near bead)
Width, mm	0.4	0.6	0.7	1.3	3	6.5

Modulus profiles were run on an unaged cross-section (sample 1001-31) and a sample from a tire run under severe handling maneuver conditions (ER1001-10). The profiles were taken along the approximate centerline of the apex region, starting at the bead ($P = 0\%$) and proceeding to the narrow tip ($P = 100\%$). The results for both samples are shown in Fig. 89. Although aging has little effect on the properties, the modulus values for the apex material vary dramatically dependent upon the position in the apex region. Values start at around 30 MPa near the bead, rising slightly to 40-45 MPa in the center region, then dropping substantially to around 10 MPa near the tip. This most likely indicates under curing in the low modulus tip region. Figure 90 shows a modulus profile perpendicular to the apex direction at a distance of ~6 mm from the apex tip. The width of the apex region at this location is approximately 0.6 mm. The approximately constant values of modulus across the apex region indicates both a uniformly cured material at this location and shows that the low-modulus, adjacent material is not influencing measurements in the narrow apex region. These results also imply that transfer of constituents (e.g., sulfur) across boundary layers during cure does not account for the reduction in modulus for the apex material near its tip.

Construction and Delivery of Automated Modulus Profiler

It became clear from the results of the previous sections that data from our modulus profiling apparatus represented unique and extremely useful information on tires and tire materials. Because Goodyear was interested in running large numbers of samples on the instrument, they eventually requested that we build and deliver a second apparatus for their in-house use. Our original instrument was designed for occasional use and involved full-time, tedious attention by an operator during data acquisition. Given the number of samples that Goodyear expected to run, it was necessary to modify the apparatus so that it was completely automated and computer-controlled before delivery to Goodyear. This

upgrade would not only allow Goodyear to conveniently run numerous samples, but a similar automation of our existing instrument would result in a significant improvement in capabilities for our work on Defense programs.

For each modulus measurement, the original instrument involved manual placement of the contact load, followed by manual addition of the major load 30 seconds later. After manually recording the difference in penetration caused by the two loads, the loads were then manually removed from the sample, the sample manually moved to the next measurement location and the process repeated until all measurements were finished. Clearly, full-time attention by an operator was required. Using stepper motors, stepper drivers and associated electronic controls together with a Pentium computer and LabTech Software, all of these manual operations were converted to automated control. In addition, the computer was utilized to 1) select the number and distance between data points, 2) acquire and analyze the data, and 3) control the temperature of the silicone oil bath used to stabilize the zero-weight float position. More details are given in Appendix 3, which contains instructions for the use of the computer-controlled instrument, plus timing, block diagrams and associated information on the modifications.

Two modified instruments were successfully completed and then extensively tested on Goodyear and weapon-related samples. One of the modified instruments was kept at Sandia. The other was delivered to Goodyear in late, 1996 after Goodyear personnel were trained in its use at Sandia. Figure 91 shows a picture of Sandia's completed apparatus, with a closer view of the sample area shown in Fig. 92. A typical computer output of the raw data (lower plot) and the analyzed modulus profile (upper plot) are shown in Fig. 93. Over the past year or so, Goodyear has used their apparatus so extensively that they are now running profiles 8 hours per day and claim to have a 2-year backlog of samples that they would like to examine. For this reason, they recently requested that we build them a second apparatus using funds-in Goodyear money. We are expecting to deliver the second instrument in early, 1999.

Construction of Dynamic Oxygen Consumption Apparatus

We saw earlier that important diffusion-limited oxidation (DLO) effects can occur in tire cross-sections, leading to reductions in oxidation and even aging under anaerobic conditions for internal tire layers. We also saw that it is possible to model these effects using knowledge of oxygen consumption, oxygen permeability and oxygen solubility parameters for each layer. Since the oxidation and aging of tires occurs predominantly when the tire is moving, one important question for such modeling is the possible effect of dynamic strain on these parameters. Although it is unlikely that dynamic strain effects permeability and solubility coefficients, it could have an effect on the oxygen consumption rates. Since no one has ever attempted to address this issue, we decided to build an apparatus that would allow us to answer this question.

The construction of such an instrument offers an immediate challenge since the dynamic straining must be accomplished in conjunction with the high vacuum requirement needed for the GC approach to oxygen consumption measurements. We achieved a workable

approach utilizing a metal bellows welded to a can (Fig. 94) that could be vacuum-sealed using copper gaskets on knife-edge metal seals. By connecting the metal bellows to a motor and cam arrangement (Fig. 95), it was possible to sinusoidally strain multiple tensile specimens (at 3.5 Hz) attached internally to the bellows (Fig. 96). In addition to oxygen consumption capabilities, the vacuum-tight capabilities of the instrument allow us to dynamically age samples under rigorously controlled atmospheric conditions. This means that samples can be dynamically exposed under true anaerobic conditions.

Preliminary tests on the original design uncovered several problems, which led to design changes and improvements in the apparatus. For instance, the original design used one centrally located motor to drive the bellows for both cells. The forces were balanced at the start of the experiment by proper horizontal positioning of the motor. Unfortunately, if the aging of samples in one of the two cells was faster than the samples in the other cell, the balance was lost over time, leading to mechanical instability. Building two separately controlled systems eliminated this problem. Another important change in the design was to add a solid cylinder to fill void space internal to the strained samples (Fig. 96). This reduced the free gaseous volume inside the can from ~1000 cc to 420 cc, effectively increasing the sensitivity of the apparatus by ~2.5 times and thereby allowing experiments under selected conditions of sample mass plus temperature to be done ~2.5 times faster. Another problem involved fairly large temperature gradients across the sample containers. This was minimized by adding air-flow baffling to divert hot air-flow from the bottom of the cells and suspending the cells from the top of the oven to avoid thermal contact with the oven bottom (Fig. 94). Another modification was to change the holder arrangement from ten 6-mm wide samples to six 12-mm wide samples (Fig. 96), so that 10-mm disks could be cut from the samples after aging for subsequent dynamic property evaluations at Goodyear.

Our first set of experiments using the more sensitive arrangement (free volume $V_f = 420$ cc) were run on 80-mil thick samples of Material 153 at a temperature of ~72°C. Duplicate runs in the two dynamic cells were compared to simultaneously run duplicate experiments under static conditions. The static cells were attached to the side of the dynamic cells as illustrated in Fig. 94. Under these conditions, we measured oxygen consumption rates of around $2e-10$ mol/g/s for both types of samples. Unfortunately, this result implies that oxygen consumption measurements on 80 mil thick samples may be influenced by DLO effects, thereby necessitating thinner samples for the measurements. This can be seen by using an approximate relationship that gives the critical thickness L_c for the beginning of important DLO effects [6].

$$L_c = \left[\frac{3pP_{Ox}}{\phi} \right]^{0.5} \quad (14)$$

where the parameters p , P_{Ox} and ϕ have the same meanings as earlier. With Albuquerque partial pressure p of oxygen equal to 13.2 cmHg, P_{Ox} typically around $5e-9$ ccSTP/cm/s/cmHg and ϕ equal to $2e-10$ mol/g/s, this equation leads to an L_c of 76 mil. Therefore, at ~70°C, we are forced to use 40 mil thick samples to assure ourselves that

DLO effects are not influencing the results. For other samples and temperature conditions, similar calculations can be made using the measured value of ϕ together with measurements or estimates of P_{Ox} in order to judge the potential importance of DLO effects to the measurement.

Suppose we are trying to make measurements corresponding to Albuquerque ambient oxygen pressure conditions. We therefore want the average oxygen pressure in the container to be ~ 13.2 cmHg at the aging temperature. During the experiment, we need the drop in oxygen pressure to be large enough to accurately measure (4 cmHg is reasonable), implying starting at ~ 15.2 cmHg and ending up at ~ 11.2 cmHg. If the aging temperature was chosen to be 70°C (343 K), the approximate measured pressure drop at ambient temperature (293 K) would then be given by

$$\Delta p \approx (4\text{cmHg}) \frac{(293\text{K})}{(343\text{K})} \approx 3.4\text{cmHg}$$

In terms of Δn , the number of moles of oxygen consumed

$$\Delta n = \frac{\Delta p V_f}{(760)(82)(293)} \quad (15)$$

which leads to the following equation for the experimental time required

$$t = \frac{\Delta n}{W\phi} = \frac{1.86 \times 10^{-6} V_f}{W\phi} \quad (16)$$

where W is the weight of the samples. For a V_f of 420 cc appropriate to the final sample cell design and 40 mil thick samples ($W \sim 10$ g), these equations lead to estimated experimental times of ~ 18 d, 9 d and 4.5 d, respectively for ϕ values of $5\text{e-}11$, $1\text{e-}10$ and $2\text{e-}10$ mol/g/s.

Our second series of experiments was run on 40 mil thick samples of Material 154 at a temperature of $\sim 72^\circ\text{C}$ (temperature gradient problems were discovered, characterized and worked on during this series). The results after the first time interval of 170 h are summarized in Table 13.

Table 13. Dynamic versus static results for 40 mil thick samples of Material 154.

Sample cell	Time/cycles	ϕ , mol/g/s	Ave. est. T	ϕ at 72°C
B ($18 \pm 6\%$)	170 h/ 2.1e6	$2.0\text{e-}10$	75°C	$1.5\text{e-}10$
A ($14 \pm 6\%$)	170 h/ 2.1e6	$1.78\text{e-}10$	73°C	$1.62\text{e-}10$
73 (static)	170 h	$1.47\text{e-}10$	70°C	$1.79\text{e-}10$
58 (static)	170 h	$1.31\text{e-}10$	72°C	$1.31\text{e-}10$

At first glance, the measured values of ϕ shown in column 3 would indicate increased consumption under dynamic strain conditions and enhanced consumption rate as the average strain is increased. However, the observed temperature gradients cloud this initial conclusion. After roughly estimating what we consider to be the average temperature seen by the various sample cells (listed in column 4 of the Table), we can normalize all of the measured values from column 3 to a common temperature of 72°C (using an activation energy of 23 kcal/mol). When we do this, we obtain the estimated values shown in the final column of the Table, which indicate little effect of dynamic strain. Figure 97 shows the integrated consumption results versus aging time for the average of the two dynamic cells compared to similar results for the average of the two static cells, again after attempting to compensate for estimated temperature differences. From this series of experiments, we can tentatively conclude that little difference exists between static and dynamic aging for Material 154 at average strains of ~16%. Future more careful experiments on the final cell arrangement (reduced temperature gradients) using several different materials, strain amplitudes and temperatures will lead to more definitive conclusions on the importance of dynamic strain to oxygen consumption.

Micrometer Resolution Interfacial Force Microscopy (IFM)

We are currently in the process of building a modified Interfacial Force Microscopy (IFM) instrument (Fig. 98) as an improvement to our modulus profiler apparatus that has been successfully applied to the evaluation of rubber hardness profiles. The aim is to develop a suitable microscopy technique allowing us to measure modulus data with a resolution of approximately 1-micron. This would represent a significant improvement over the modulus profiler which is limited to a maximum resolution of approximately 50 μ m. If successful this would enable us to better investigate boundary layers between rubber matrix and steel/nylon belts or transitions between different rubber layers.

The IFM technique is based on similar principles as utilized in Atomic Force Microscopy (AFM) instrumentation [18,19]. A sharp minute probe tip is used to probe a sample surface with nanometer resolution. The successful operation of AFM or Scanning Probe Microscopy (SPM) instruments requires excellent environmental vibration control, positioning devices such as piezo tubes and inchworm drives which can move samples or sensors with nanometer precision, and appropriate sensor units which can measure minute positional or force changes. SPM has been applied in various modes (such as contact, tapping, modulated or non-contact) to evaluate the roughness, hardness, composition or friction properties of sample surfaces with nanometer resolution. The technique normally delivers images of a few square-microns determined by the scanning potential of the piezo tube. The AFM commonly uses probe tips deposited at the end of a silicon or silicon nitride cantilever. The minute deflection of the cantilever is optically determined using a change in laser reflection intensity on a split photodiode. The corresponding force is related to the measured deflection via the known cantilever spring constant. The dynamic range of this micro-cantilever technique is limited by the

measurable deflection to a few nanometers and by the chosen cantilever spring constant preventing an upgrade to micron resolution instruments.

The key element in the IFM technique is the use of a fundamentally different force sensor that incorporates an automatic balancing scheme and offers a large dynamic range in the force measurements [20,21]. The force is determined by the displacement of a common plate in a differential capacitor. A force feedback scheme using a sensitive bridge circuitry is used to keep the capacitor properties balanced by applying a compensating voltage related to the actual force exerted on the sensor. Positional information is obtained from the location and movement of the piezo tube. Using such a sensor unit modified with a well defined micron-sized parabolic probe tip, and appropriate wide area scanning piezo tubes, large travel inchworms and associated electronic control equipment will enable us to build a novel micron resolution microscopy instrument without the problems related to sensitive nanometer instrumentation.

We have obtained all electronic equipment required to operate the IFM such as IFM, piezo, and inchworm controllers, as well as all necessary function generators, oscilloscopes, voltmeters and voltage supply sources and the associated National Instrument GPIB interfacing equipment (Fig. 98). We have also purchased all inchworms to allow for 3D sample positioning and a novel piezo tube enabling a large scan area (Fig. 99), as well as the other main components such as an anti-vibration table and a suitable microbalance for force calibration experiments. We were also able to machine suitable adapters for the inch worm devices to be incorporated into the positioner, a kinematic mount for the main piezo tube, and to produce the corresponding ceramic adapters. Initial interfacing of the computer with the inchworm controller and inchworm drives using Labview based software drivers has been successful. The electronics of the piezo controller were redesigned due to a low frequency noise problem. As a result, the power supply unit has been separated from the main board and a previous signal contamination is now under control. A kinematic base for a microbalance for force calibration purposes has been designed and is currently being manufactured. Advanced interfacing and wiring between the piezo and IFM controller and the corresponding components are currently prepared. Various software units need to be adapted or modified and will be in the testing stages soon. This includes digital interfacing for fully computerized control of all devices.

We have successfully developed a location positioner with reverse referencing (Fig. 99) which enables us to precisely position the IFM probe tip with a target point on a sample as determined by optical microscopy. This enables IFM analysis on selected areas of large samples. The positioning device is based on two independently adjustable 3D stages, one for the sample holder and one for the microscope, which can be permanently fixed and cross-referenced to the sensor tip position via the imaging analysis of a special positioning grid.

An advanced lapping machine has been obtained which can be used to polish multiple samples simultaneously, and with a better surface finish than previously possible. The samples rotate during the polishing which minimizes the formation of surface features due to the polishing process. A water-based suspension of industrial diamonds is used as

a polishing medium. We have polished samples and analyzed by SEM, which show a surface roughness sufficient to allow for detailed micron-modulus profiling.

Various probe tips have been produced via electrochemical etching of 100- μm tungsten wire and yielded probe tips in variable size of 1-25 microns. The shape of the tip is of adequate parabolic nature as required for quantitative modulus measurements when using the Hertzian model of viscoelasticity. This model implies a linear behavior between applied force and indentation for a parabolic curve shape. The probe tip properties depend on various parameters of the etching process such as the applied cell potential, surface tension, concentration of the NaOH electrolyte, etching current and wire length and cut-off time. It is purely an empirical process but suitable tips for our IFM sensor are easily obtained.

The sensor unit is the key component of the IFM instrument since it enables a force measurement independent of the actual position or penetration depth of the probe tip. The sensor production process was previously based on micro-supergluing individual parts using light microscopy. This approach, however, yielded functional sensors only $\sim 10\%$ of the time and often with huge and unpredictable variation in the sensor sensitivity. This yield is disappointingly low, and considering the tremendous time involved when making the sensors it was necessary to explore novel alternatives. An improved and reproducible process for sensor production is currently under investigation and is based on a high voltage welding process on doped silicon substrates and other modifications to optimize the critical separation between the common and torsion bar capacitor plates. Initial experiments are encouraging and should ultimately greatly enhance our ability to obtain suitable high gain sensors.

In summary, we have obtained all necessary electronic components, inchworm and piezo tubes to build an IFM instrument. Other additional parts required for the positioning of samples, calibration of sensor unit, and flexible piezo mounts have been machined and are operational. This further includes all ceramic adapters and cable connectors. Various micron-sized parabolic probe tips have been produced via electrochemical etching techniques. Some software drivers to control inchworm and piezo movement have been implemented. This means that we currently have an operational reverse referencing positioning stage. Additional software drivers and modifications for all interface applications need to be developed or modified for our special needs. A reproducible method to produce improved high gain sensors is currently under development. The completion of this instrument will continue using funds from a Goodyear-supported CRADA.

CONCLUSIONS

During this CRADA, a great deal was learned about the mechanisms underlying tire degradation. When oxygen is present during the aging of tire materials, oxidation effects are important contributors to degradation. Oxidation will often result in modulus increases (material hardening), which can be an important underlying factor in crack initiation. Extensive mechanical property measurements were made versus time and

temperature for materials representative of the component elastomers typically used in passenger and truck tires. Analyses of the ultimate tensile elongation data using time-temperature superposition principals showed good superposition for all materials and consistency of the empirically derived shift factors with the often-used Arrhenius aging model. The activation energies derived from the Arrhenius plots were quite similar for most materials. Modulus profiling results on the same series of materials showed the presence of important diffusion-limited oxidation (DLO) effects, seemingly inconsistent with the Arrhenius behavior found for the tensile elongation results. However, the observation of excellent correlation between the surface modulus results (equilibrium oxidation occurs at the surface) and the ultimate tensile elongation for all materials showed that Arrhenius behavior was due to the immediate propagation of cracks that initiated at the hardened sample surface. The DLO effects, on the other hand, influenced superposition of tensile strength data, since tensile strength at break results from the force at break integrated across the entire sample cross-section.

The presence of DLO effects for 2-mm thick sheet materials at 95°C and 110°C suggested that important DLO effects might be operative for the aging of real tires, especially truck tires, which run at higher temperatures and have thicker cross-sections. Since oxygen permeability measurements were needed to model DLO effects for sheet materials, these values were obtained versus temperature for representative compounds of the important tire component materials. By combining the oxygen consumption and permeability results with a DLO model derived using simplified oxidation expressions appropriate for stabilized organic materials, we were able to show that the experimental modulus profiles were reasonably consistent with the theory for DLO effects.

Our next achievement was to derive a model for DLO effects of a laminate material and write software allowing easy application of the model. For each layer of the laminate, in addition to oxygen permeability and consumption results, the model required values of the oxygen solubility coefficient. Estimates of these values were obtained by measuring the time-dependent flux on an extensively modified oxygen permeability apparatus. We were now able to use the values of oxygen consumption, permeability and solubility to theoretically examine the aging of specially prepared laminates and the aging of actual tires. The conclusion of this modeling was that important DLO effects occur across real tire cross-sections and that the interior layers of truck tires are likely to age under anaerobic conditions. This was a very new and controversial conclusion, since it was believed prior to this CRADA that oxidation occurred throughout the tire cross-section for all types of tires.

The oxygen consumption measurements used in the modeling were derived on statically aged samples. Since tires are dynamically strained during aging, it is possible that actual oxygen consumption values for tire materials are even higher than those measured under static conditions. If so, the importance of DLO effects would be even greater than predicted using static values. Since measurements of oxygen consumption under dynamic loading conditions have never been reported, a special instrument was constructed to accomplish these measurements. Preliminary results on one material

indicate that little difference exists between oxygen consumption rates under dynamic and static aging conditions.

Our modulus profiling apparatus was applied to tire materials, specially constructed laminates and cross-sections of unaged tires and tires aged under laboratory and actual use conditions. The results were extremely interesting, useful and often allowed examination of areas of tires that were previously inaccessible to other techniques. Results on truck tires, for instance, offered additional evidence (with the DLO modeling) for the importance of anaerobic aging in the interior layers. This conclusion, which was still controversial at Goodyear, prompted oxygen content measurements at Goodyear on slices from the cross-sections of unaged and aged truck tires. Since the oxygen content measurements also implied anaerobic aging internally, this, at-first controversial, conclusion was finally accepted. This resulted in a paradigm shift for Goodyear's research, since anaerobic aging had been previously ignored in optimizing compound formulations and studying aging effects. There is currently a large effort at Goodyear devoted to anaerobic aging effects.

Because of the unique information available from modulus profiling and the ease and rapidity of the measurements, Goodyear requested that we build an instrument for delivery to their Akron laboratory. An automated, computer-controlled version of the instrument was delivered to Goodyear in late 1996; we built an identical instrument for use at Sandia. The instrument at Goodyear is delivering such useful information that it is now being run 8 hours per day and there is currently a two-year backlog of samples. For this reason, Goodyear recently requested that we build them a second identical instrument using Goodyear funds. The second instrument should be delivered in early 1999. Because of the utility of modulus profiling measurements, we have nearly finished building the first generation of a modified IFM that will allow measurements to be made with resolutions in the micrometer range. This should allow measurements to be made closer to interfaces between material layers and fillers, potentially yielding new information on such things as adhesion effects.

Besides all of the useful information obtained on tire aging, this CRADA (with partial support from other sources such as the Enhance Surveillance Program) led to the development of numerous improved experimental techniques and aging models, which will be useful for Goodyear, DOE and industry. The automation of our modulus profiler has resulted in enhanced throughput of samples and ease of measurement. The micro-IFM apparatus will allow us to probe samples with micrometer resolution. The improved methods for measuring oxygen permeability, which account for reaction during the measurement) will allow measurements to be made at previously inaccessible temperatures. The models for DLO effects in sheet and laminate materials can be applied to many air-aging situations. The software delivered to Goodyear on DLO effects for laminate structures is being used as a method for estimating the importance of anaerobic and DLO effects for various locations in tires.

Finally, from a DOE Defense Programs perspective, this CRADA has significantly aided the development of new and improved aging techniques and models. Since elastomers

are important in weapons, the experimental observation from modulus profiling measurements of important DLO effects for accelerated aging studies of weapon elastomers was an important observation. The derivation of the reason why tensile elongation measurements followed an Arrhenius relationship, even in the presence of DLO effects, resolved an apparent contradiction. This insight allowed surface modulus results to be used as a reflection of the true oxidation chemistry operative during degradation. The development of the ultrasensitive oxygen consumption approach, which represented the first and only method to quantitatively test the Arrhenius extrapolation assumption, was partially funded by this CRADA. The improved capability of the oxygen permeability apparatus allowed oxygen permeability coefficient measurements at higher temperatures than previously available. This led to the opportunity for better quantitative testing of the theoretical DLO models derived for the aging of weapon materials. The completion of the automated modulus profiler has resulted in a much larger throughput of weapon-related samples. Finally, the completion of the micro-IFM will allow finer details to be observed in weapon materials and at or near interfaces between materials.

ACKNOWLEDGMENTS

The authors are grateful to Mathew Celina, who has been assembling the IFM instrument and to Mike Malone, who conducted many of the experimental measurements including tensile tests, modulus profiles and oxygen consumption.

REFERENCES

1. K. T. Gillen, R. L. Clough and C. A. Quintana, "Modulus Profiling of Polymers", *Polym. Degrad. & Stabil.*, 17, 31 (1987).
2. K. T. Gillen and R. L. Clough. "Polymer Insights Available from Modulus Profiling Data.", *Polym. Eng. and Sci.*, 29, 29 (1989).
3. K. T. Gillen, M. Celina, R. L. Clough and J. Wise, "Extrapolation of Accelerated Aging Data- Arrhenius or Erroneous?", Review paper in *Trends in Polymer Science*, Vol. 5, No. 8, 250 (August, 1997).
4. J. Wise, K. T. Gillen and R. L. Clough, "An Ultrasensitive Technique for Testing the Arrhenius Extrapolation Assumption for Thermally-Aged Elastomers", *Polym. Degrad. & Stabil.*, 49, 403 (1995).
5. A. V. Cunliffe and A. Davis, *Polym. Deg. & Stabil.*, 4, 17 (1982).
6. K. T. Gillen and R. L. Clough, "Rigorous Experimental Confirmation of a Theoretical Model for Diffusion-Limited Oxidation", *Polymer*, 33, 4358 (1992).
7. J. Wise, K. T. Gillen and R. L. Clough, "Quantitative Model for the Time Development of Diffusion-Limited Oxidation Profiles", *Polymer*, 38, 1929 (1997).
8. J. L. Bolland, *Proc. Roy. Soc.*, A186, 218 (1946).
9. L. Bateman, *Q. Rev. Chem. Soc.*, 8, 147 (1954).
10. J. Crank, "The Mathematics of Diffusion", Clarendon Press, Oxford, 1975.
11. J. Wise, K. T. Gillen and R. L. Clough, "Time-Development of Diffusion-Limited Oxidation Profiles in a Radiation Environment", *Radiat. Phys. and Chem.*, 49, 565 (1997).

12. K. T. Gillen, unpublished results.
13. R. M. Barrer and G. Skirrow, *J. Polym. Sci.*, 3, 549 (1948).
14. H. L. Frisch and S. A. Stern, *Critical reviews in Solid State*, 11, 123 (1983).
15. R. Kosiyanon and R. McGregor, *J. Appl. Polym. Sci.*, 26, 629 (1981).
16. W. A. Rogers, S. Buritz and D. Alpert, *J. Appl. Phys.*, 25, 868 (1954).
17. S. Pauly, *Rad. Phys. Chem.*, 39, 269 (1992).
18. V. V. Tsukruk, *Rubber Chem. Technology*, 70, 430 (1998).
19. C. J. Chen, *Introduction to Scanning Tunneling Microscopy*, Oxford University Press (1993).
20. S. A. Joyce, J. E. Houston, *Rev. Sci. Instrum.* 62, 710 (1991).
21. J. E. Houston and T. A. Michalske, *Nature*, 356, 266 (1992).

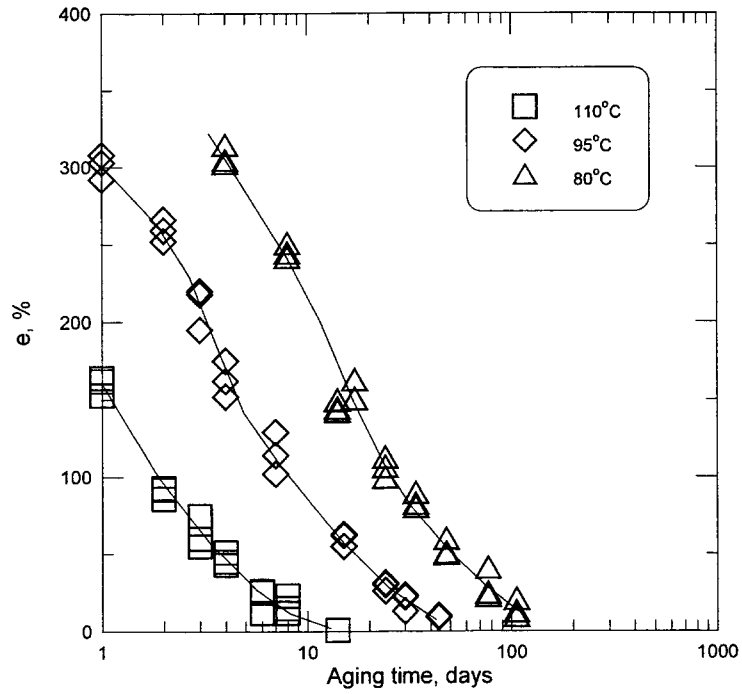


Figure 1. Ultimate tensile elongation data for Material 145 (thick) versus time at the indicated temperatures.

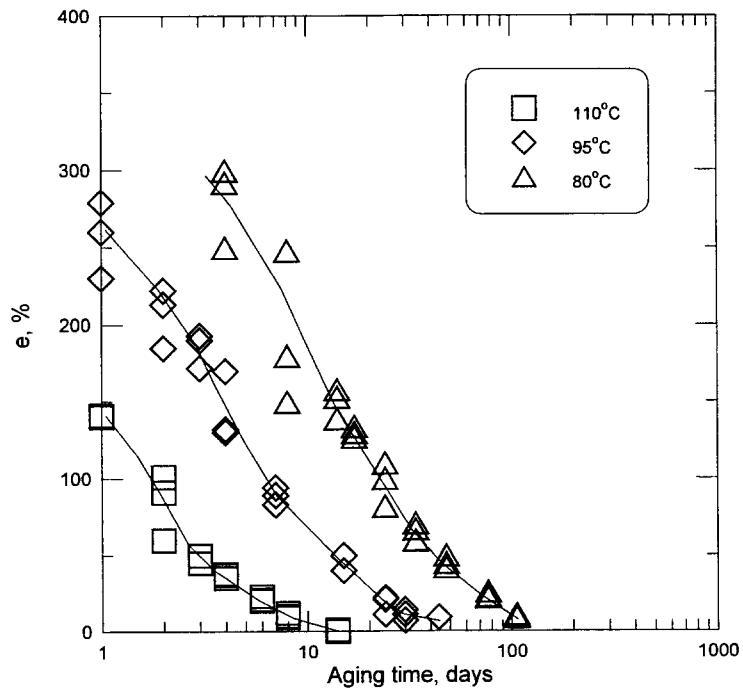


Figure 2. Ultimate tensile elongation data for Material 145 (thin) versus time at the indicated temperatures.

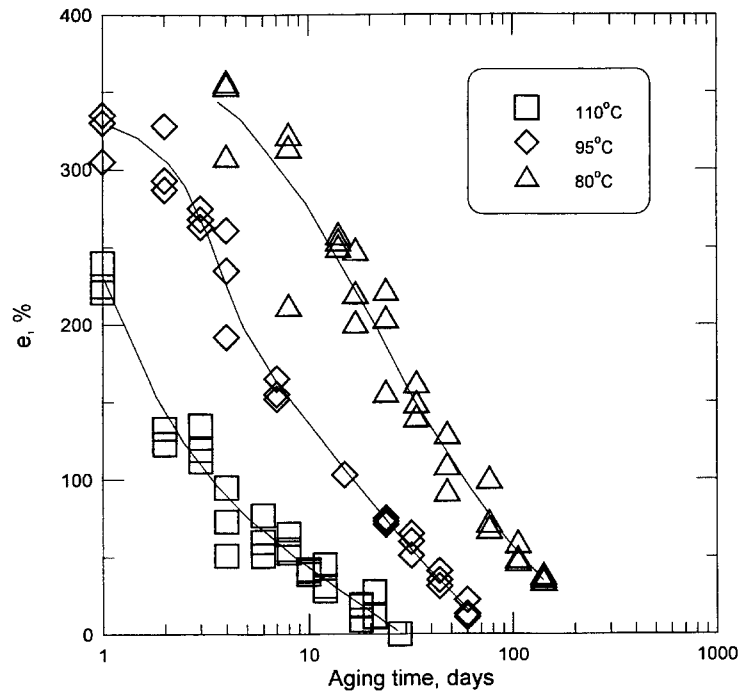


Figure 3. Ultimate tensile elongation data for Material 146 versus time at the indicated temperatures.

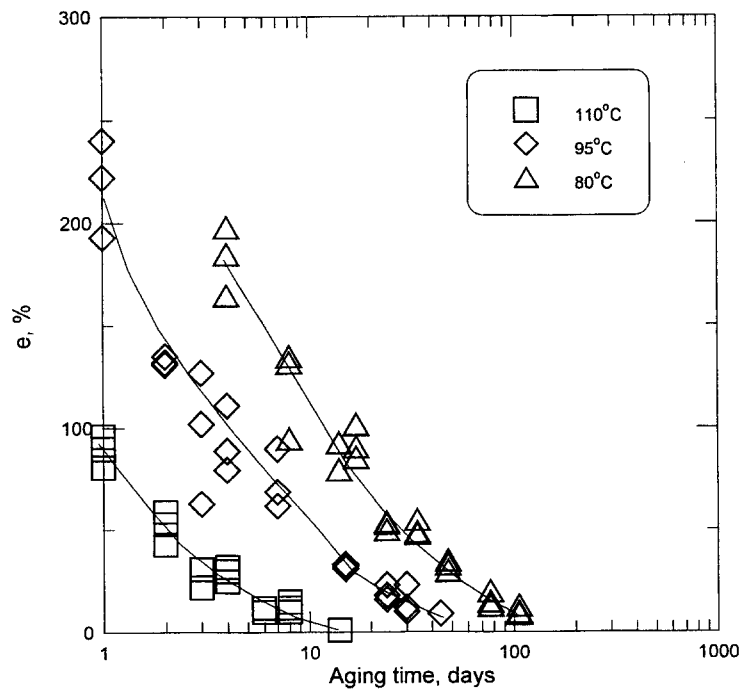


Figure 4. Ultimate tensile elongation data for Material 147 versus time at the indicated temperatures.

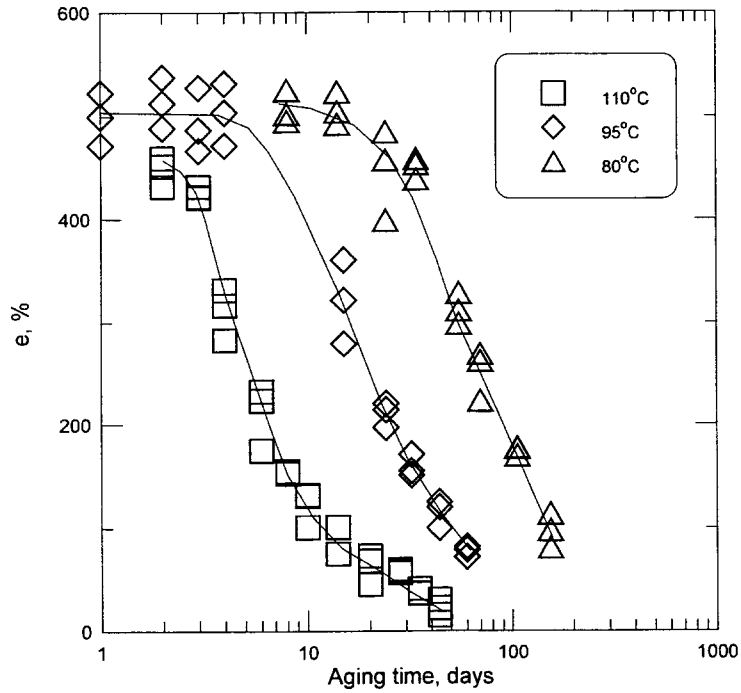


Figure 5. Ultimate tensile elongation data for Material 148 versus time at the indicated temperatures.

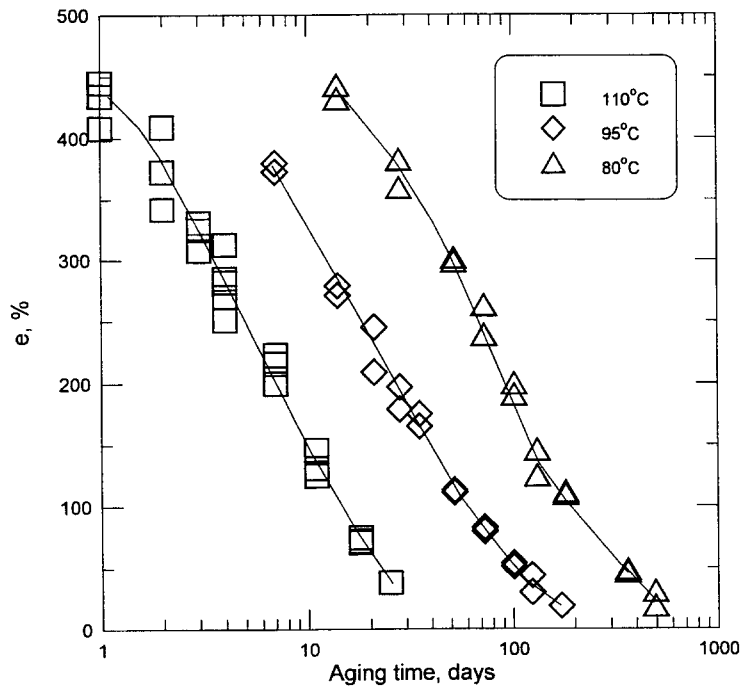


Figure 6. Ultimate tensile elongation data for Material 150 versus time at the indicated temperatures.

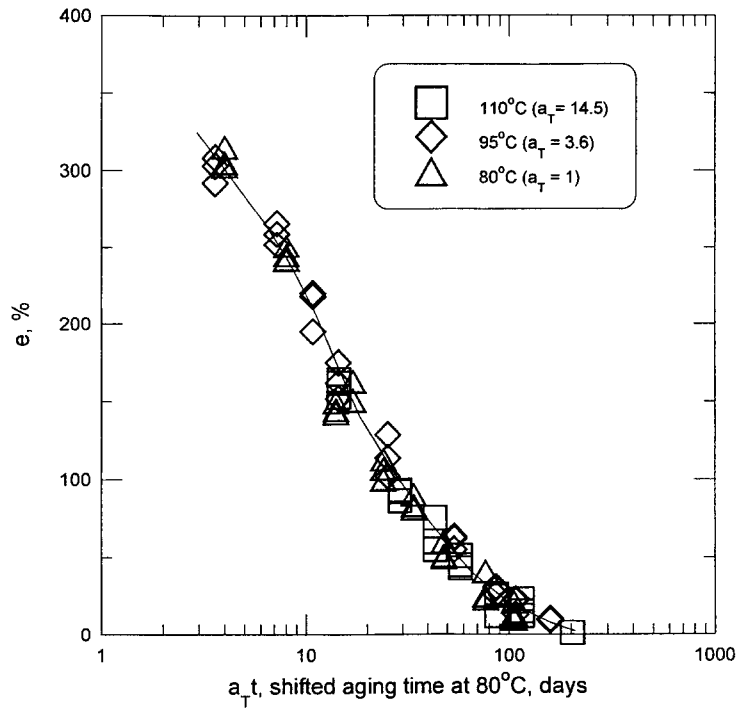


Figure 7. Time-temperature superposed elongation results for Material 145 (thick) at 80°C.

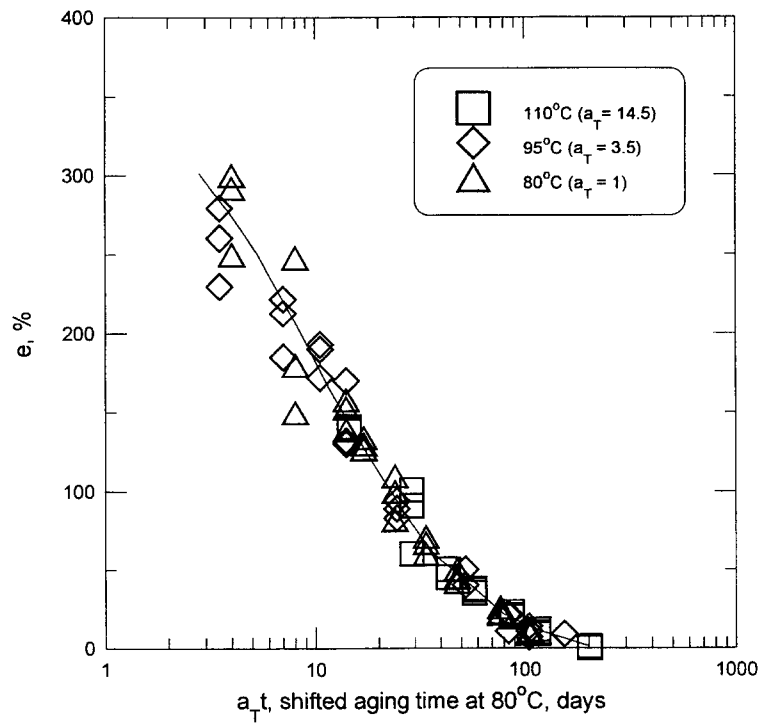


Figure 8. Time-temperature superposed elongation results for Material 145 (thin) at 80°C.

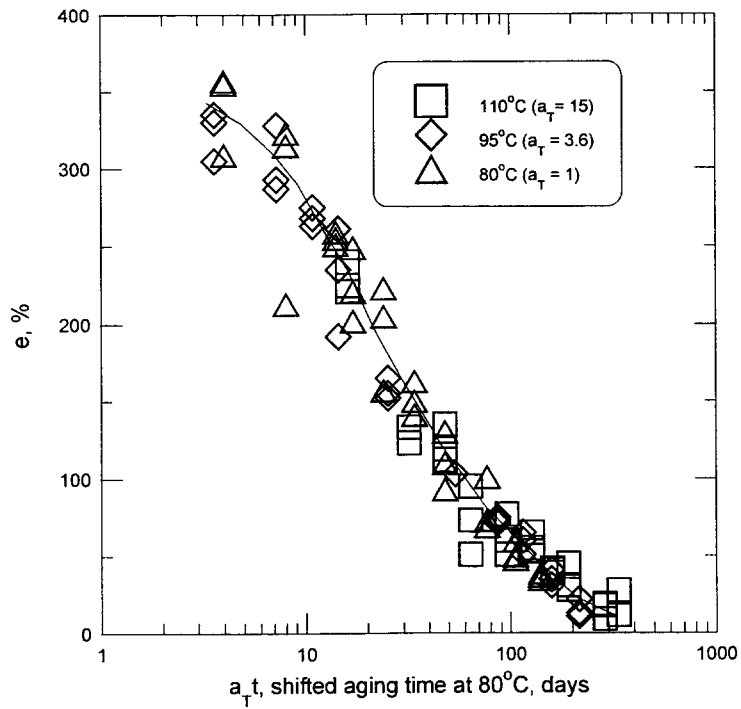


Figure 9. Time-temperature superposed elongation results for Material 146 at 80°C.

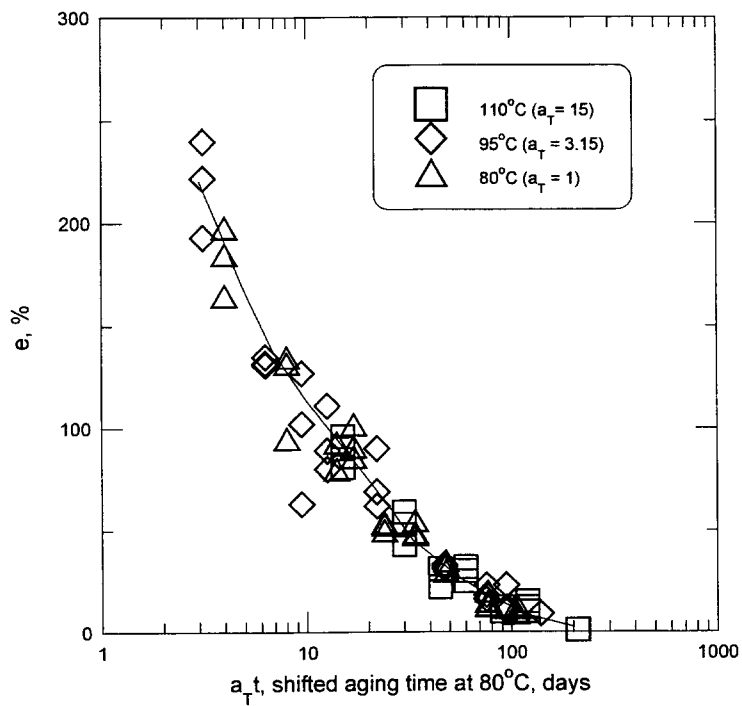


Figure 10. Time-temperature superposed elongation results for Material 147 at 80°C.

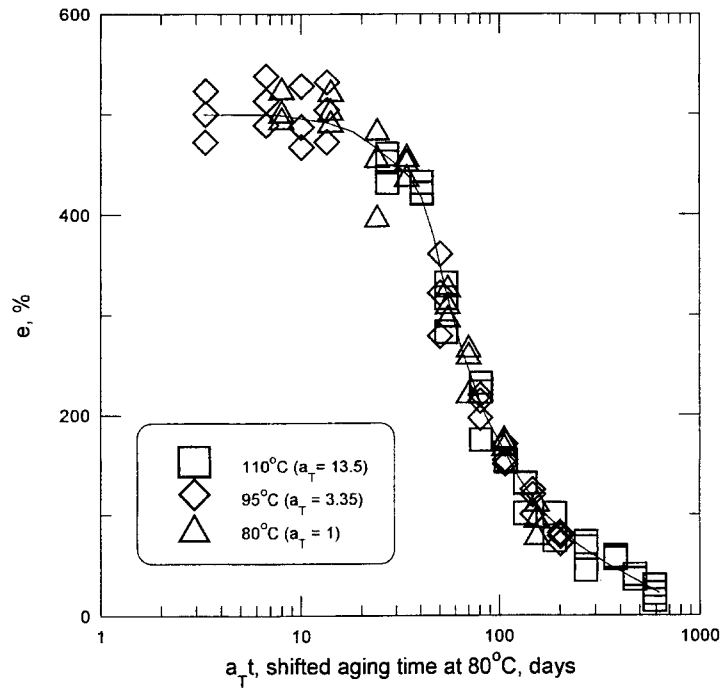


Figure 11. Time-temperature superposed elongation results for Material 148 at 80°C.

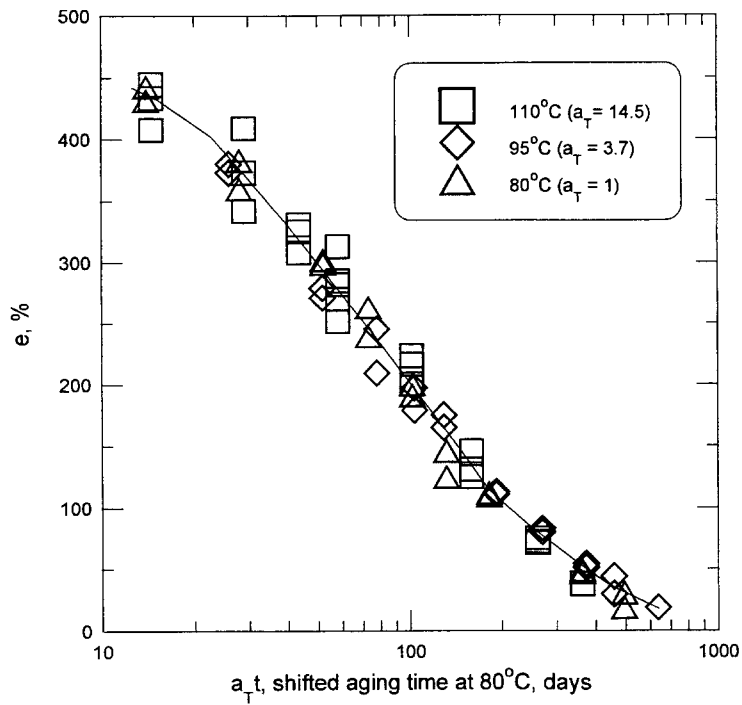


Figure 12. Time-temperature superposed elongation results for Material 150 at 80°C.

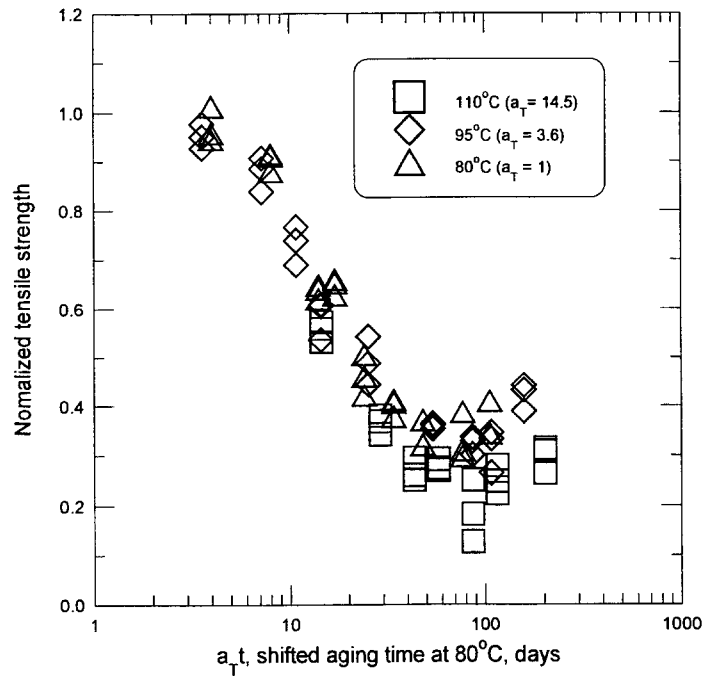


Figure 13. Superposition of tensile strength values for Material 145 (thick) using a_T values from the elongation superposition.

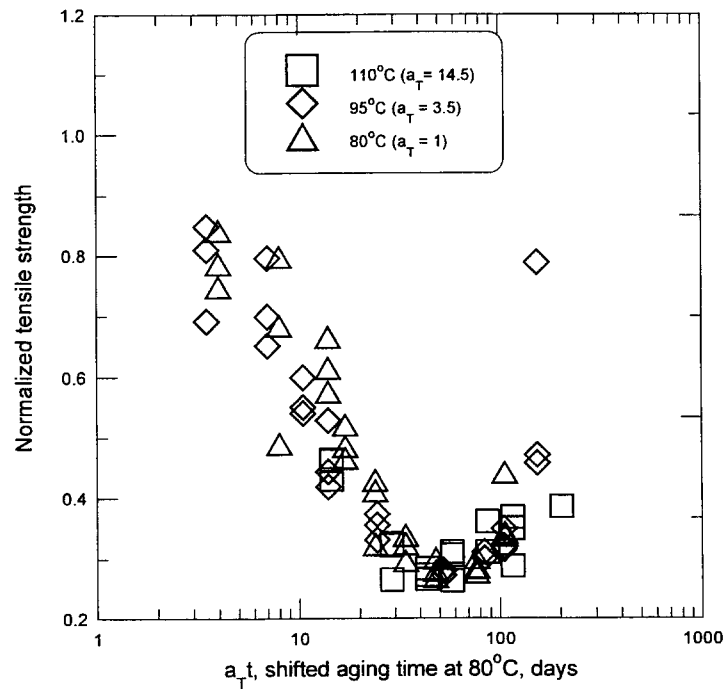


Figure 14. Superposition of tensile strength values for Material 145 (thin) using a_T values from the elongation superposition.

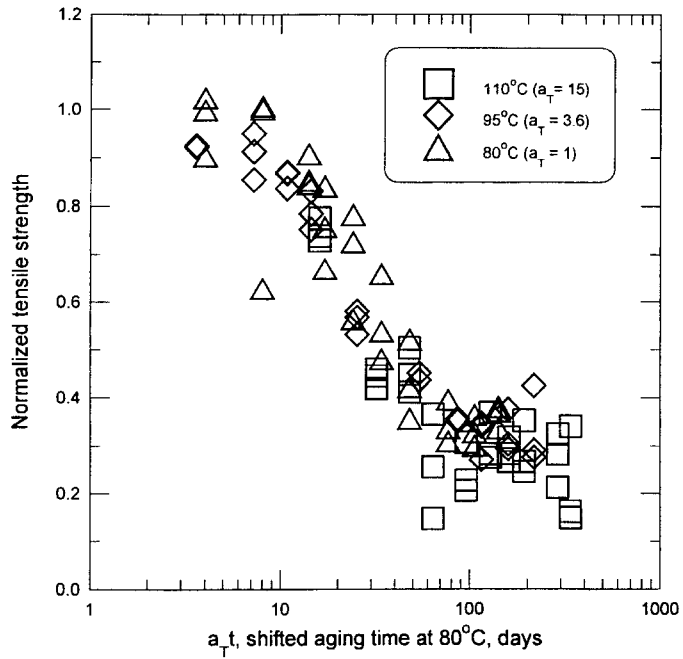


Figure 15. Superposition of tensile strength values for Material 146 using a_T values from the elongation superposition.

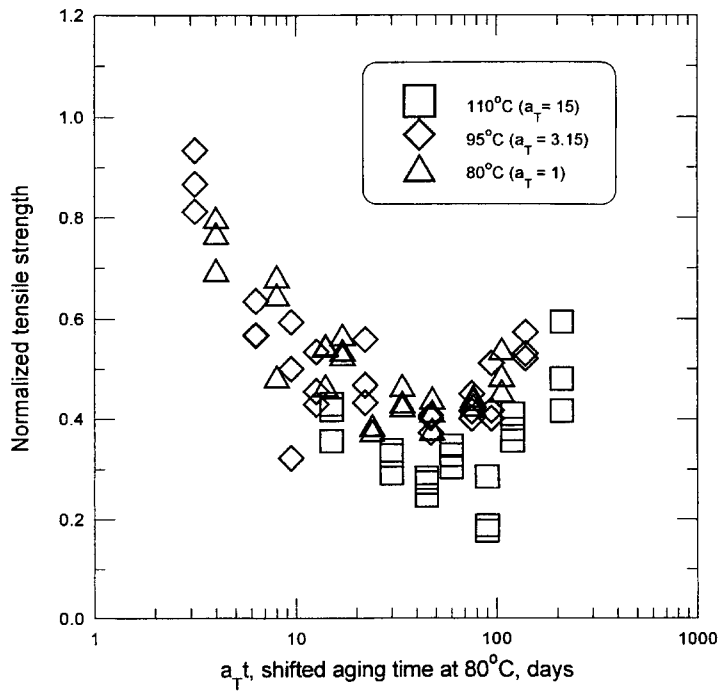


Figure 16. Superposition of tensile strength values for Material 147 using a_T values from the elongation superposition.

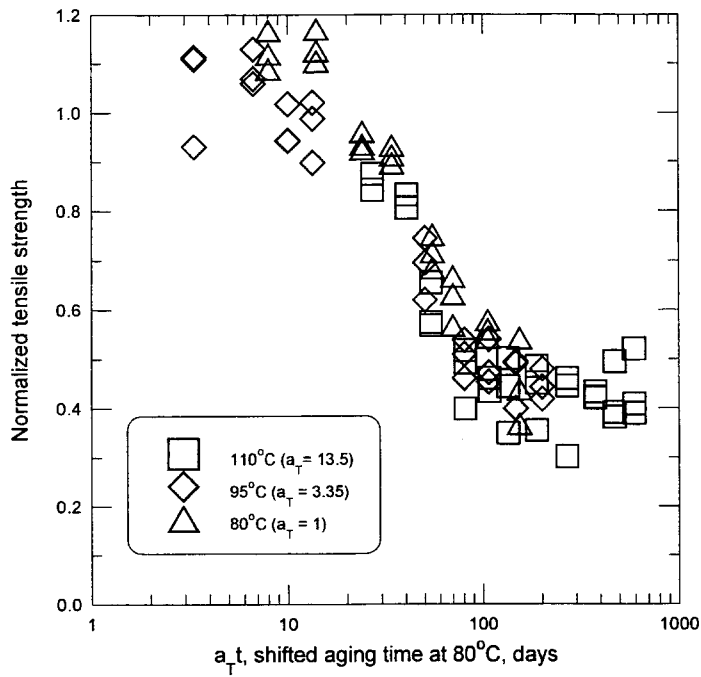


Figure 17. Superposition of tensile strength values for Material 148 using a_T values from the elongation superposition.

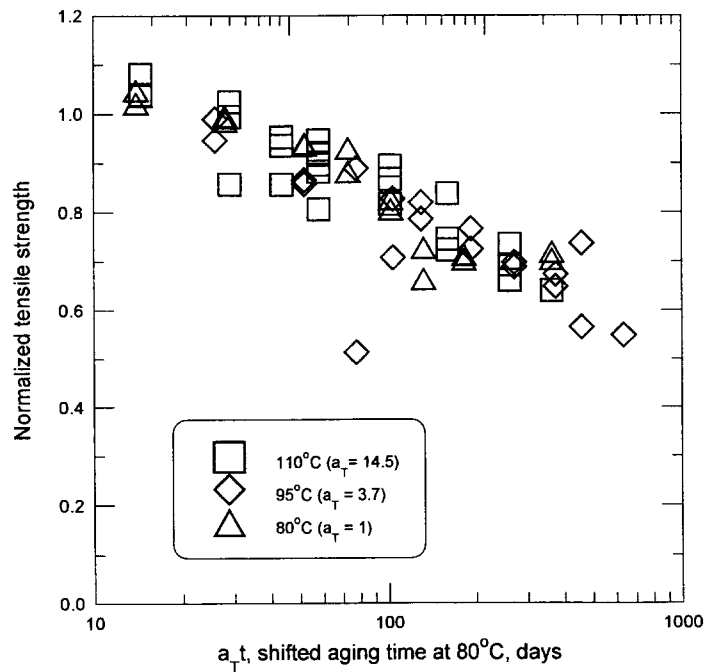


Figure 18. Superposition of tensile strength values for Material 150 using a_T values from the elongation superposition.

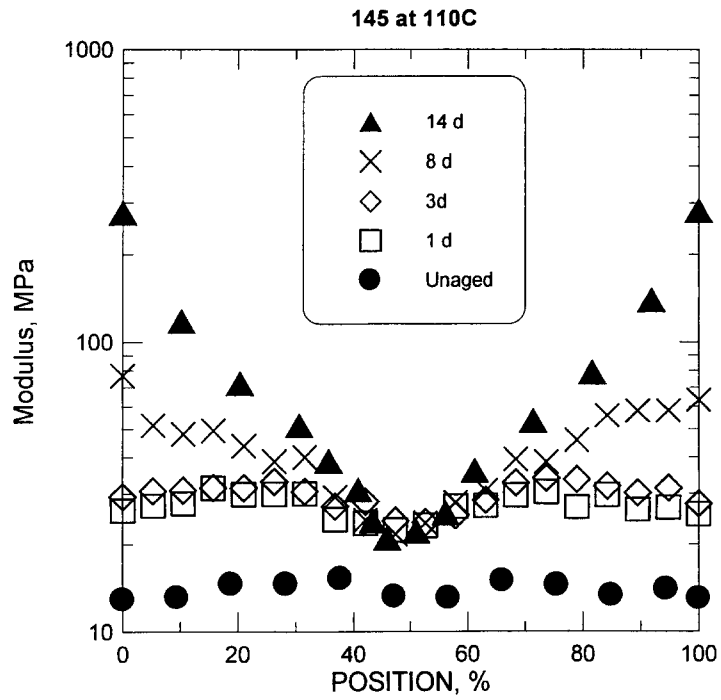


Figure 19. Modulus profiles of Material 145 after the indicated aging times at 110°C.

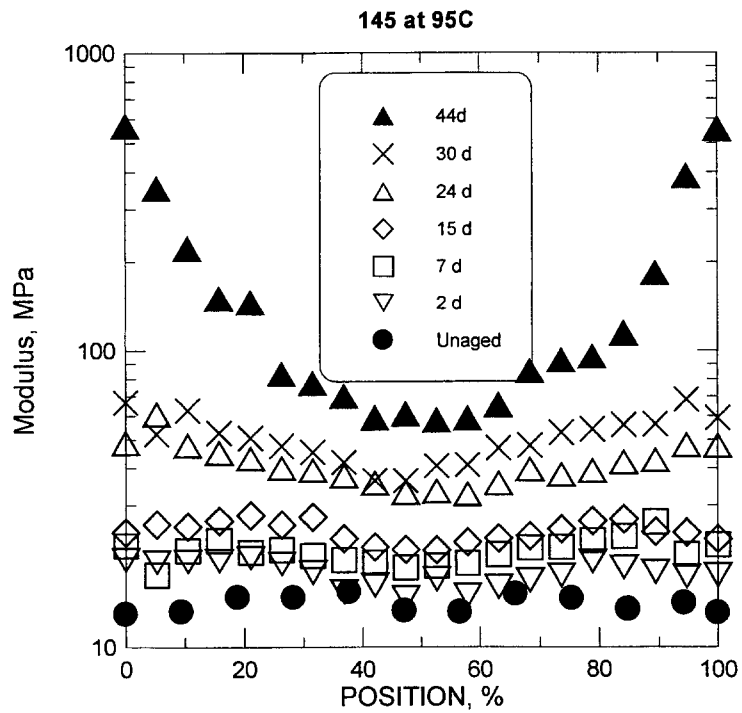


Figure 20. Modulus profiles of Material 145 after the indicated aging times at 95°C.

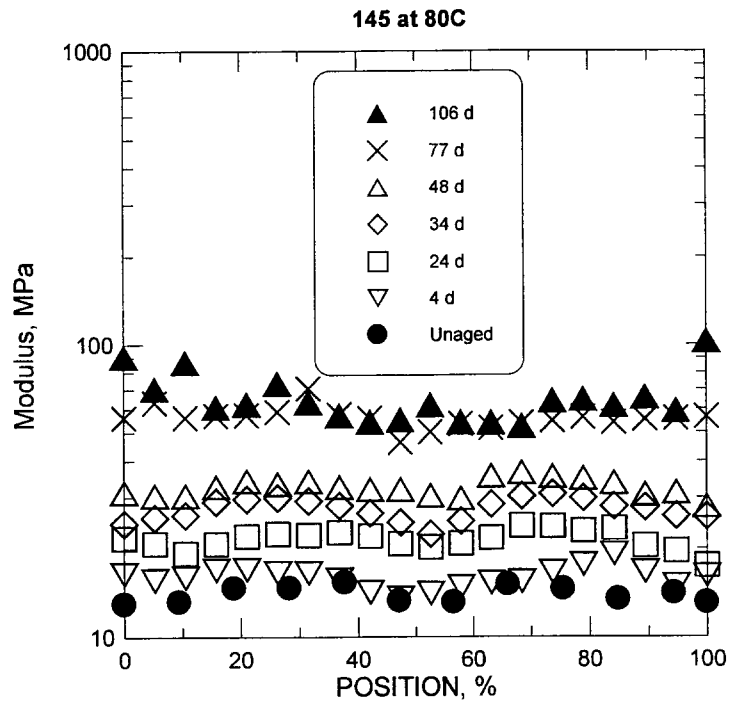


Figure 21. Modulus profiles of Material 145 after the indicated aging times at 80°C.

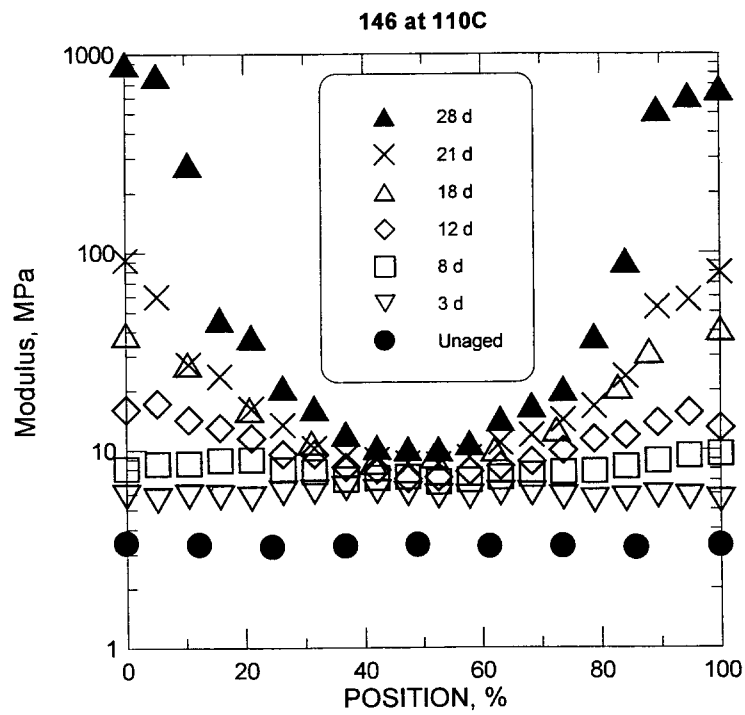


Figure 22. Modulus profiles of Material 146 after the indicated aging times at 110°C.

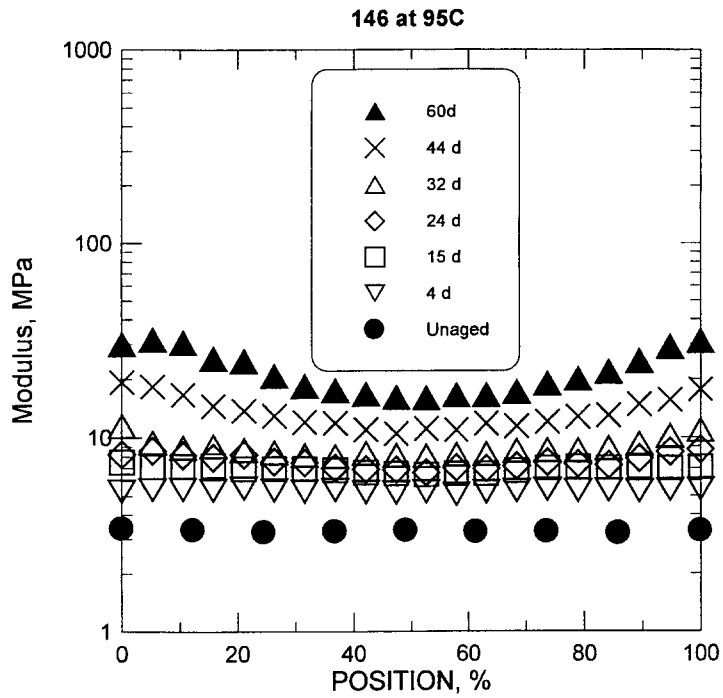


Figure 23. Modulus profiles of Material 146 after the indicated aging times at 95°C.

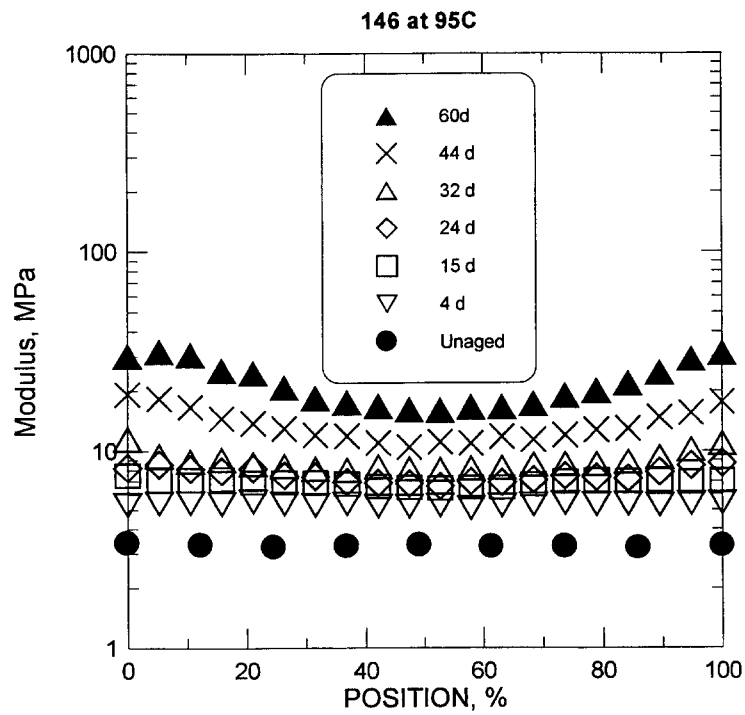


Figure 24. Modulus profiles of Material 146 after the indicated aging times at 80°C.

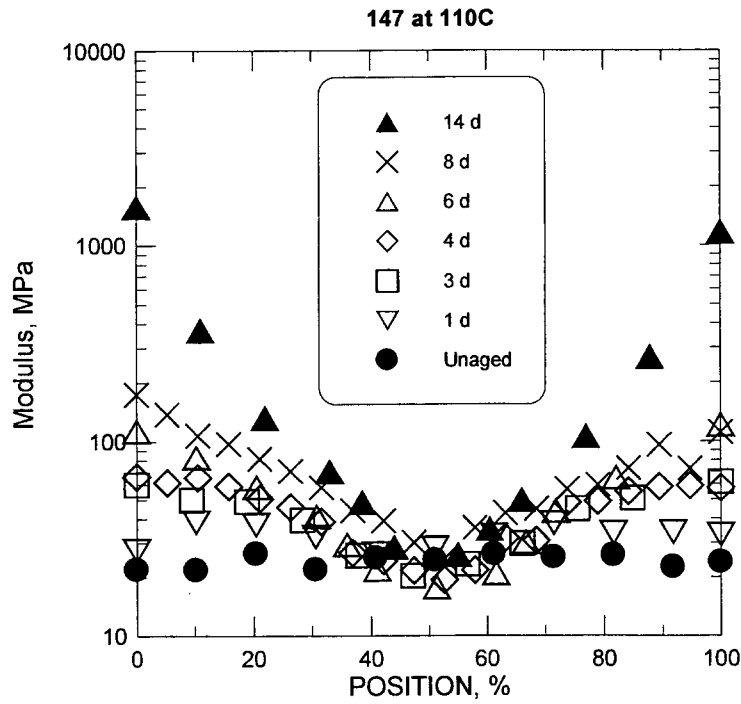


Figure 25. Modulus profiles of Material 147 after the indicated aging times at 110°C.

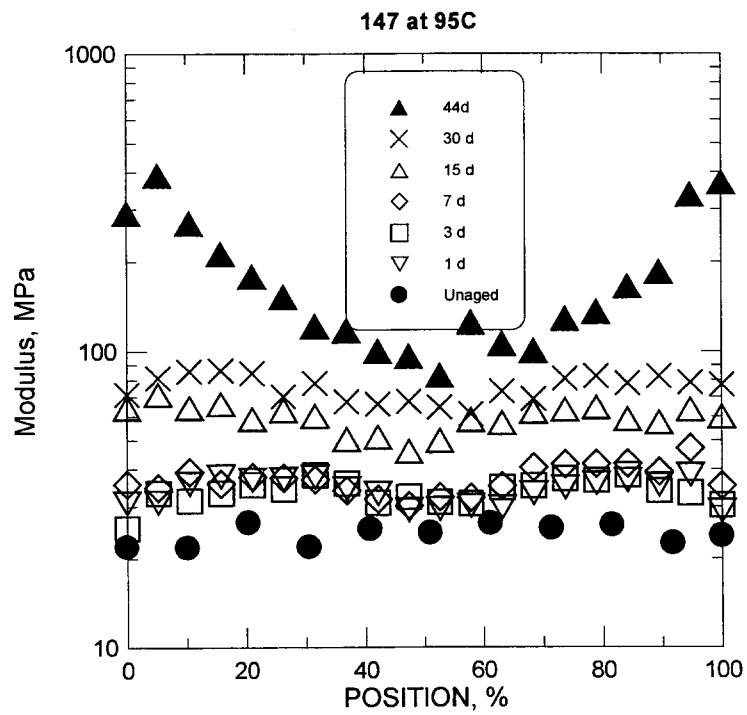


Figure 26. Modulus profiles of Material 147 after the indicated aging times at 95°C.

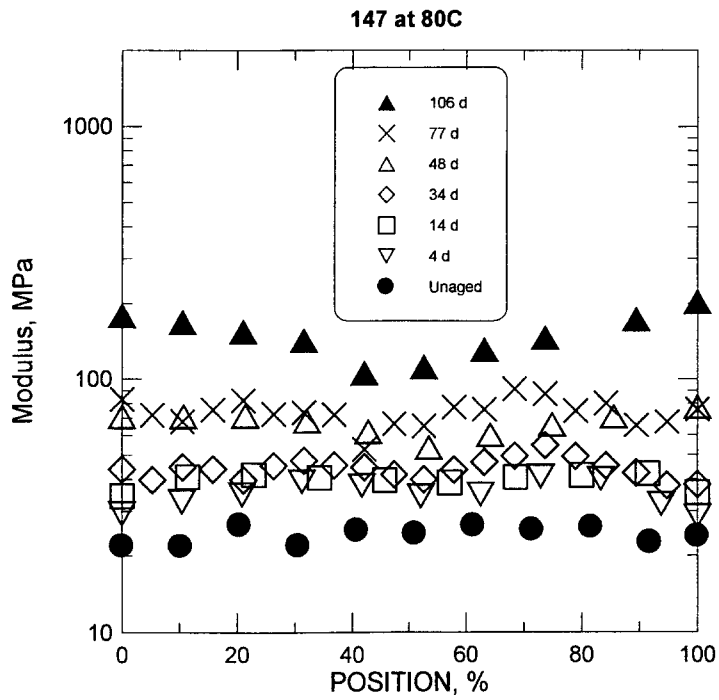


Figure 27. Modulus profiles of Material 147 after the indicated aging times at 80°C.

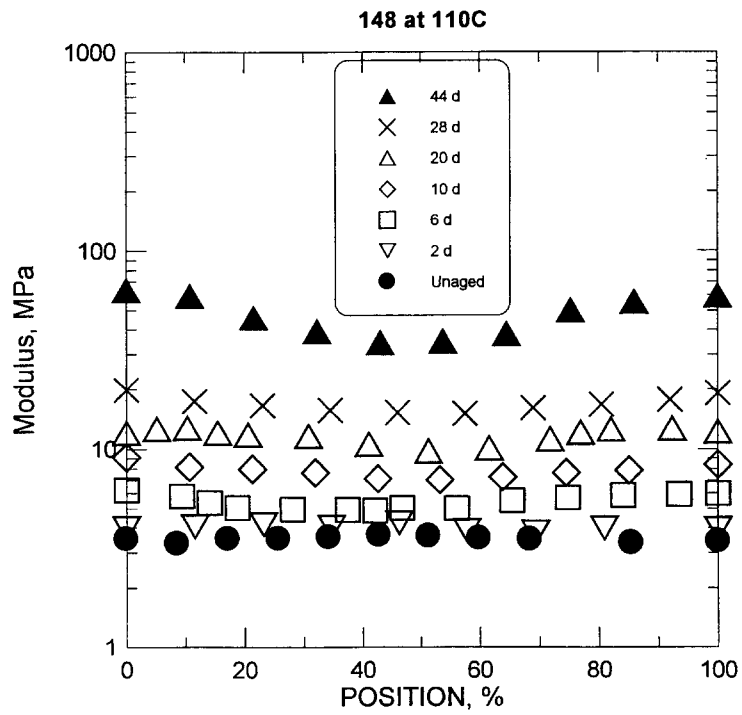


Figure 28. Modulus profiles of Material 148 after the indicated aging times at 110°C.

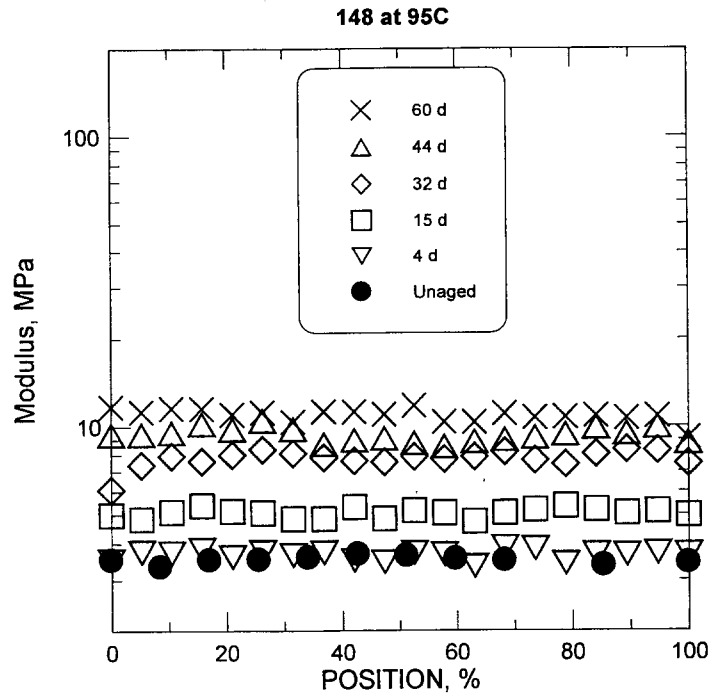


Figure 29. Modulus profiles of Material 148 after the indicated aging times at 95°C.

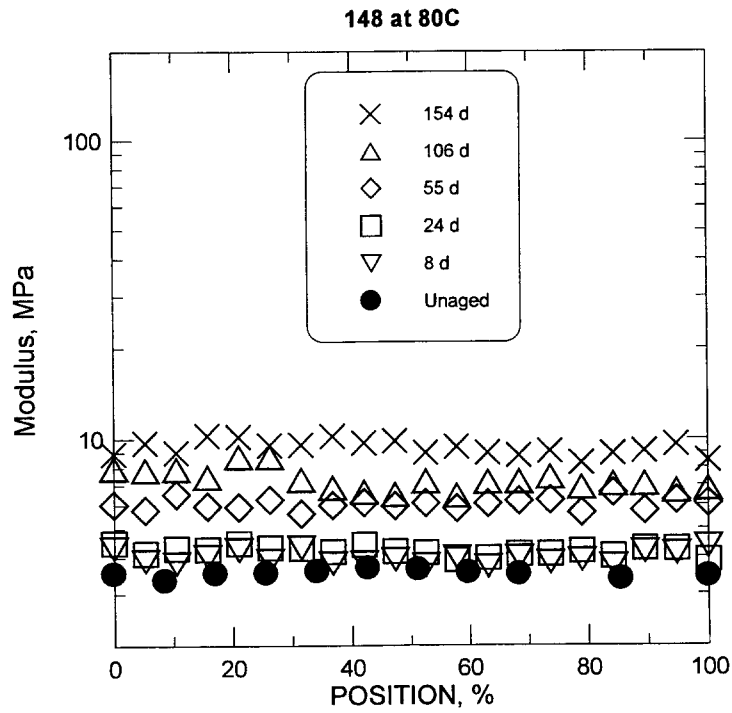


Figure 30. Modulus profiles of Material 148 after the indicated aging times at 80°C.

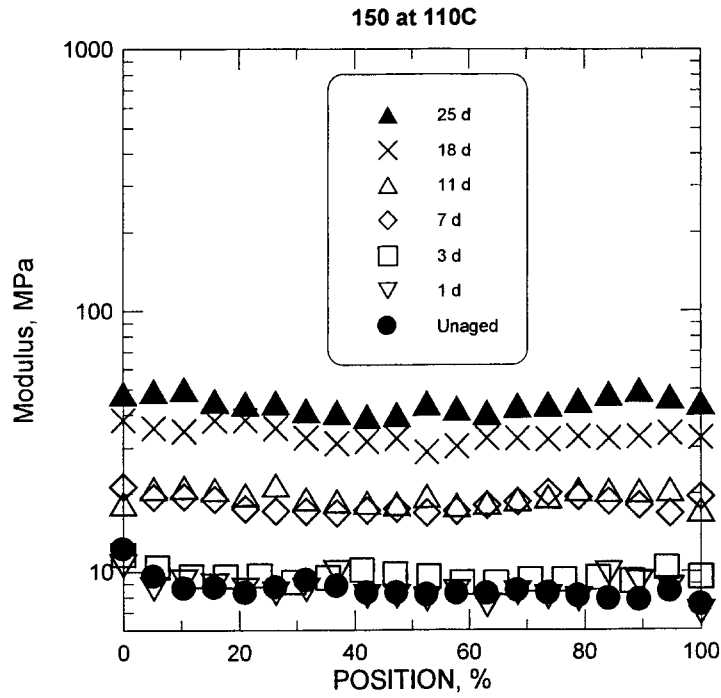


Figure 31. Modulus profiles of Material 150 after the indicated aging times at 110°C.

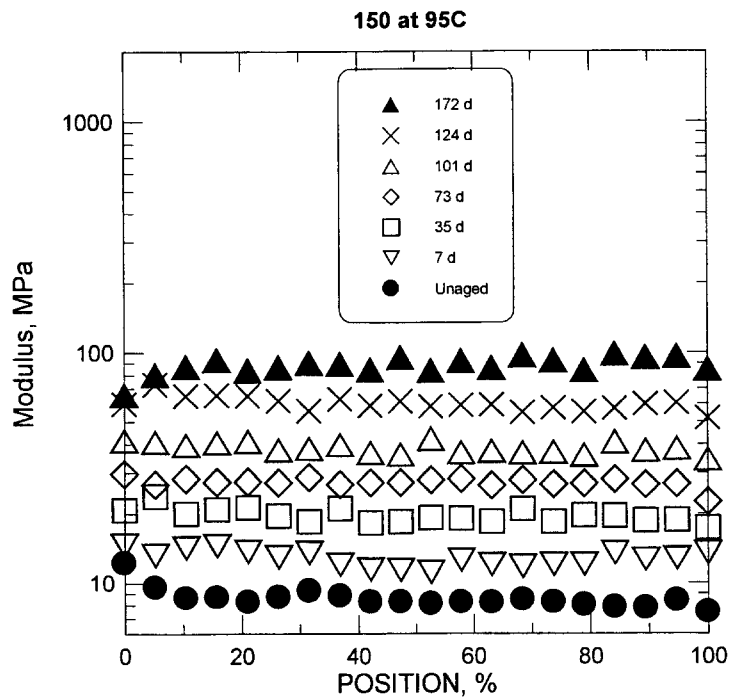


Figure 32. Modulus profiles of Material 150 after the indicated aging times at 95°C.

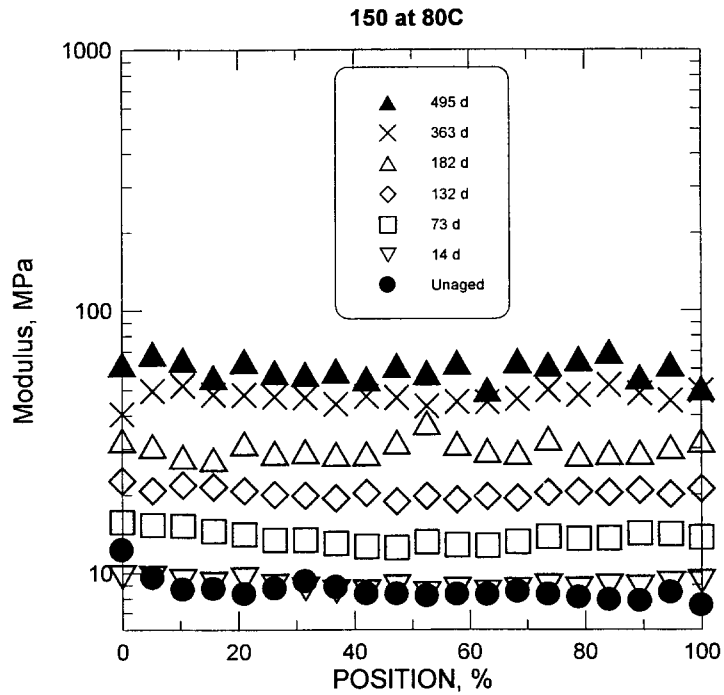


Figure 33. Modulus profiles of Material 150 after the indicated aging times at 80°C.

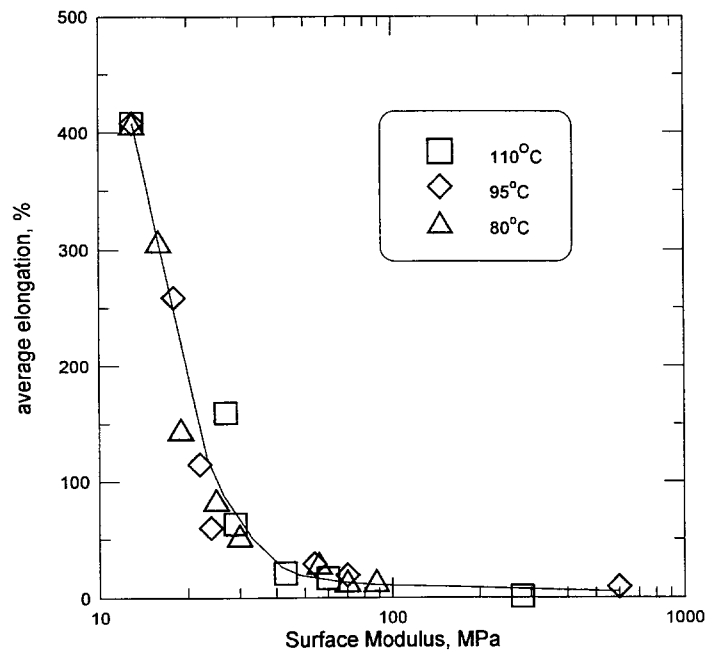


Figure 34. Elongation versus surface modulus for Material 145 (thick).

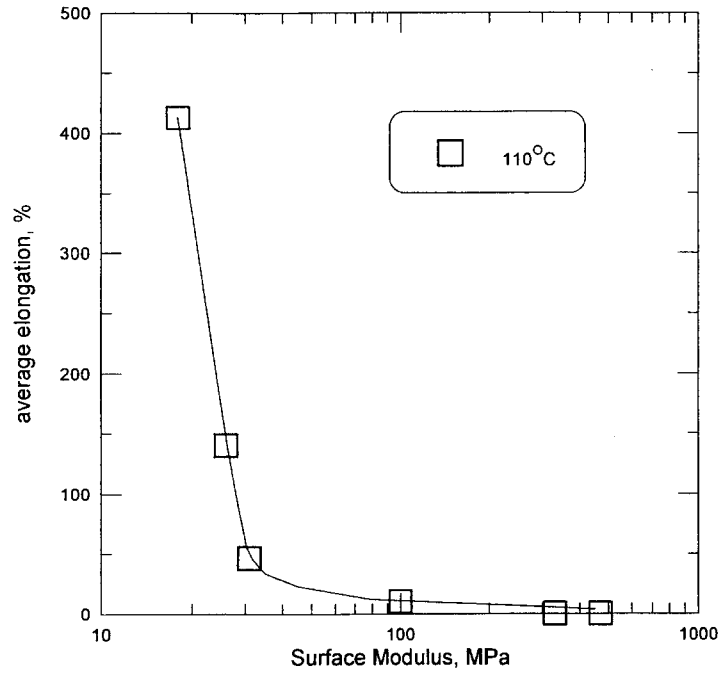


Figure 35. Elongation versus surface modulus for Material 145 (thin).

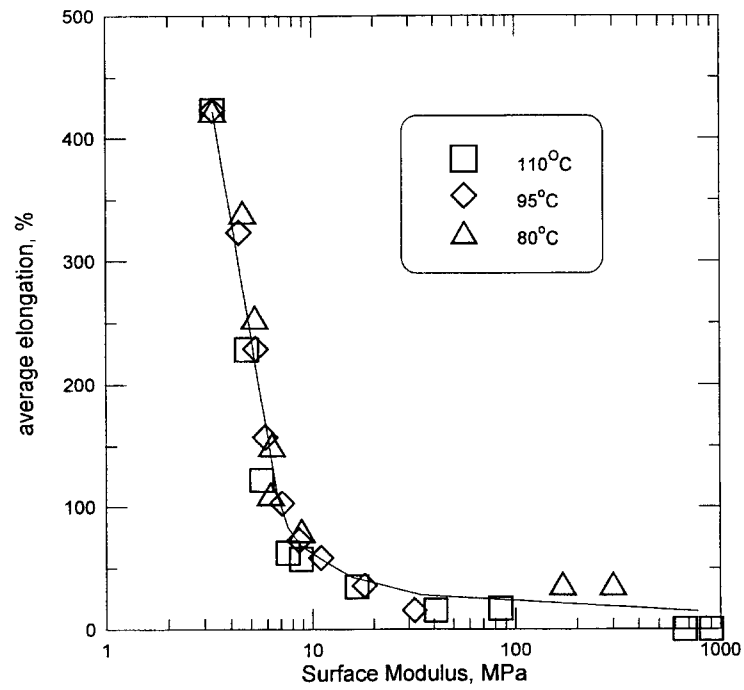


Figure 36. Elongation versus surface modulus for Material 146.

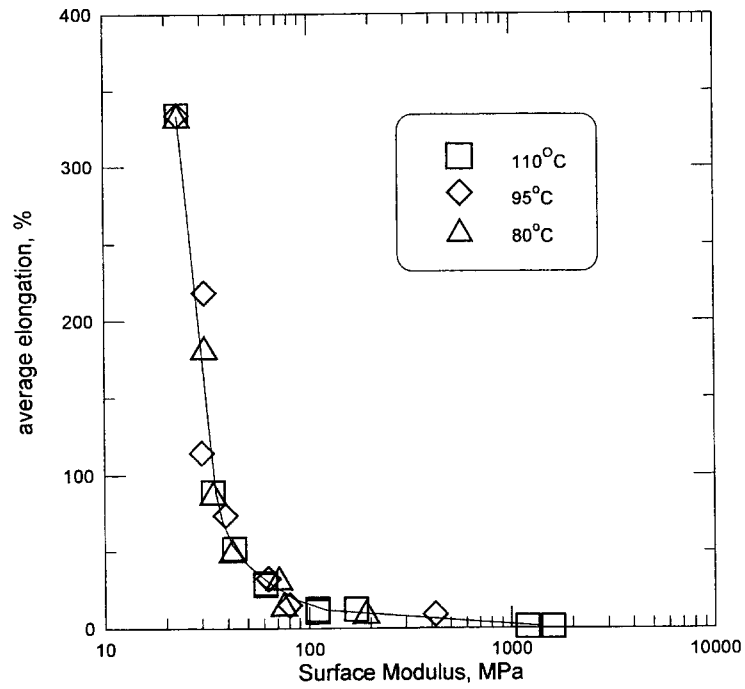


Figure 37. Elongation versus surface modulus for Material 147.

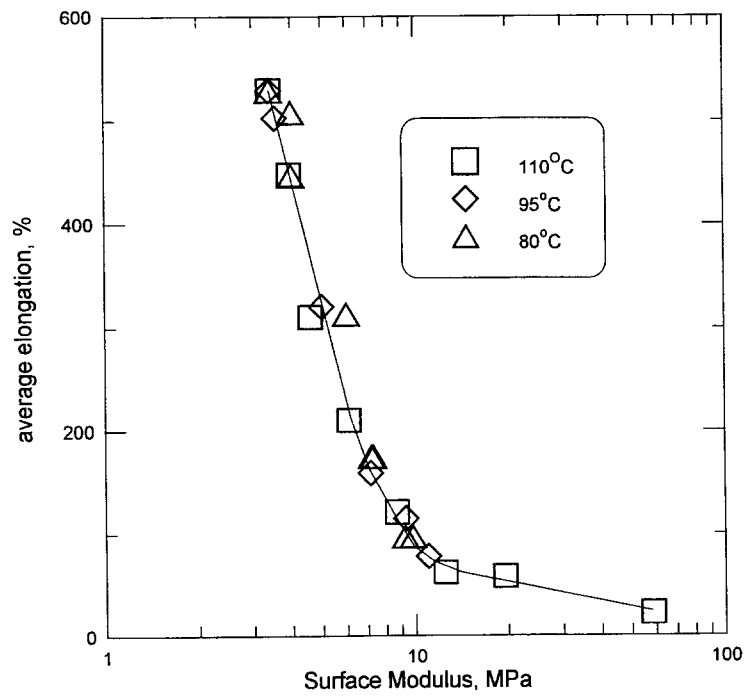


Figure 38. Elongation versus surface modulus for Material 148.

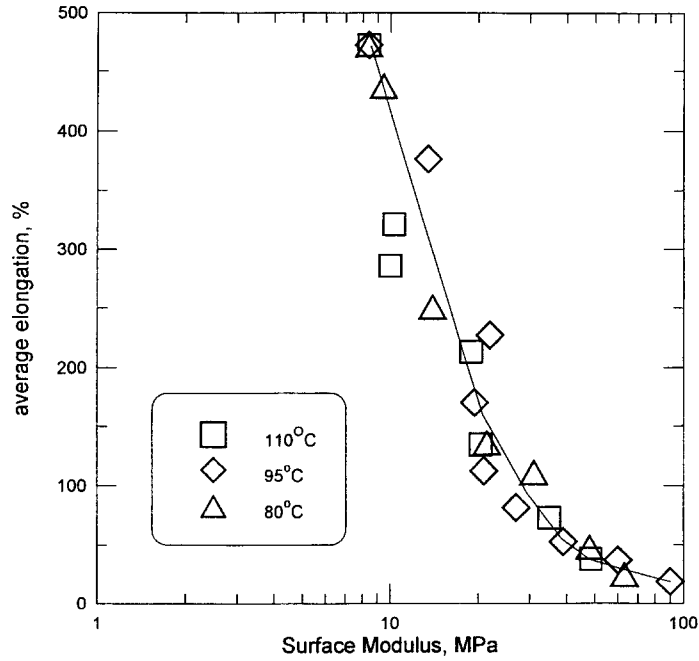
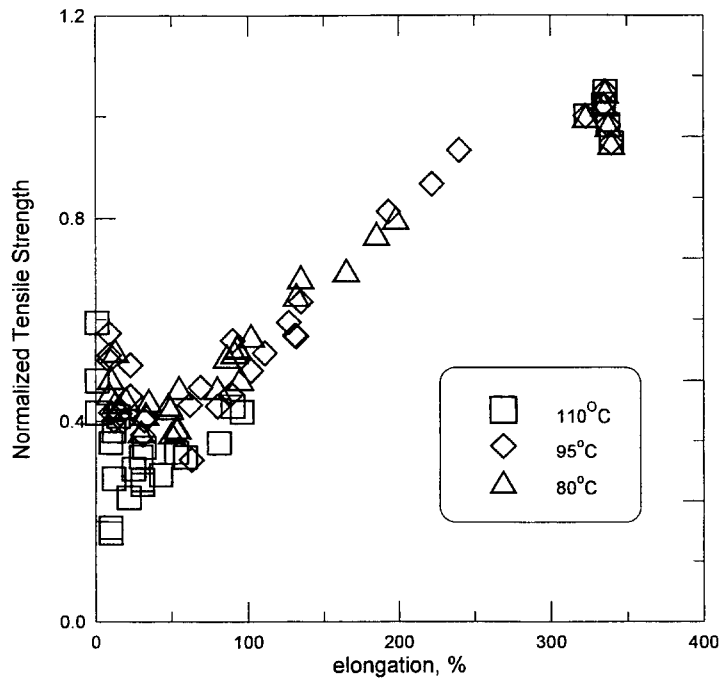


Figure 39. Elongation versus surface modulus for Material 150.



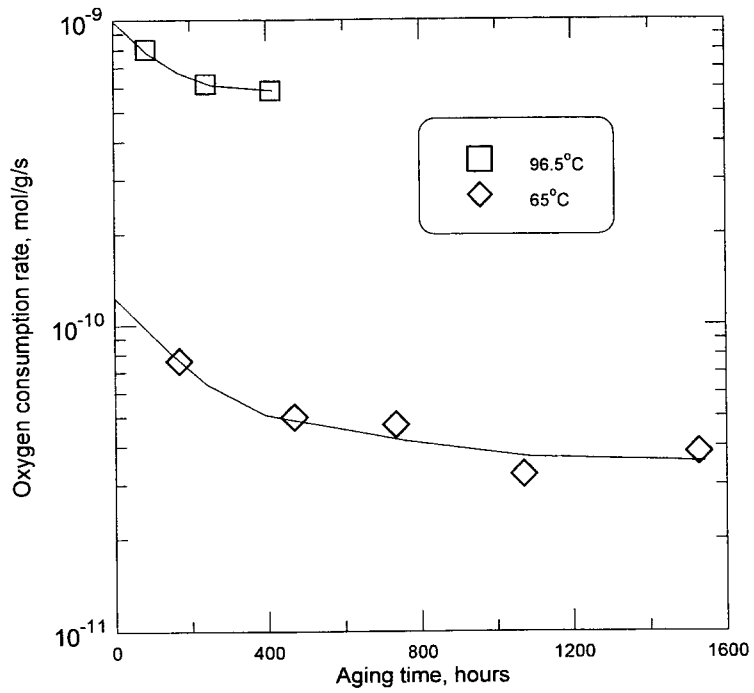


Figure 41. Oxygen consumption rate results for Material 145.

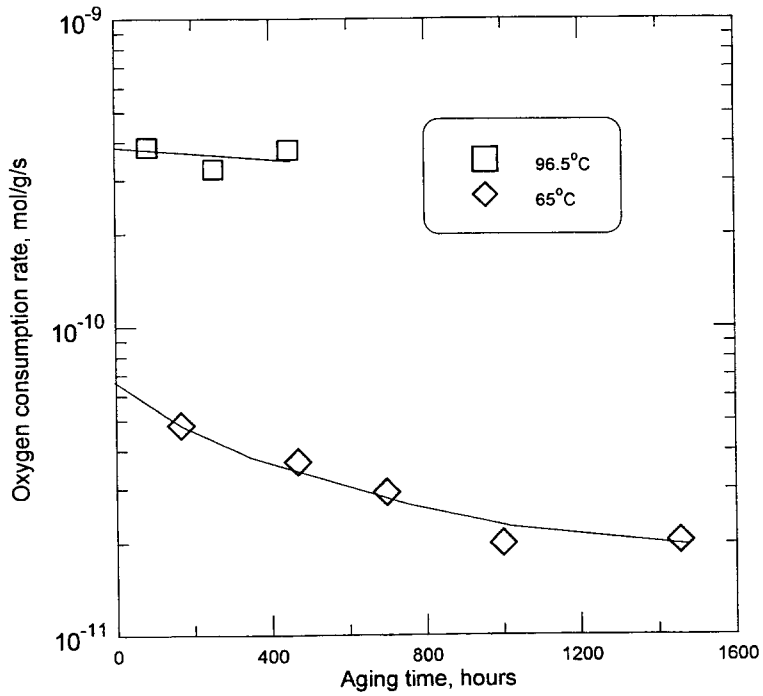


Figure 42. Oxygen consumption rate results for Material 146.

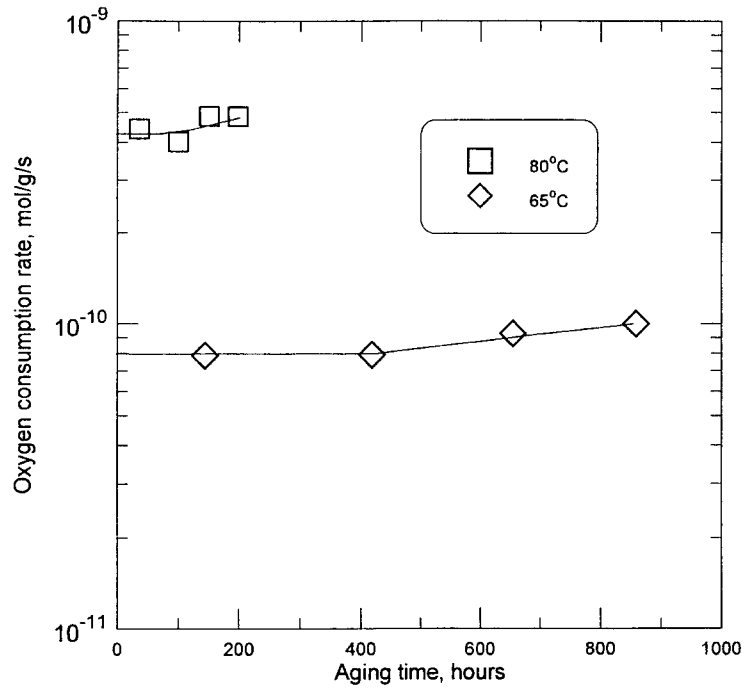


Figure 43. Oxygen consumption rate results for Material 147.

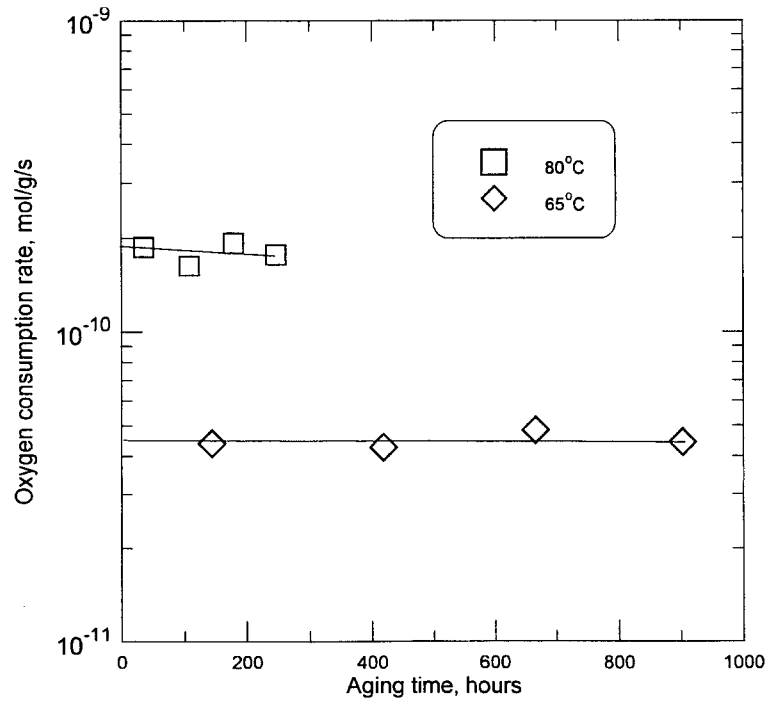


Figure 44. Oxygen consumption rate results for Material 148.

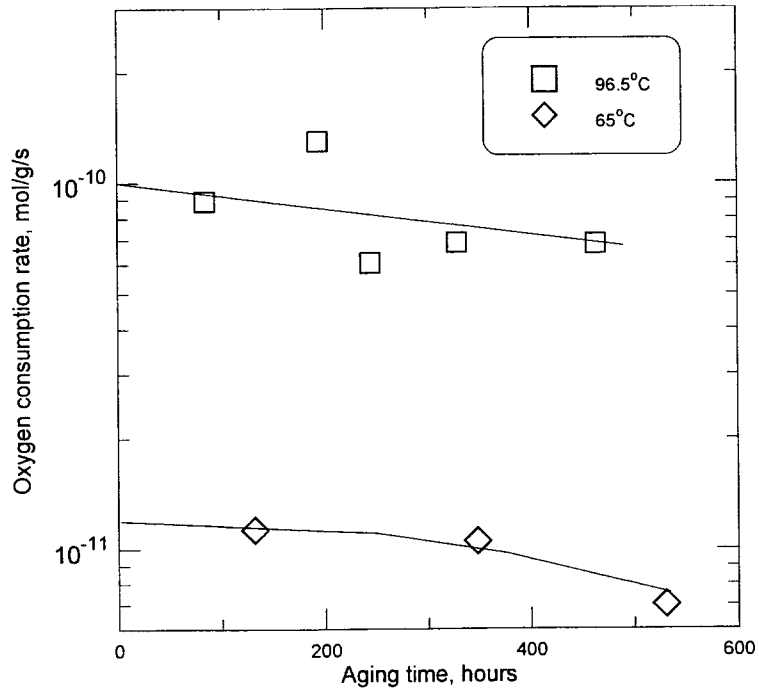


Figure 45. Oxygen consumption rate results for Material 149.

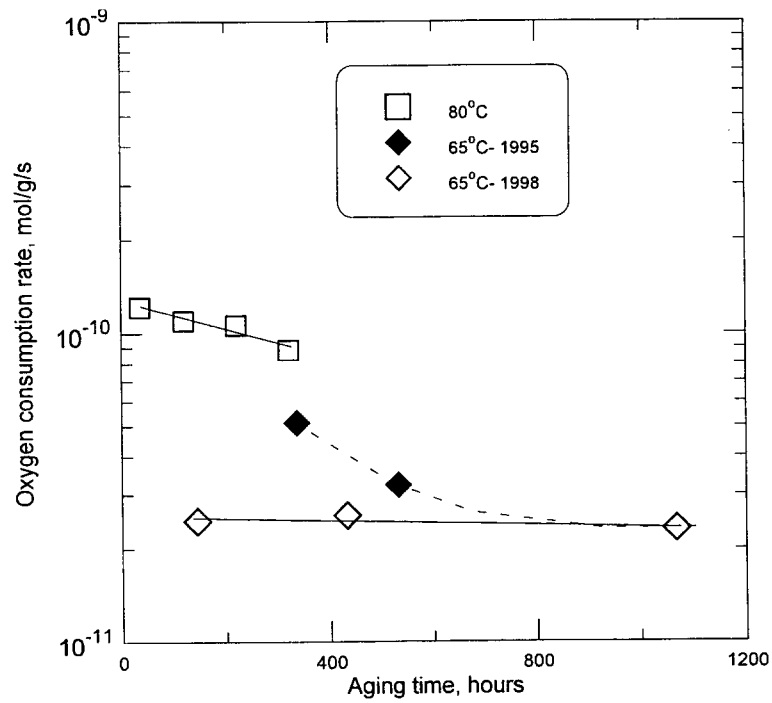


Figure 46. Oxygen consumption rate results for Material 150.

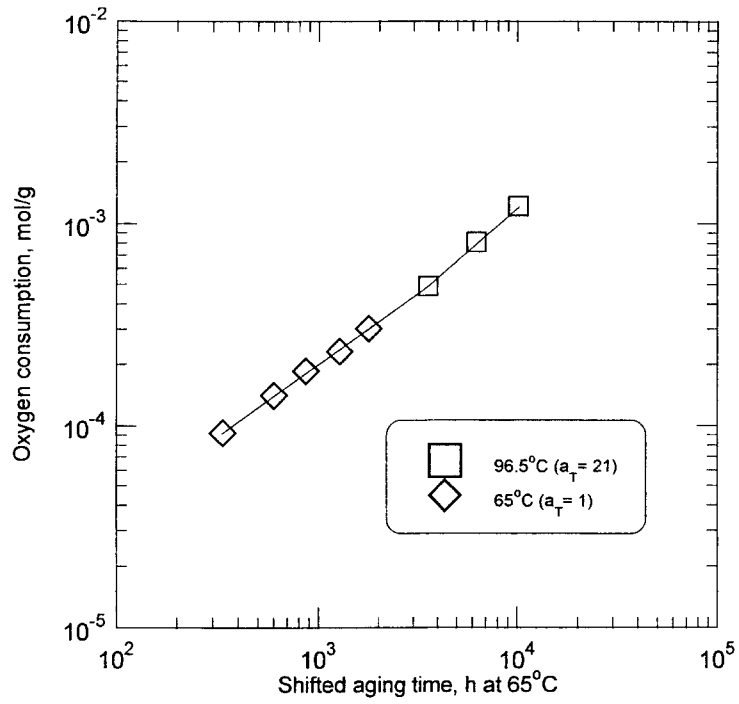


Figure 47. Time-temperature superposed oxygen consumption data for Material 145.

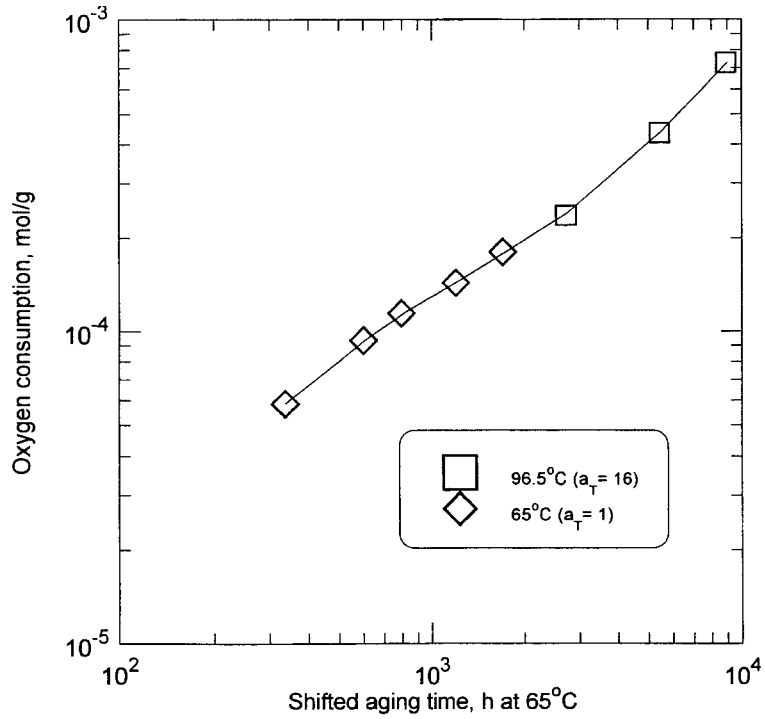


Figure 48. Time-temperature superposed oxygen consumption data for Material 146.

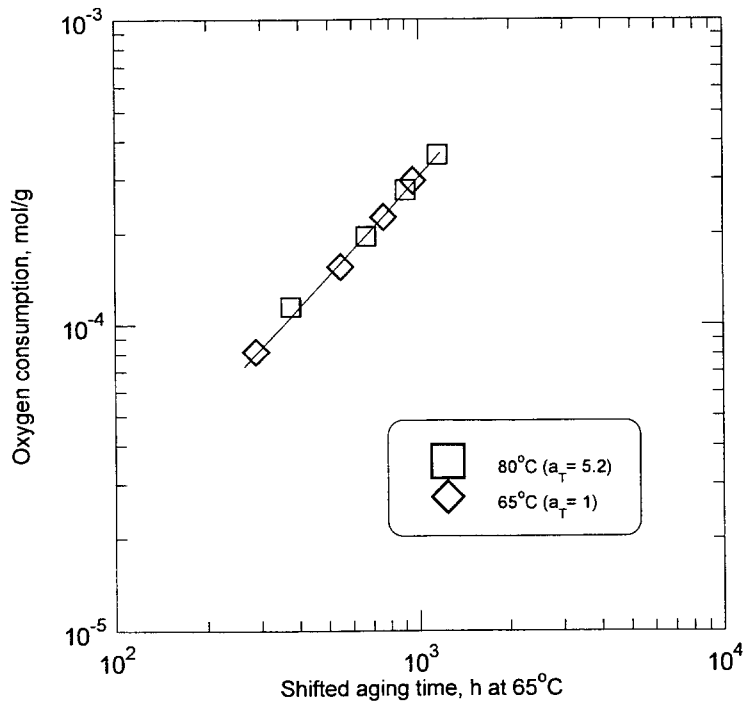


Figure 49. Time-temperature superposed oxygen consumption data for Material 147.

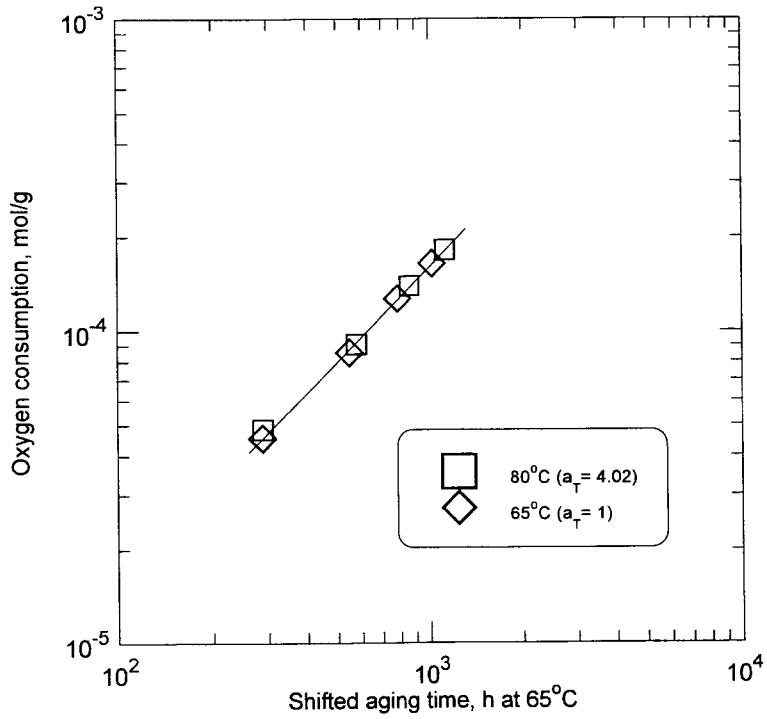


Figure 50. Time-temperature superposed oxygen consumption data for Material 148.

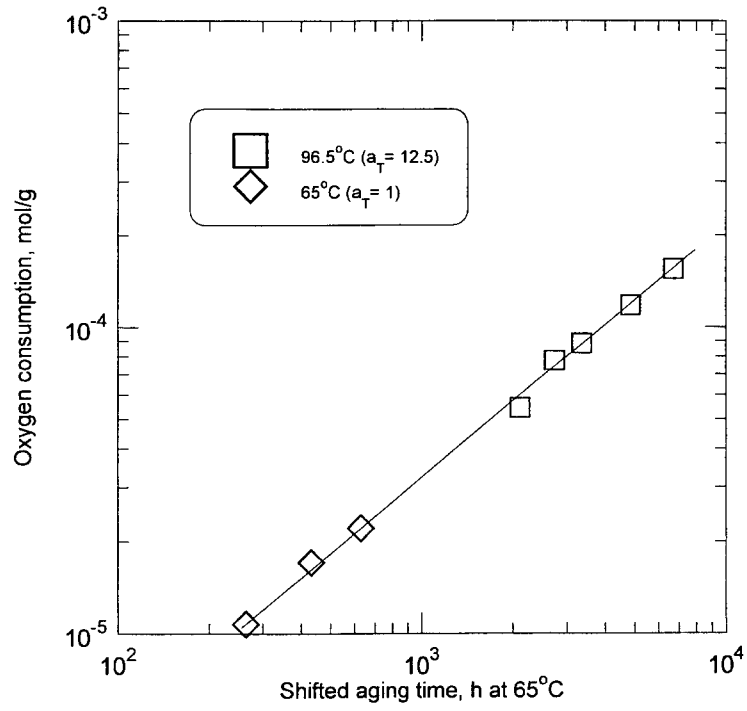


Figure 51. Time-temperature superposed oxygen consumption data for Material 149.

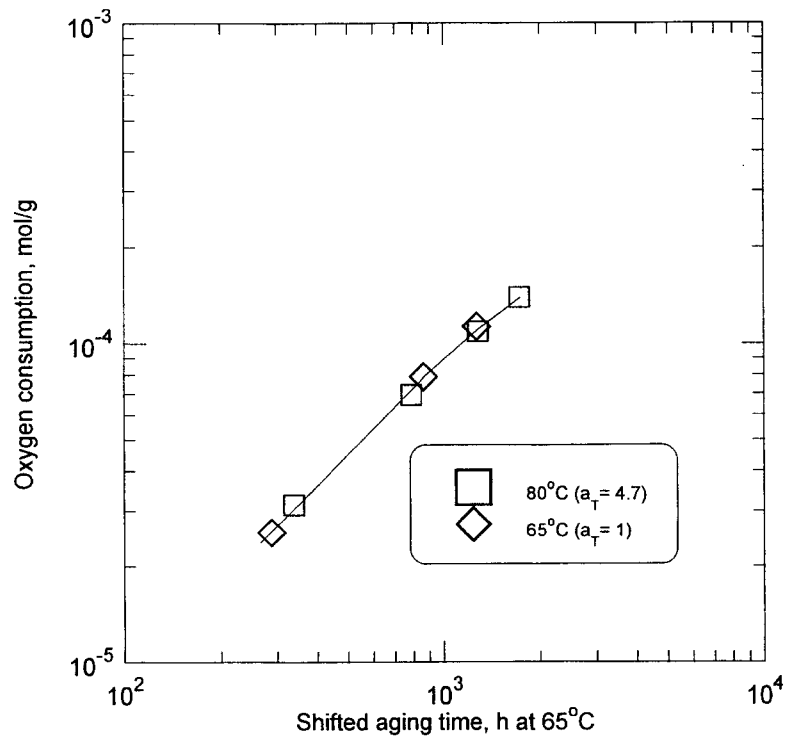


Figure 52. Time-temperature superposed oxygen consumption data for Material 150.

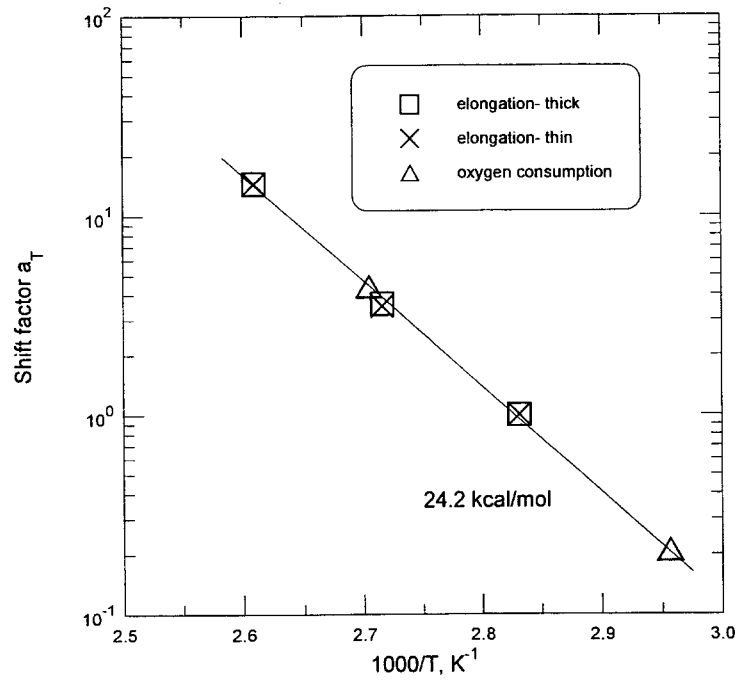


Figure 53. Arrhenius plot for elongation and oxygen consumption of Material 145.

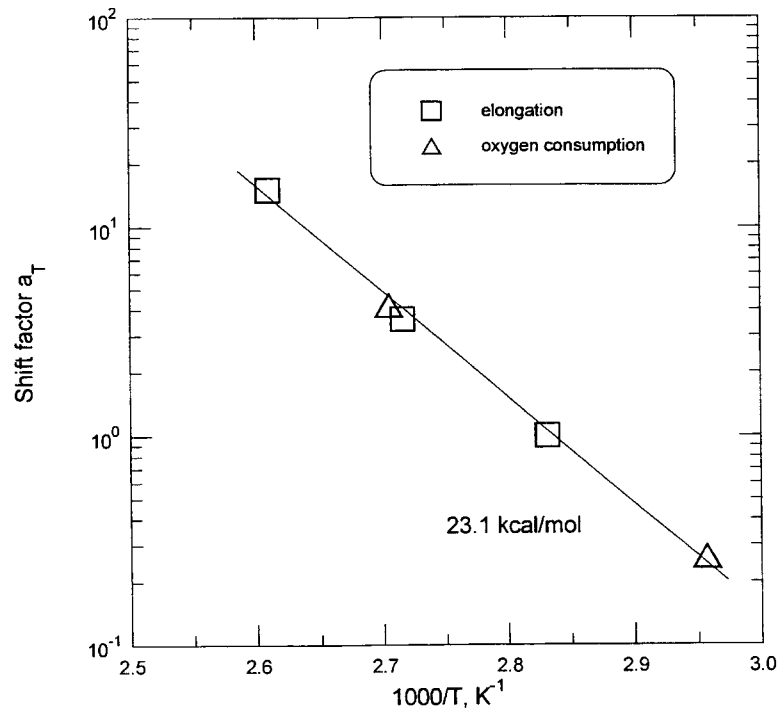


Figure 54. Arrhenius plot for elongation and oxygen consumption of Material 146.

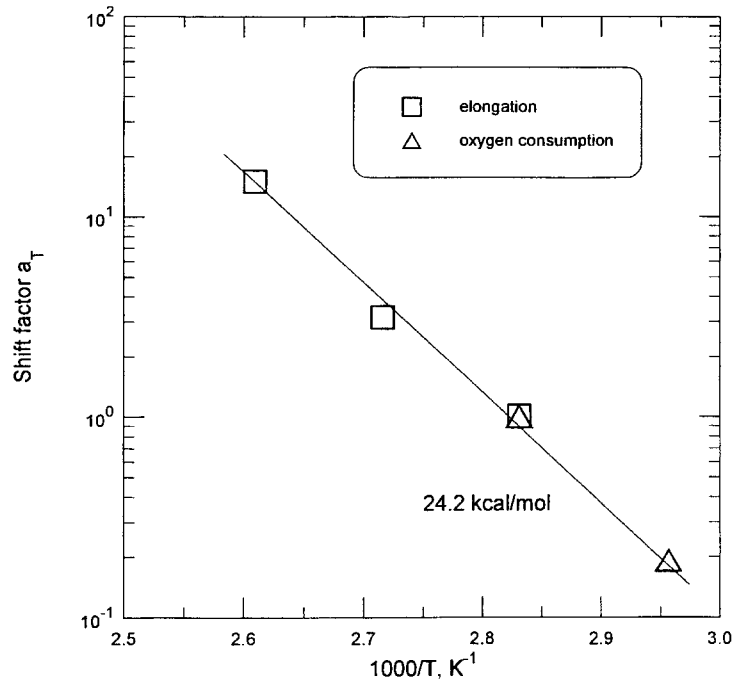


Figure 55. Arrhenius plot for elongation and oxygen consumption of Material 147.

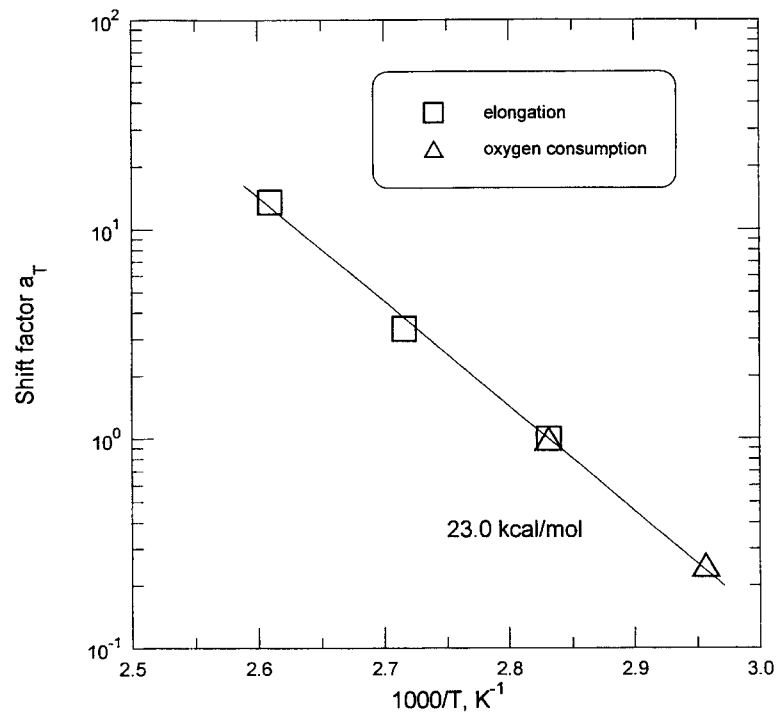


Figure 56. Arrhenius plot for elongation and oxygen consumption of Material 148.

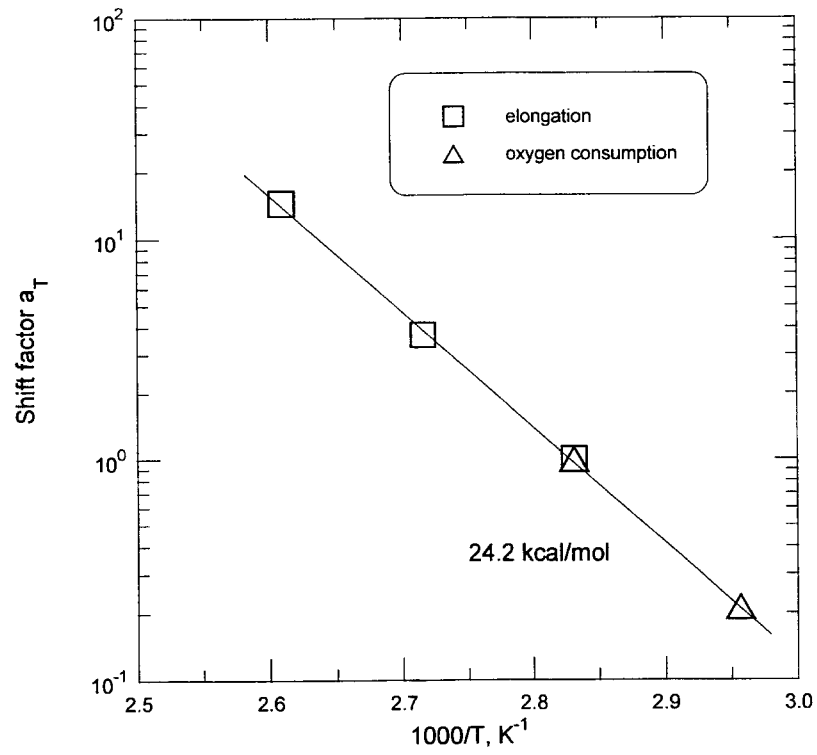


Figure 57. Arrhenius plot for elongation and oxygen consumption of Material 150.

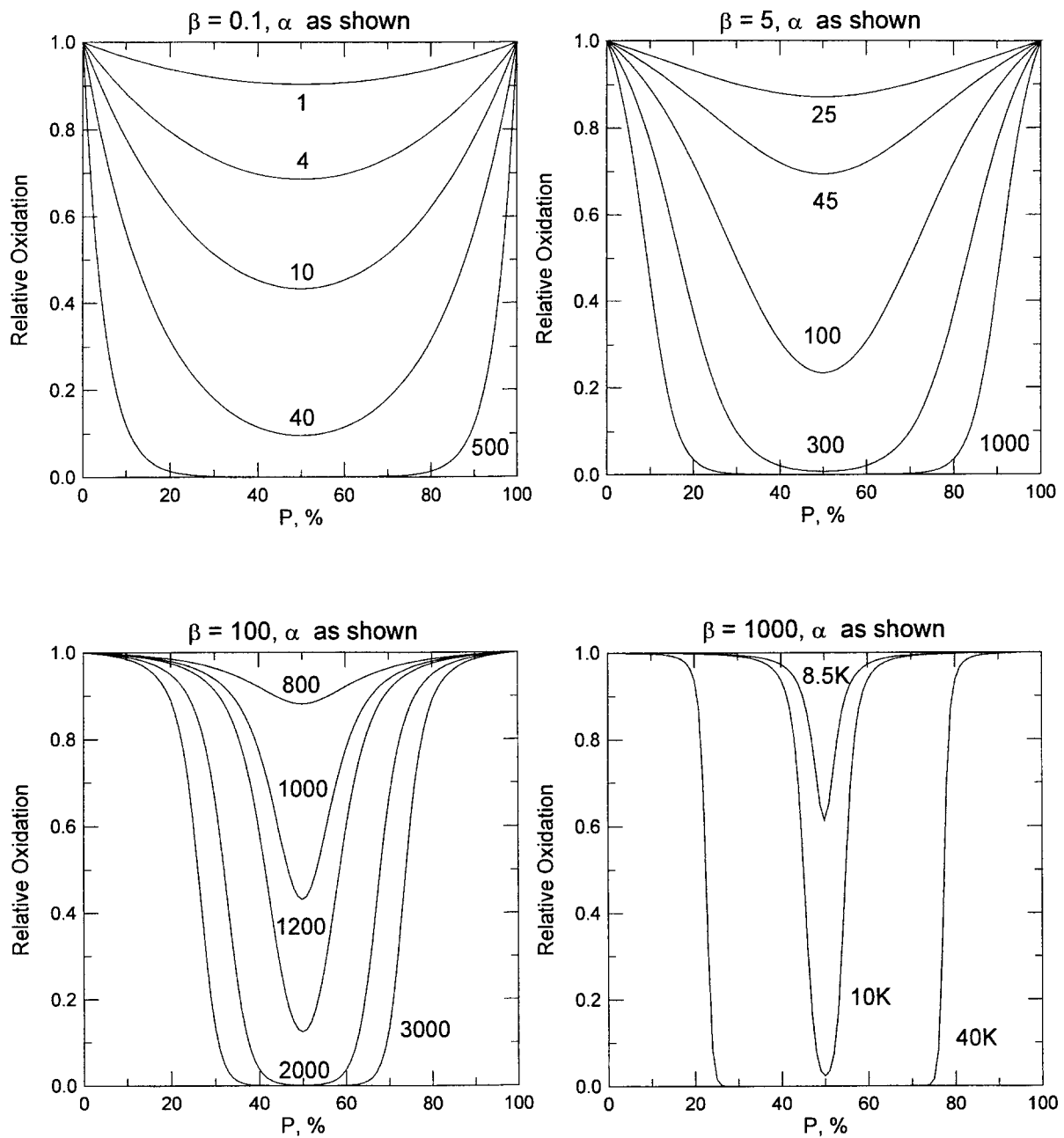


Figure 58. Theoretical relative oxidation profiles for planar material surrounded by oxygen on both sides as a function of various combinations of the diffusion-limited oxidation parameters α and β .

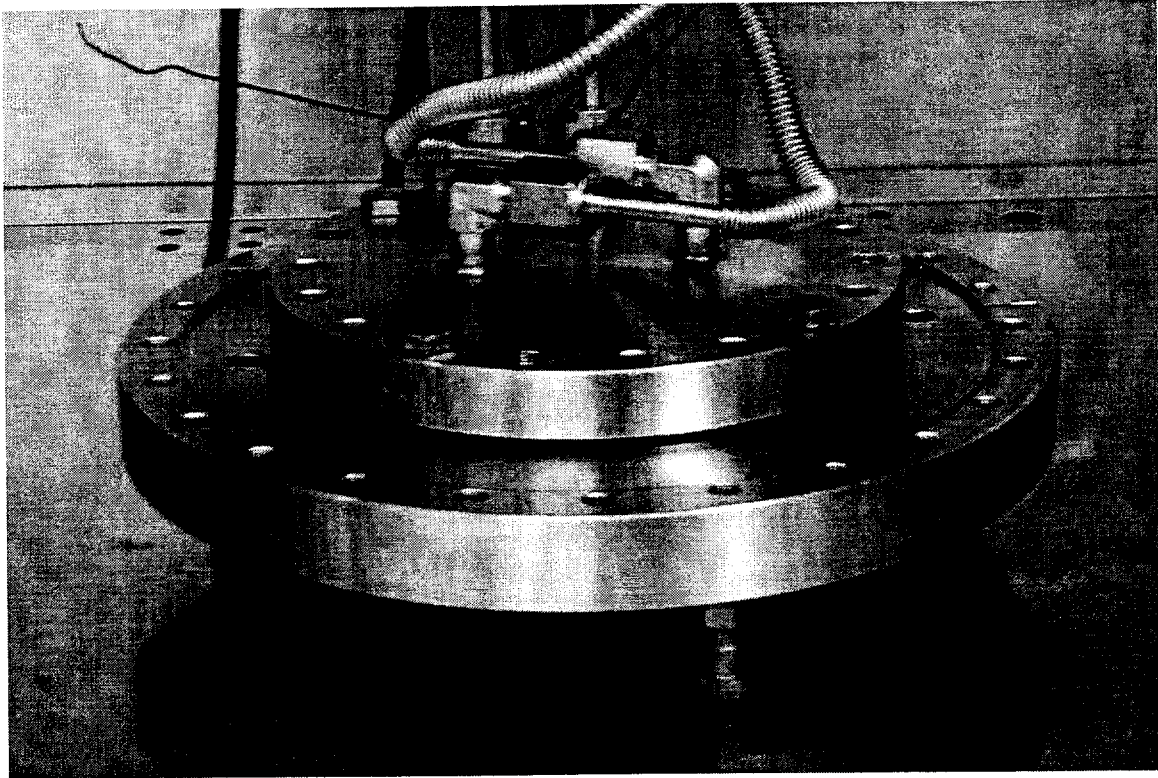


Figure 59. New sample holder region of oxygen permeation apparatus.

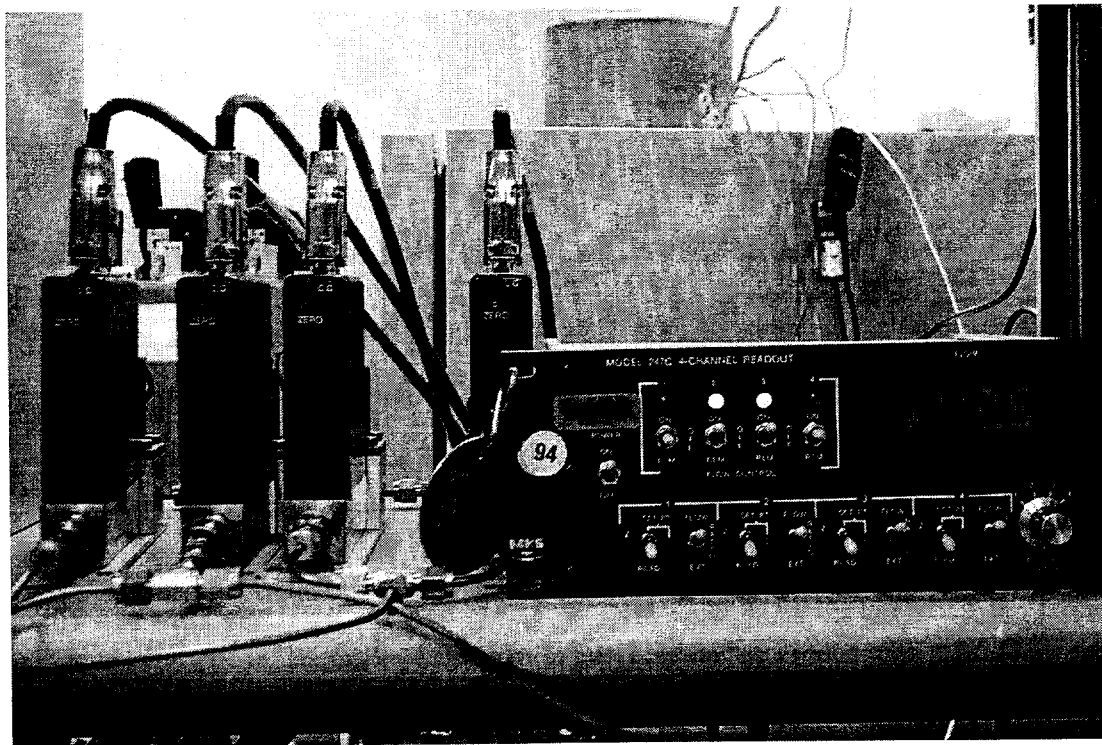


Figure 60. MKS flow meters and controllers for accurate gas flow.

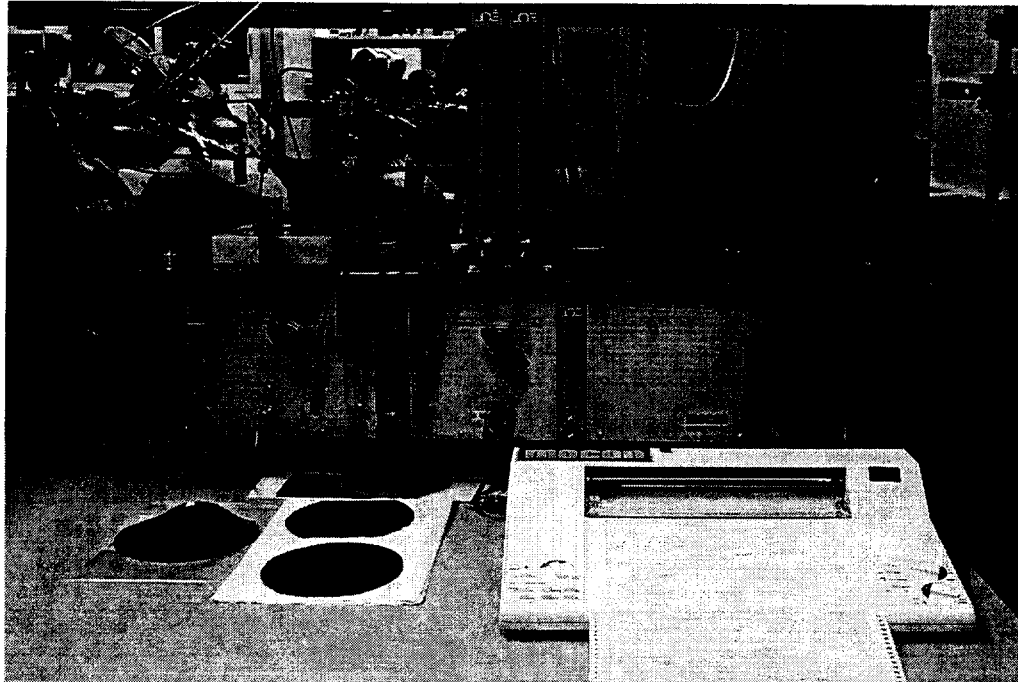


Figure 61. Photograph of modified oxygen permeability apparatus.

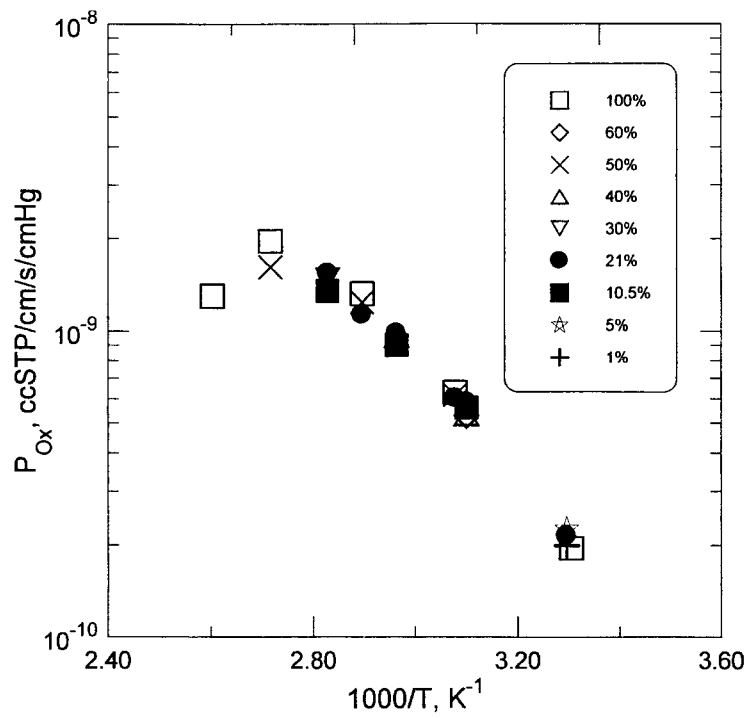


Figure 62. Temperature-dependent oxygen permeability results versus oxygen partial pressure without corrections for reaction.

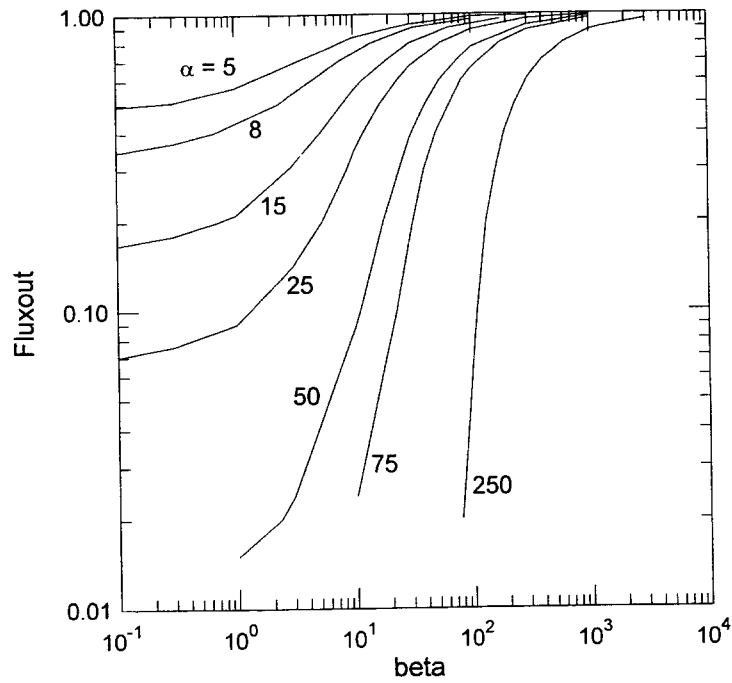


Figure 63. Theoretical curves versus α and β for the fractional reduction in flux (Fluxout) relative to the flux expected if no reaction occurred.

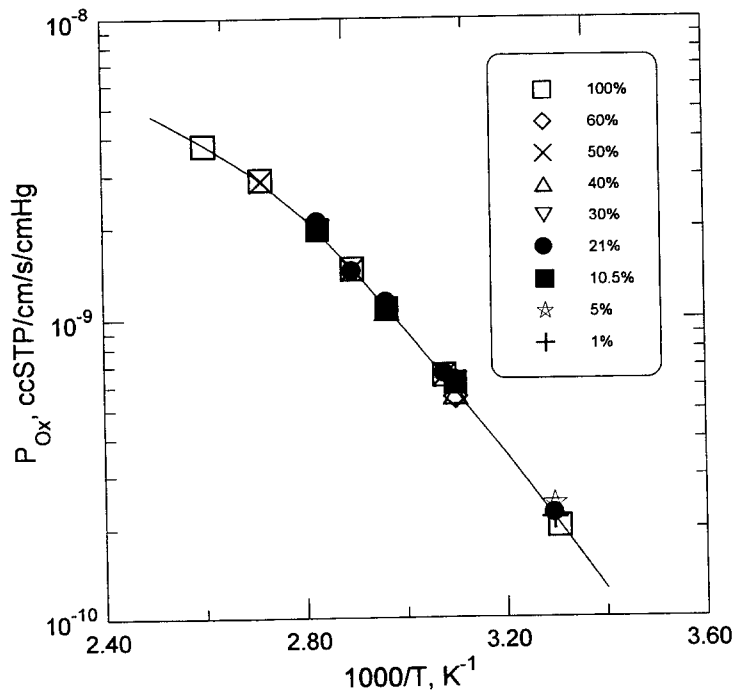


Figure 64. Temperature-dependent oxygen permeability results versus oxygen partial pressure with corrections for reaction.

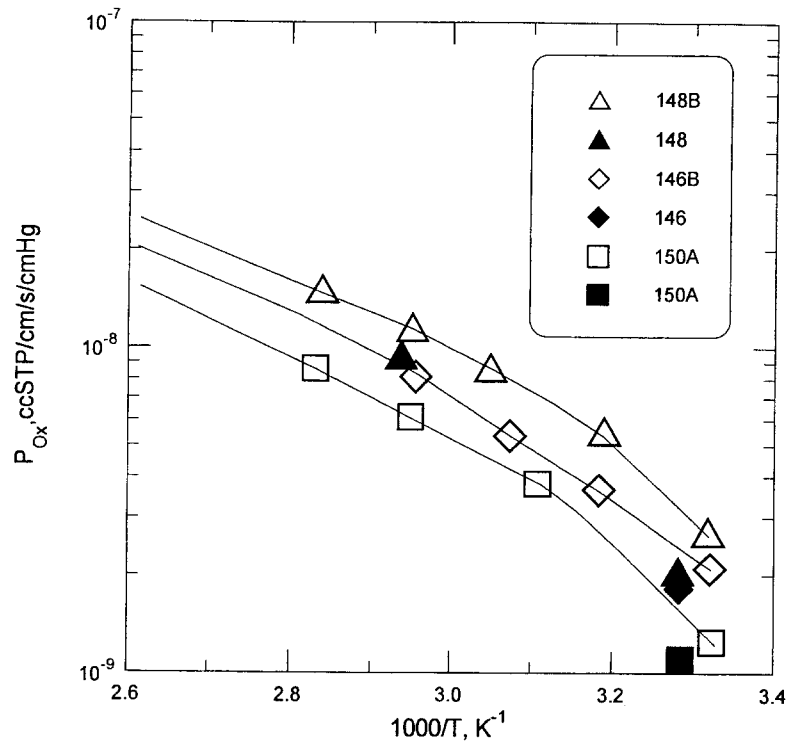


Figure 65. Temperature-dependent oxygen permeability coefficients for Materials 146, 148 and 150.

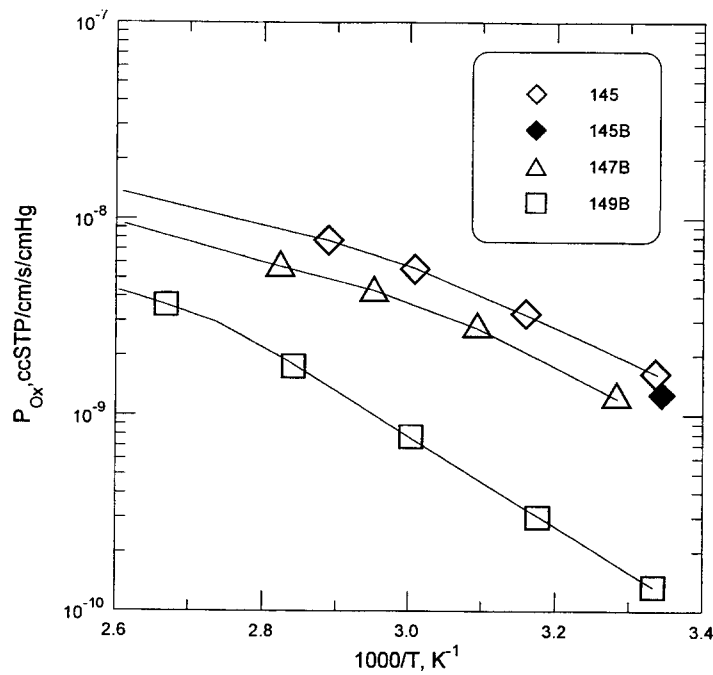


Figure 66. Temperature-dependent oxygen permeability coefficients for Materials 145 and 147.

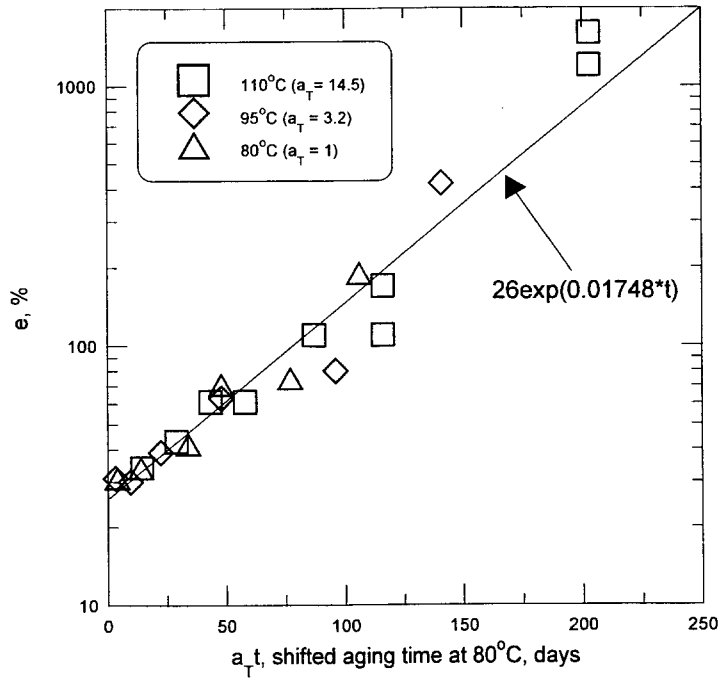


Figure 67. Time-temperature superposition of surface modulus values for Material 147.

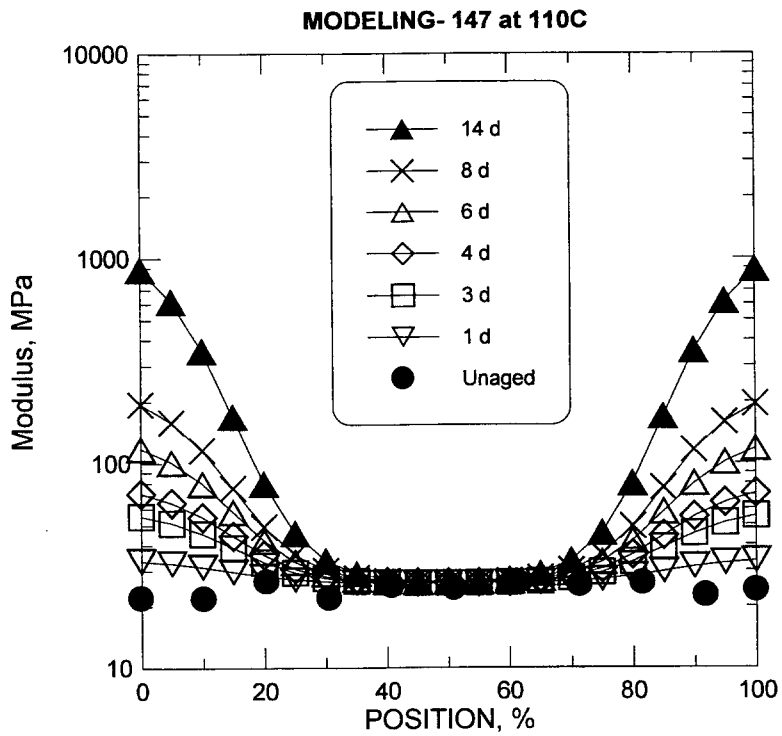


Figure 68. Theoretical modeling of modulus profiles for Material 147 at 110°C.

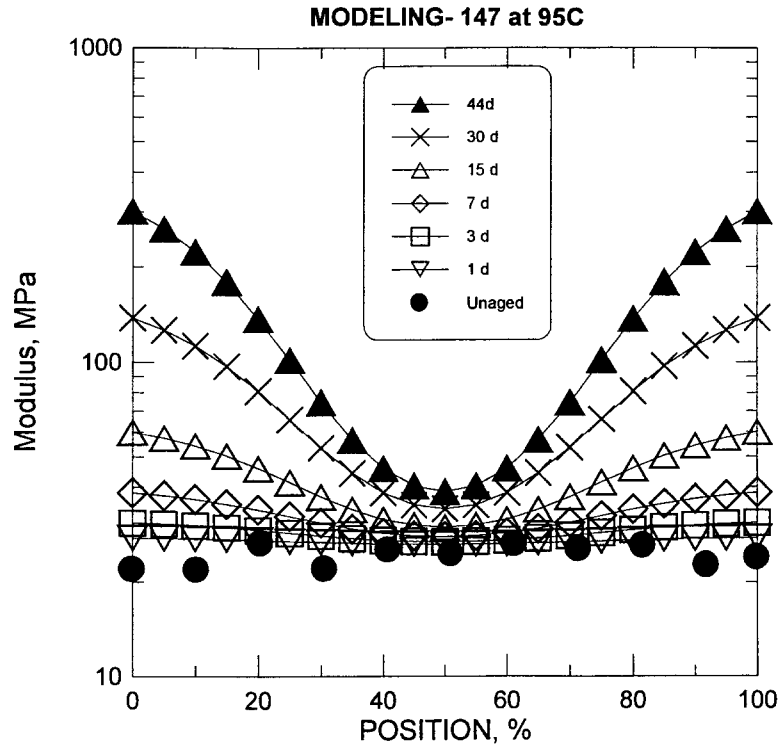


Figure 69. Theoretical modeling of modulus profiles for Material 147 at 95°C

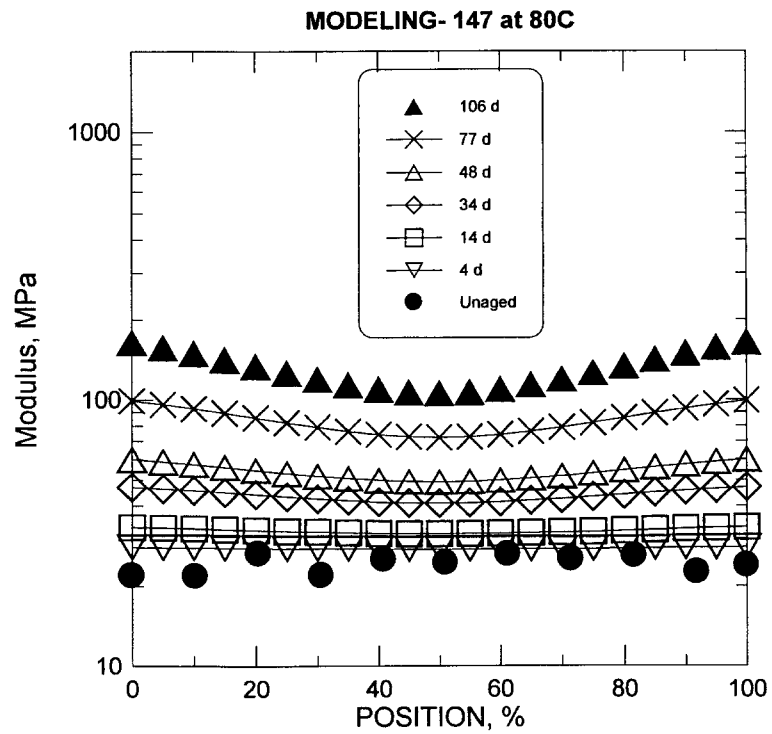


Figure 70. Theoretical modeling of modulus profiles for Material 147 at 80°C.

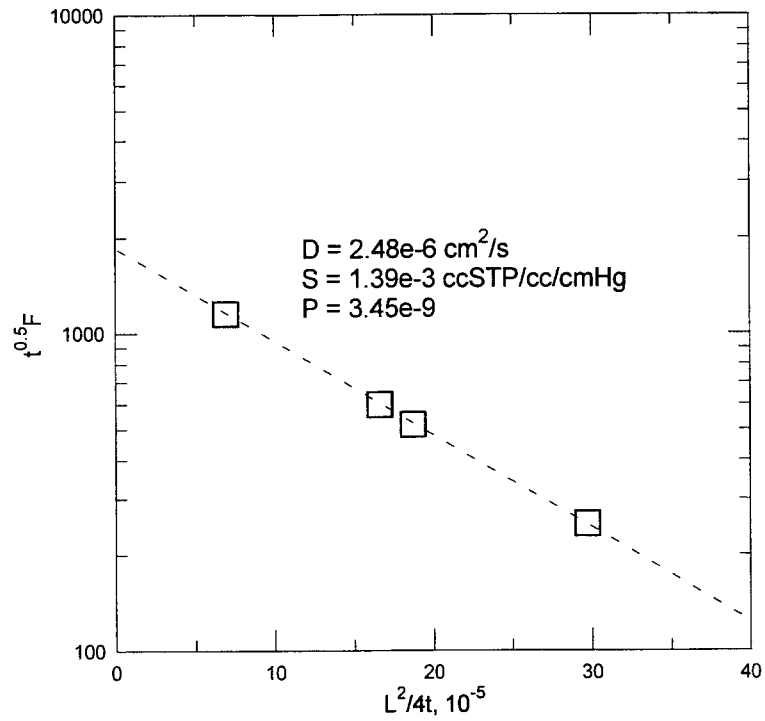


Figure 71. Plot of $\log[F(t^{0.5})]$ versus $l^2/(4t)$ for EPDM material.

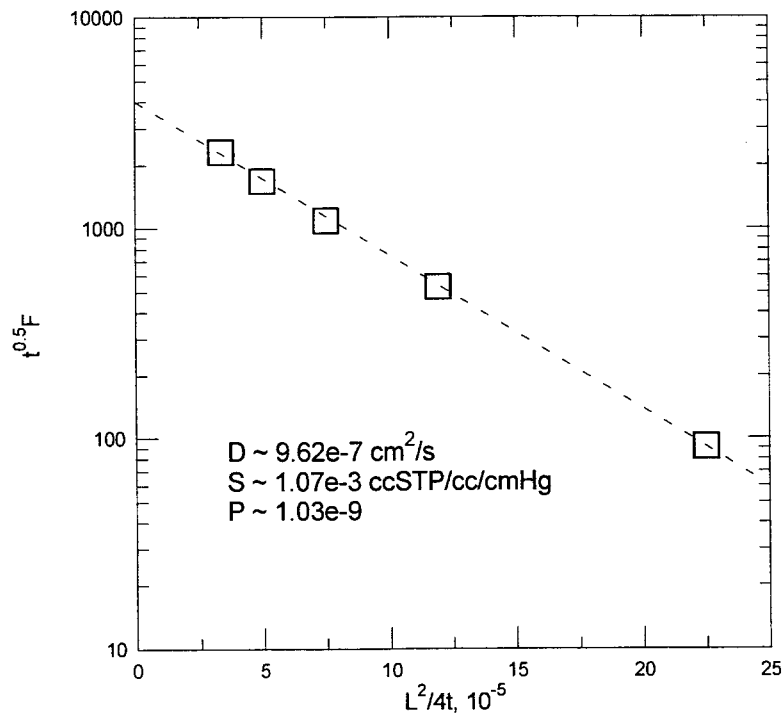


Figure 72. Plot of $\log[F(t^{0.5})]$ versus $l^2/(4t)$ for Material 147.

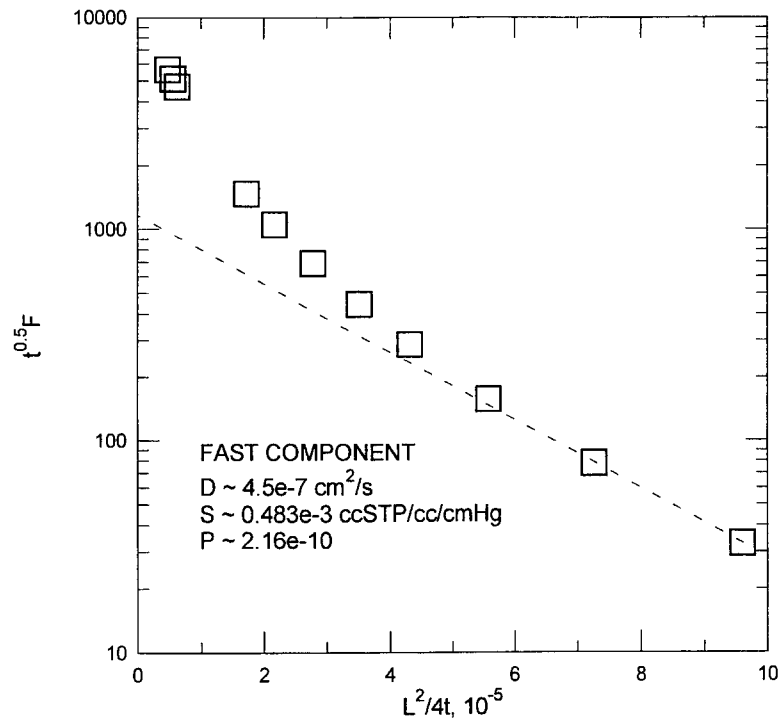


Figure 73. Plot of $\log[F(t^{0.5})]$ versus $l^2/(4t)$ for Material 150.

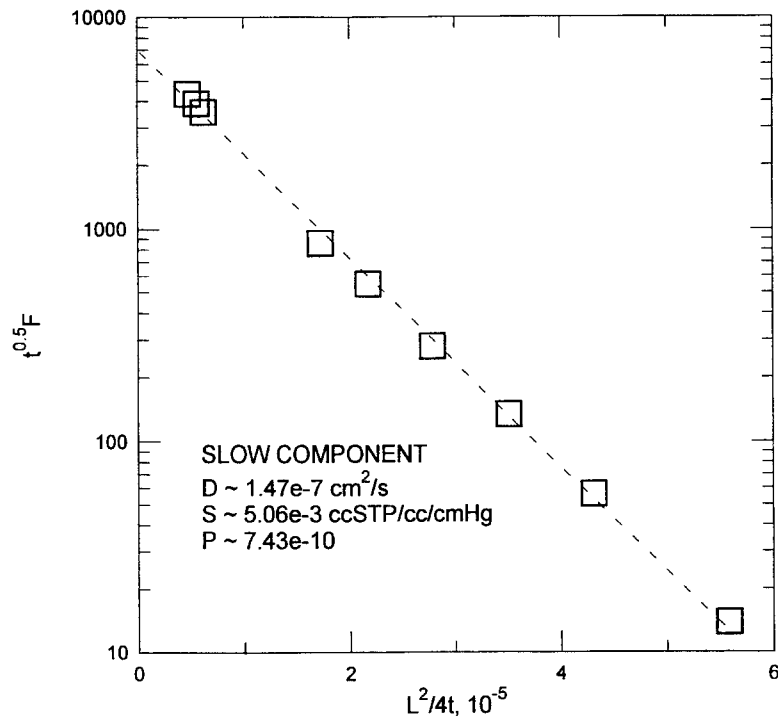


Figure 74. Plot of $\log[F(t^{0.5})]$ versus $l^2/(4t)$ for the slow component of Material 150.

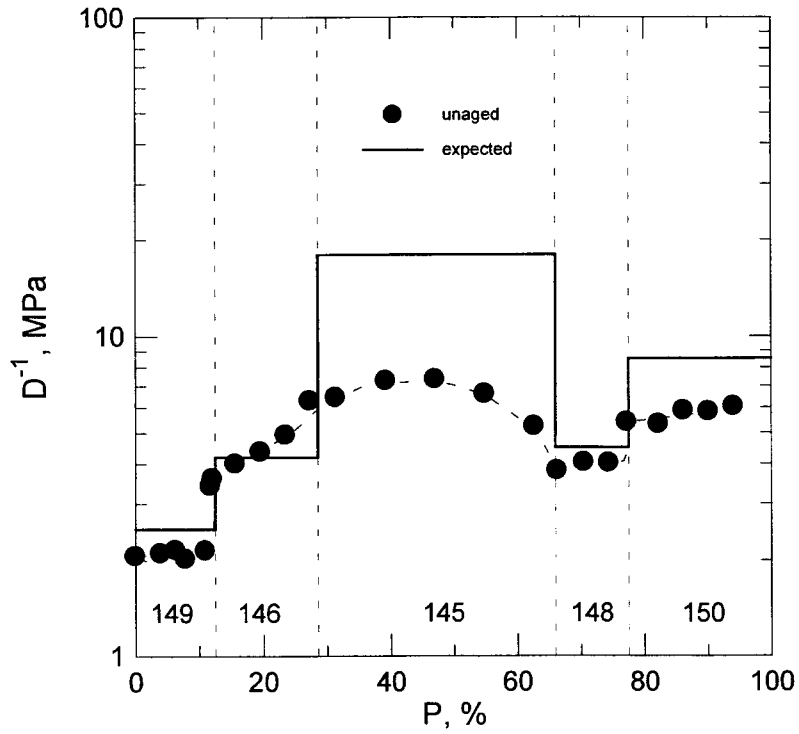


Figure 75. Modulus profiles for laminate material and expected results based on isolated material properties.

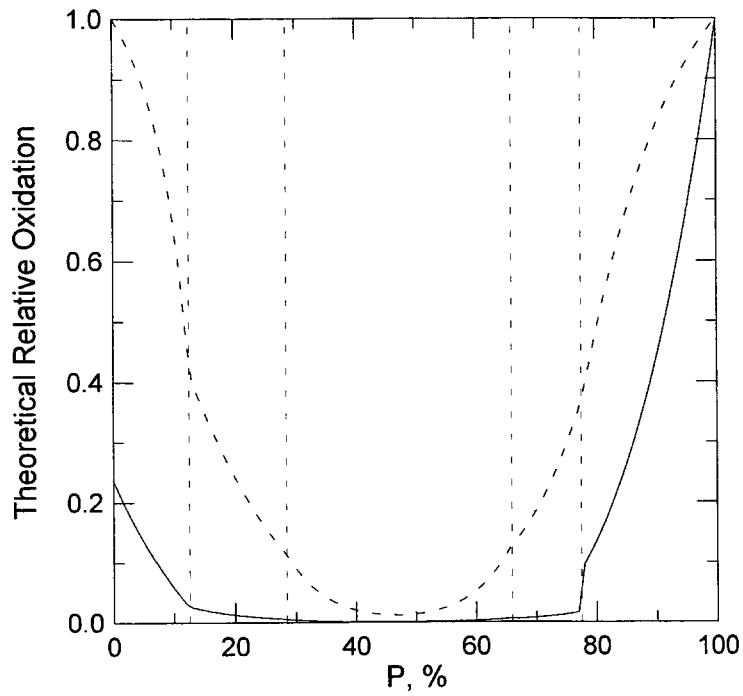


Figure 76. Modeling results for laminate using parameters from Table 9. Solid curve gives oxygen concentration profile whereas dashed curve gives oxidation profile.

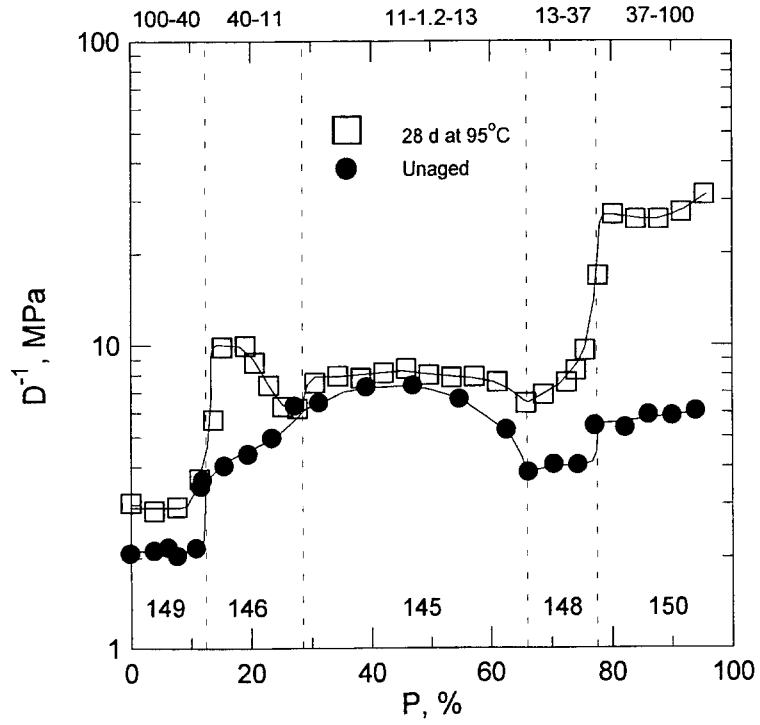


Figure 77. Experimental modulus profiles for aged and unaged laminates.

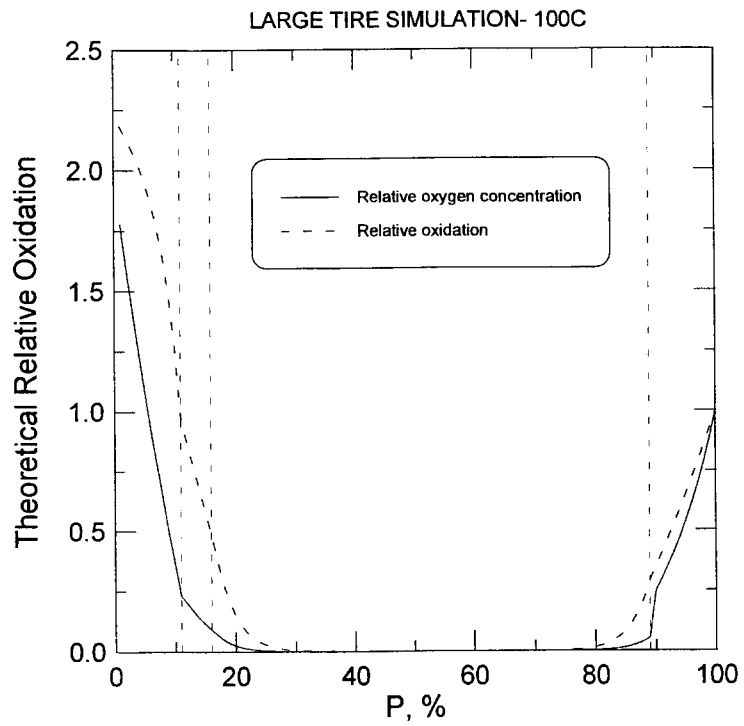


Figure 78. Large tire simulation at 100°C using the input parameters given in Table 10.

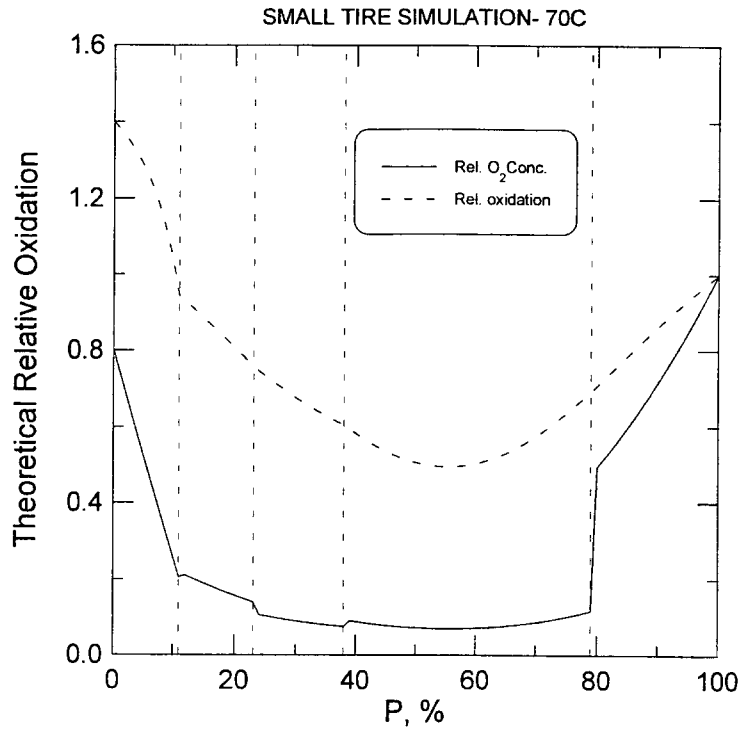


Figure 79. Small tire simulation at 70°C using the input parameters given in Table 11.

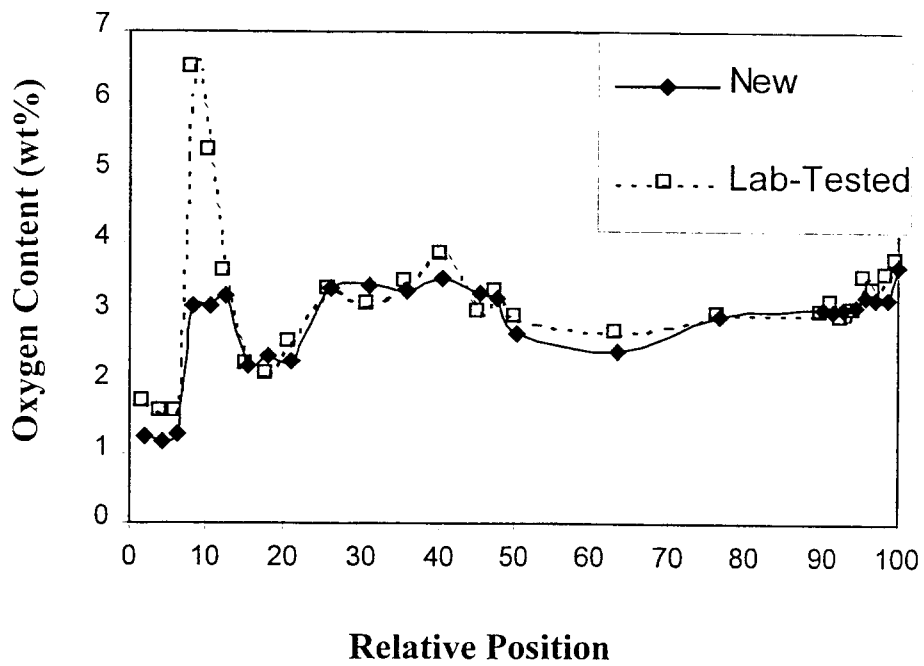


Figure 80. Oxygen content (wt. %) for lab-tested tire and new tire.

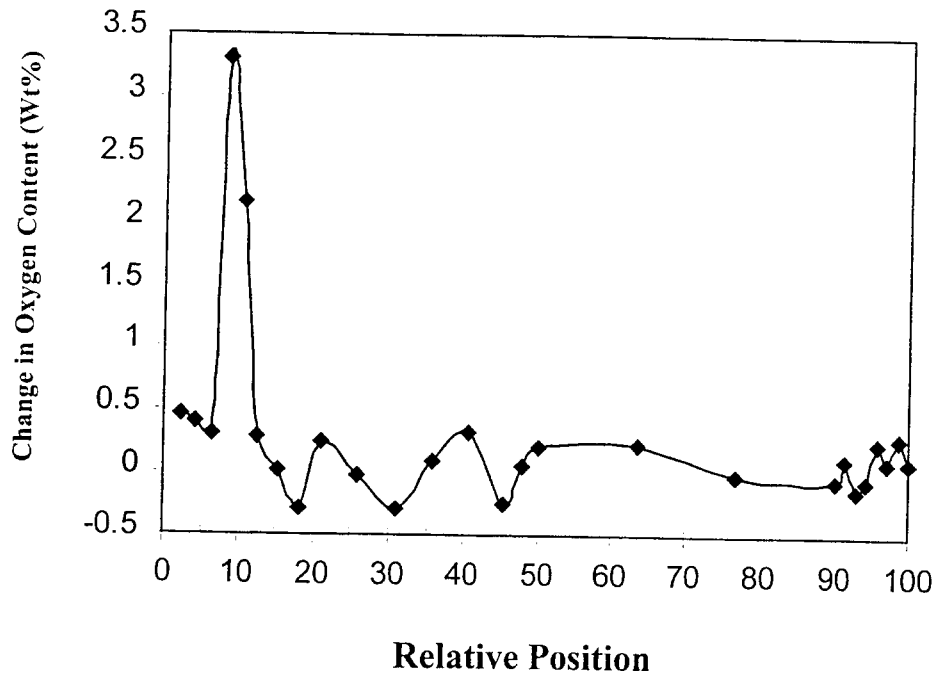


Figure 81. Change in oxygen content in lab-tested tire.

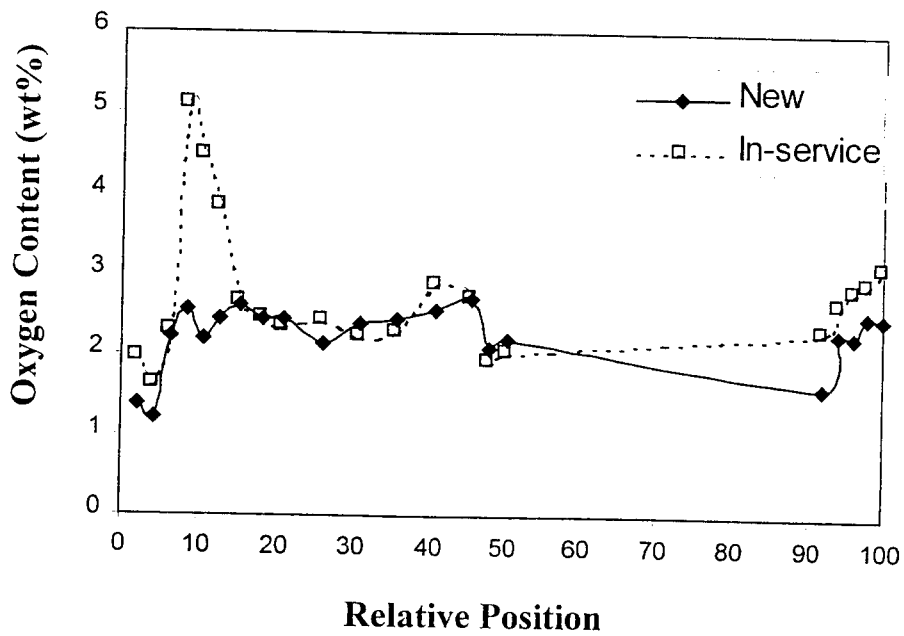


Figure 82. Oxygen content (wt. %) for in-service tire and new tire.

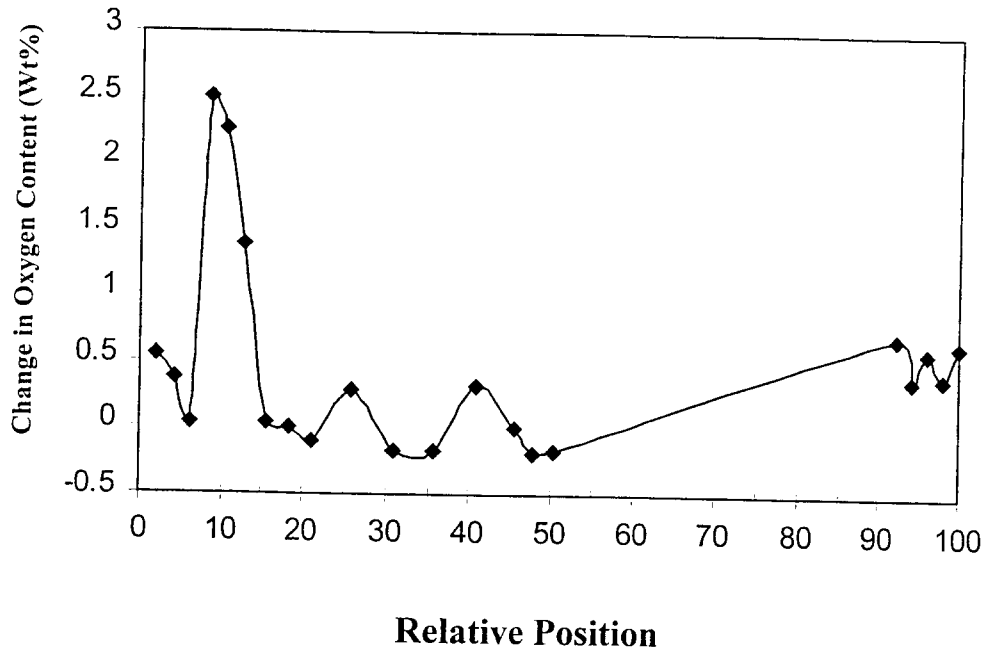


Figure 83. Change in oxygen content for in-service tire.

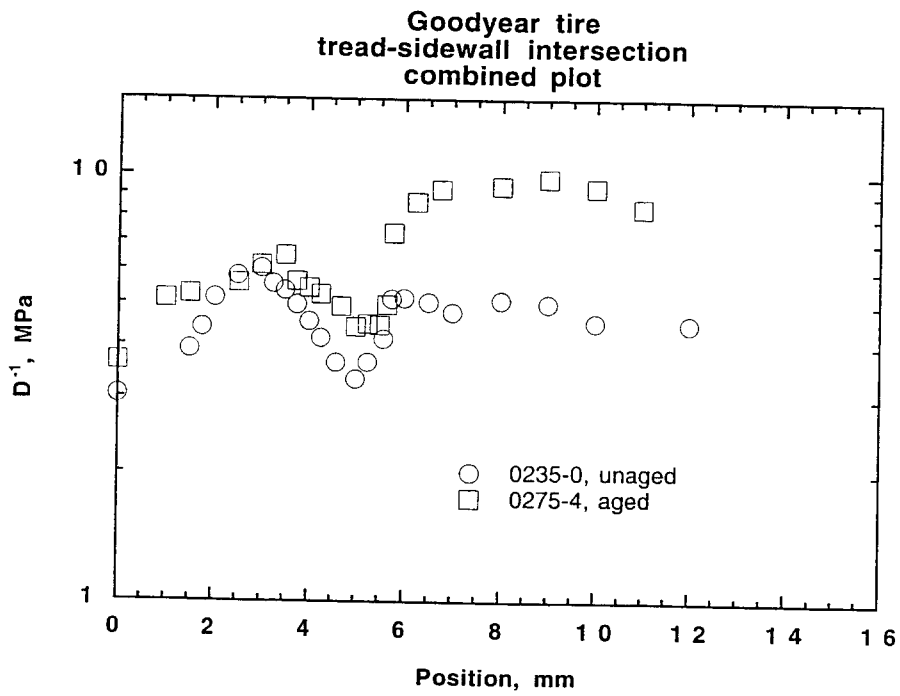


Figure 84. Modulus profile results for an unaged and an aged smaller tire.

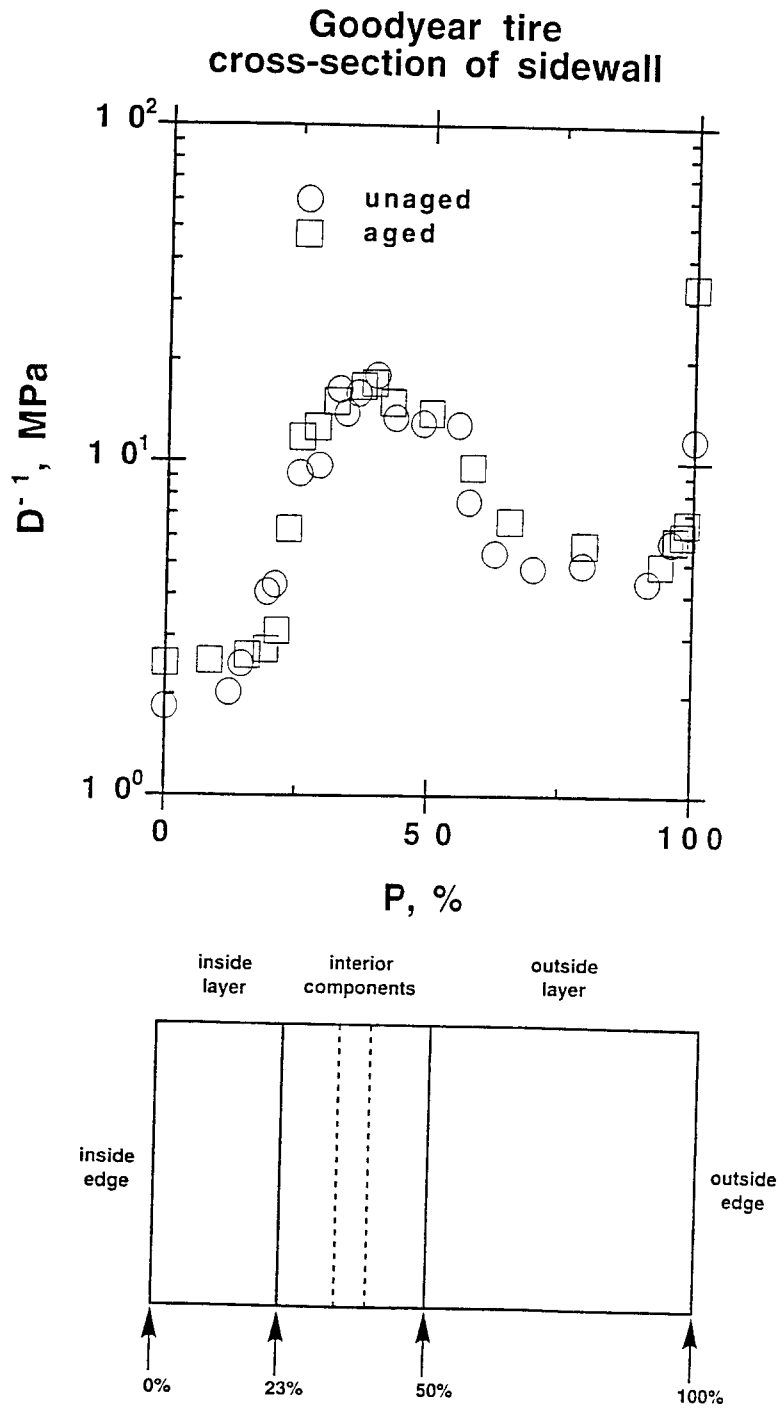


Figure 85. Modulus profile results for an unaged and an aged tire sidewall.

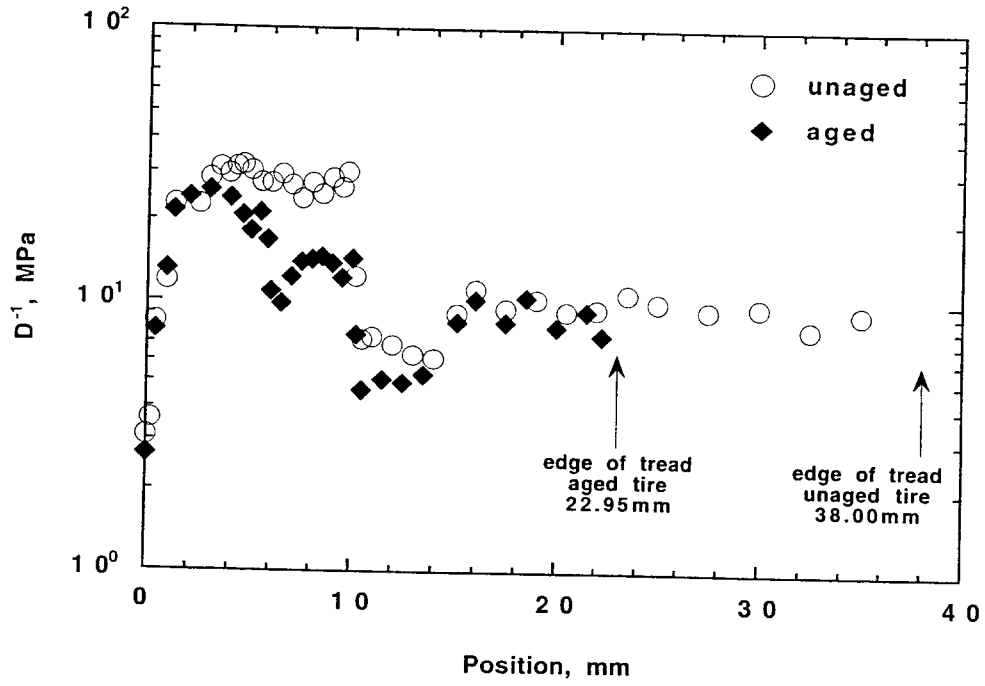


Figure 86. Unaged and aged modulus profile results for a larger size tire.

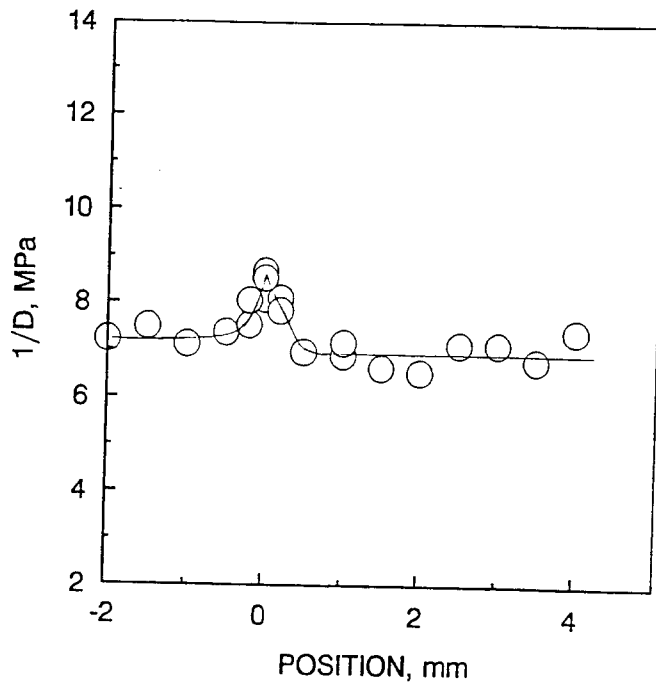


Figure 87. Modulus profile of two samples (134-2) with tread surfaces touching at 0 mm.

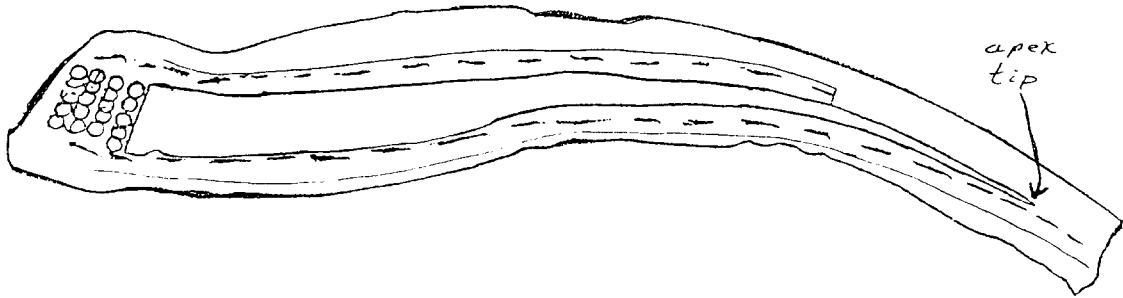


Figure 88. Sketch of the cross-section of the apex region of tire ER-1001.

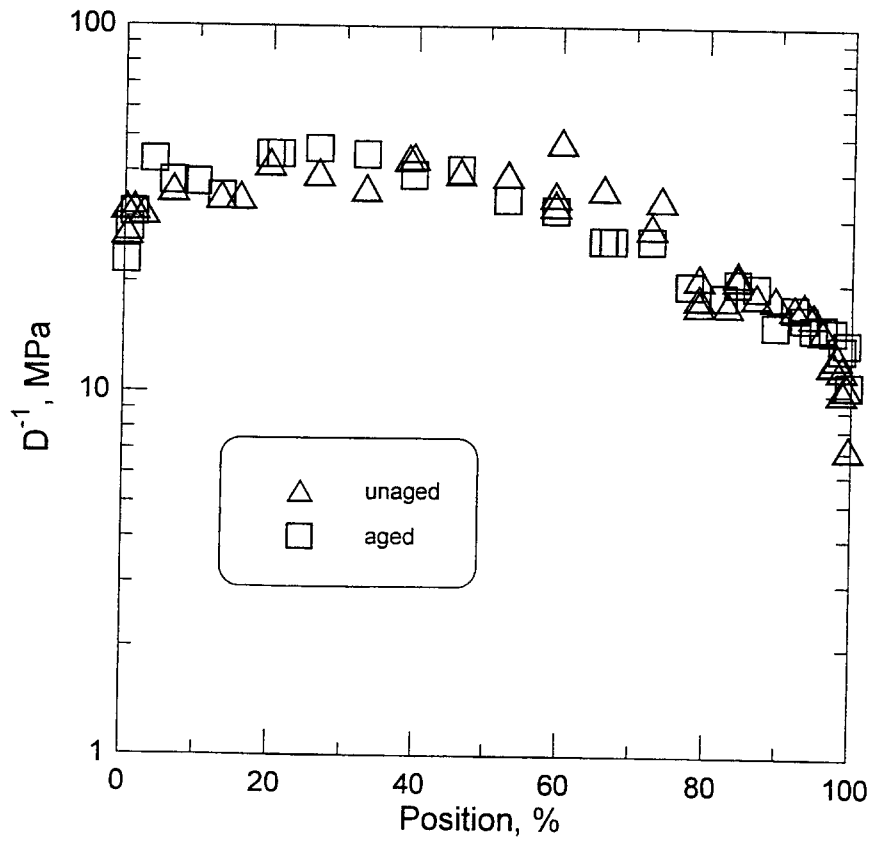


Figure 89. Modulus profiles of apex region of unaged and aged samples of ER-1001.

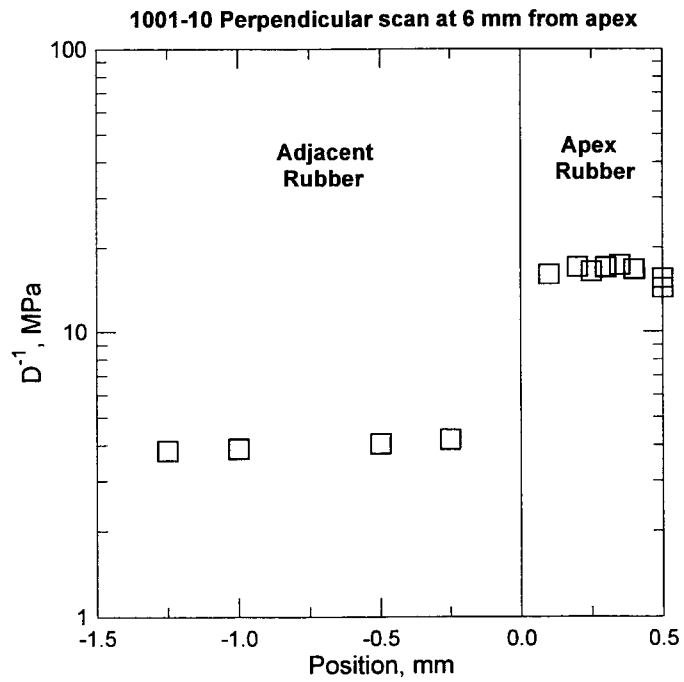


Figure 90. Modulus profile of aged ER-1001 perpendicular to the apex direction ~6 mm from the apex tip.

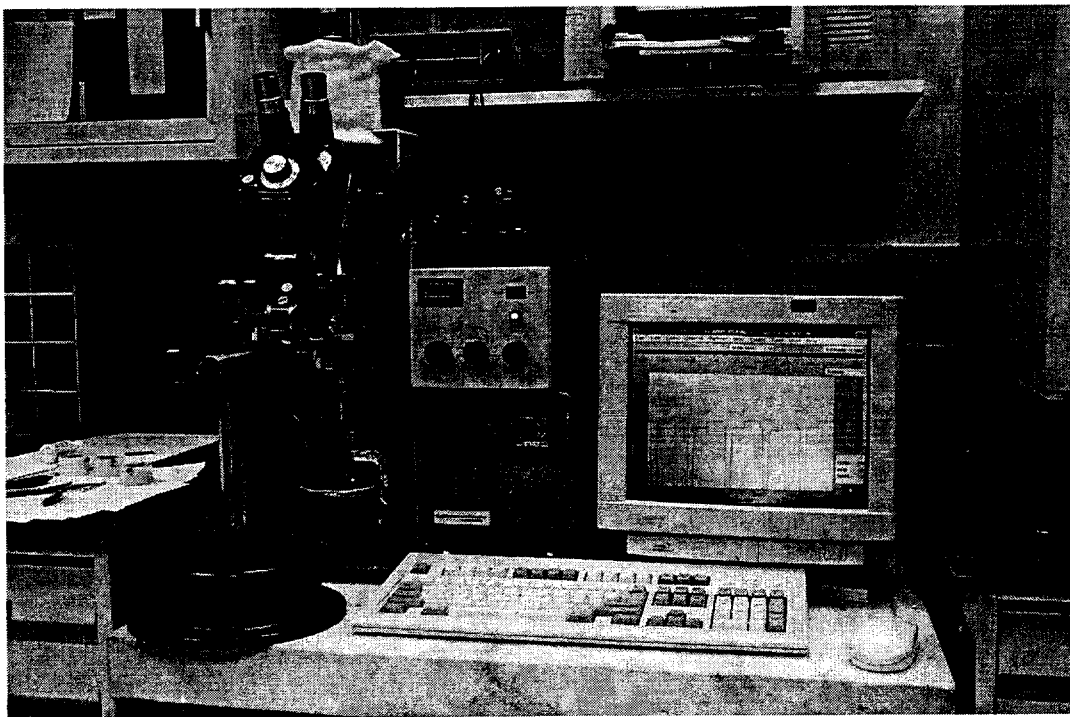


Figure 91. Automated modulus profiling apparatus.

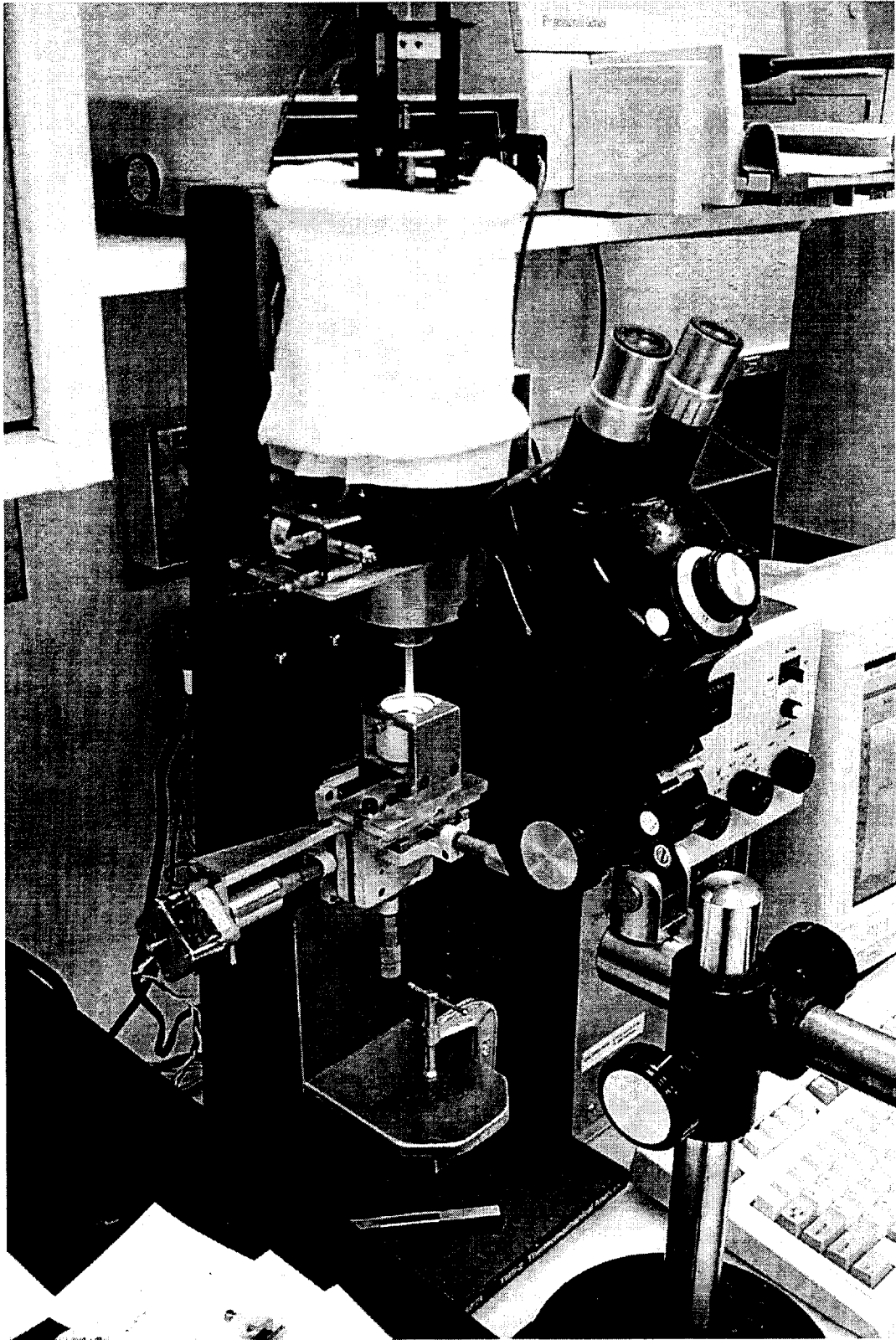


Figure 92. Sample area of modulus profiling apparatus.

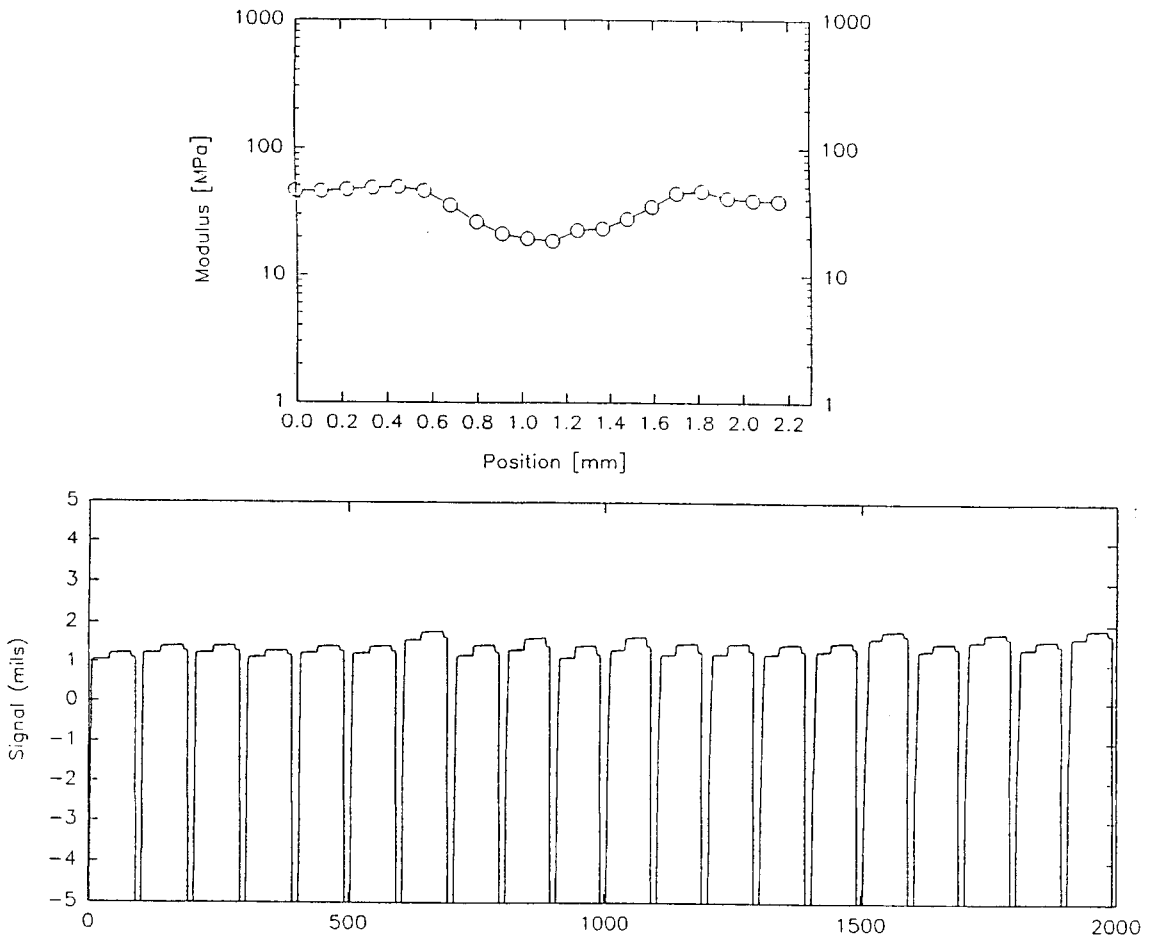


Figure 93. Typical computer output of the raw data (lower plot) and the analyzed modulus profile (upper plot).

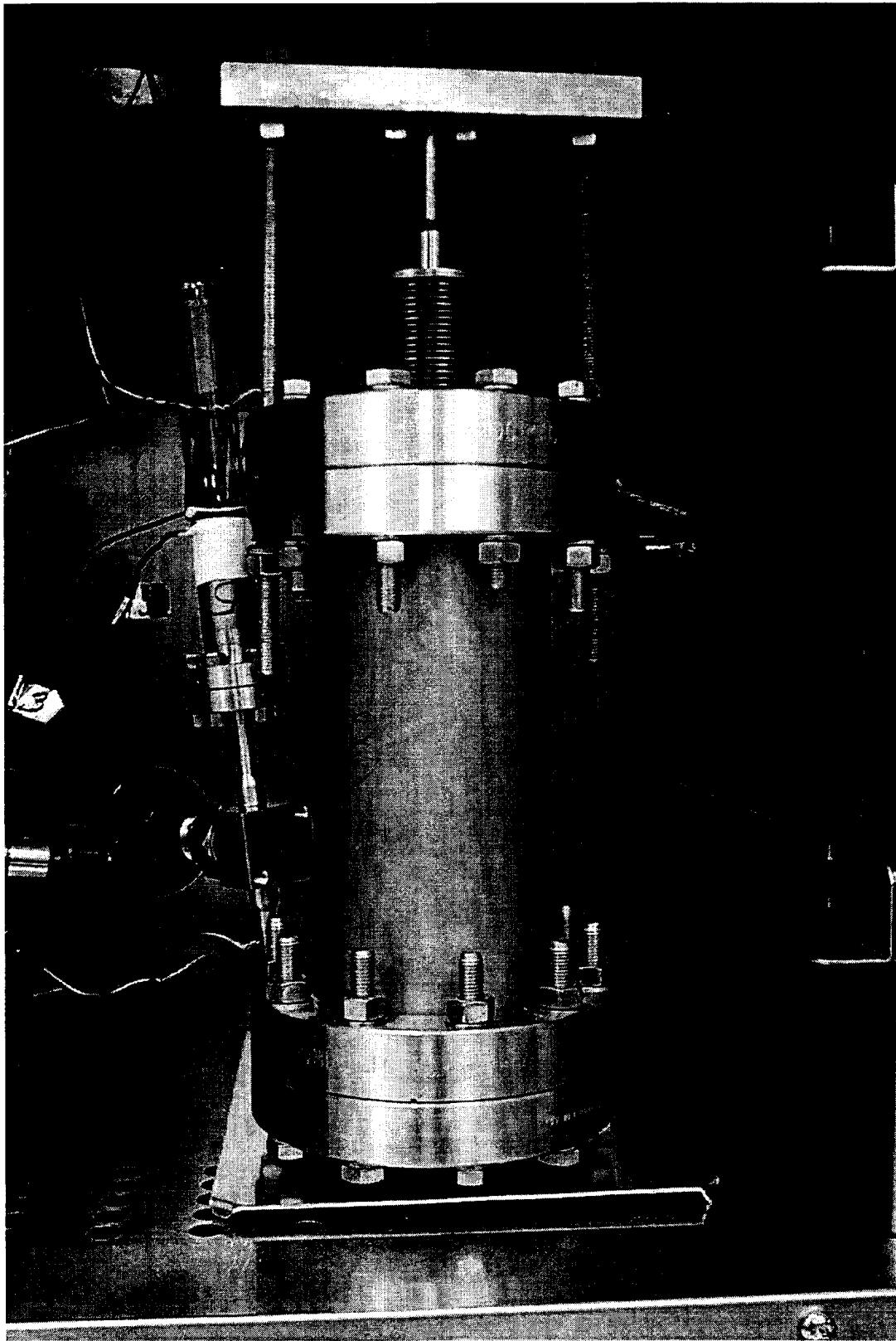


Figure 94. Dynamic oxygen consumption can with metal bellows arrangement for straining samples.

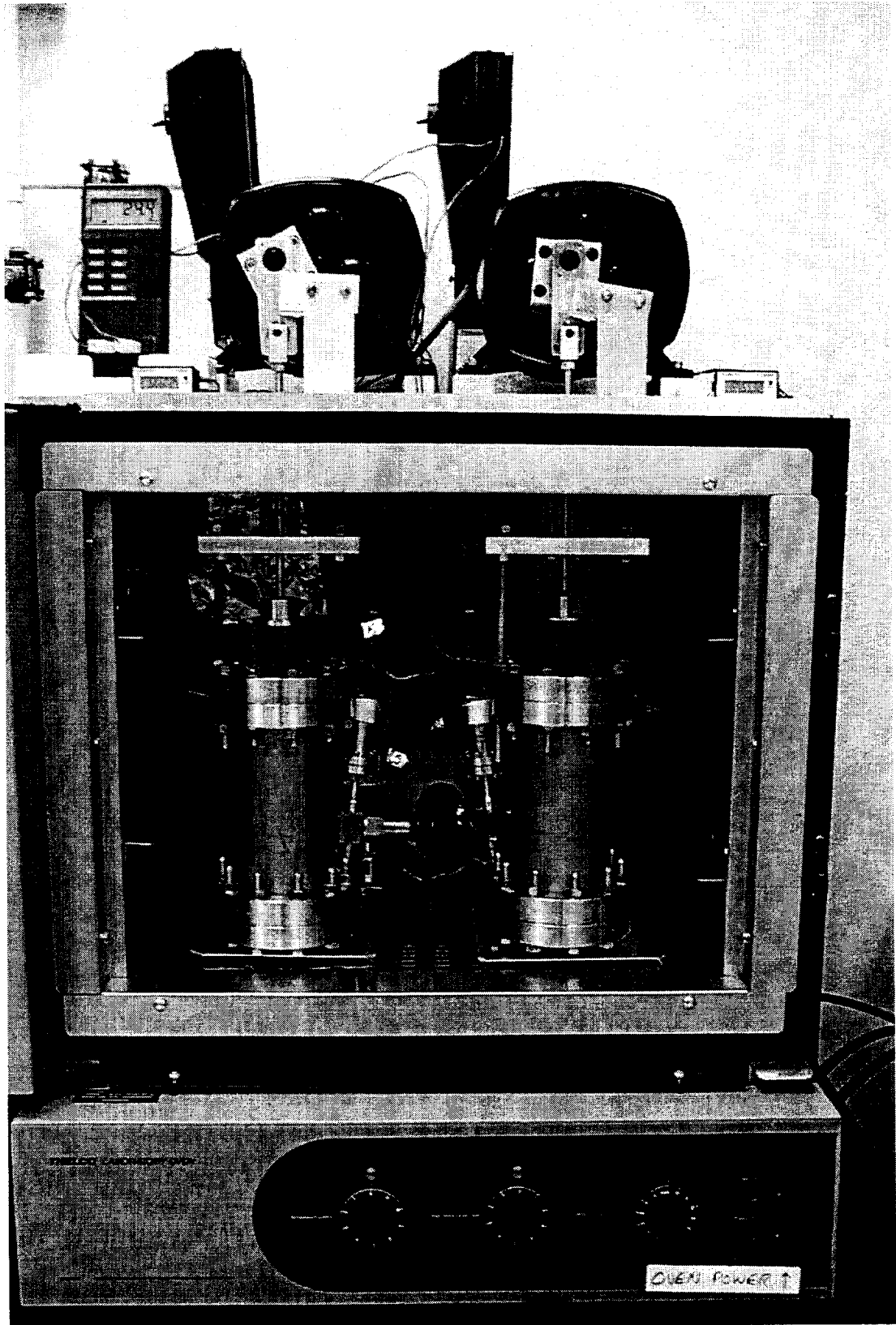


Figure 95. Dynamic oxygen consumption setup.

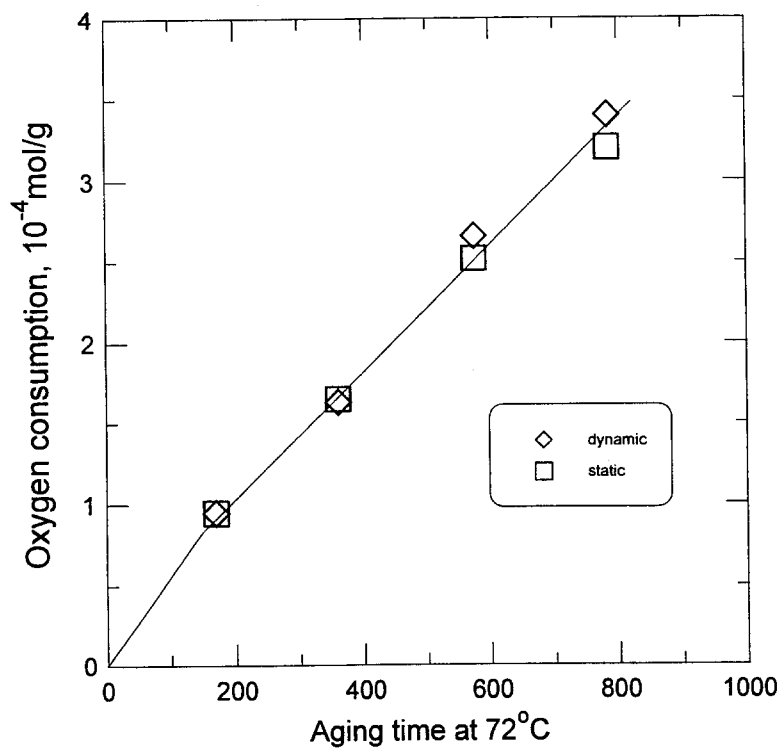


Figure 97. Integrated oxygen consumption results for Material 154 under static and dynamic aging conditions.

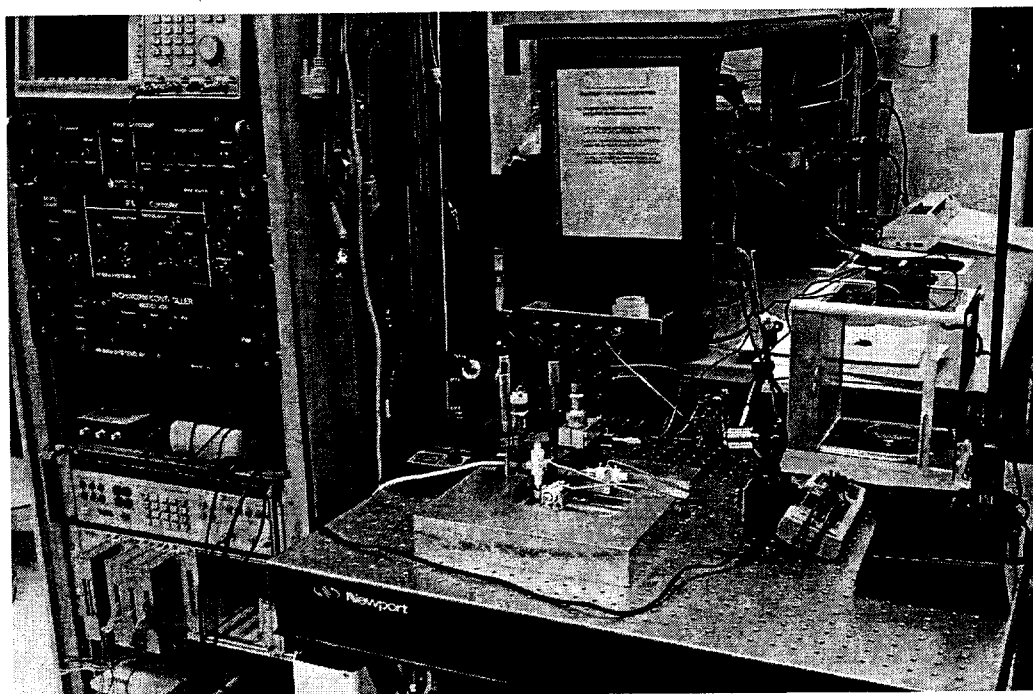


Figure 98. Interfacial Force Microscope (IFM) currently under construction.

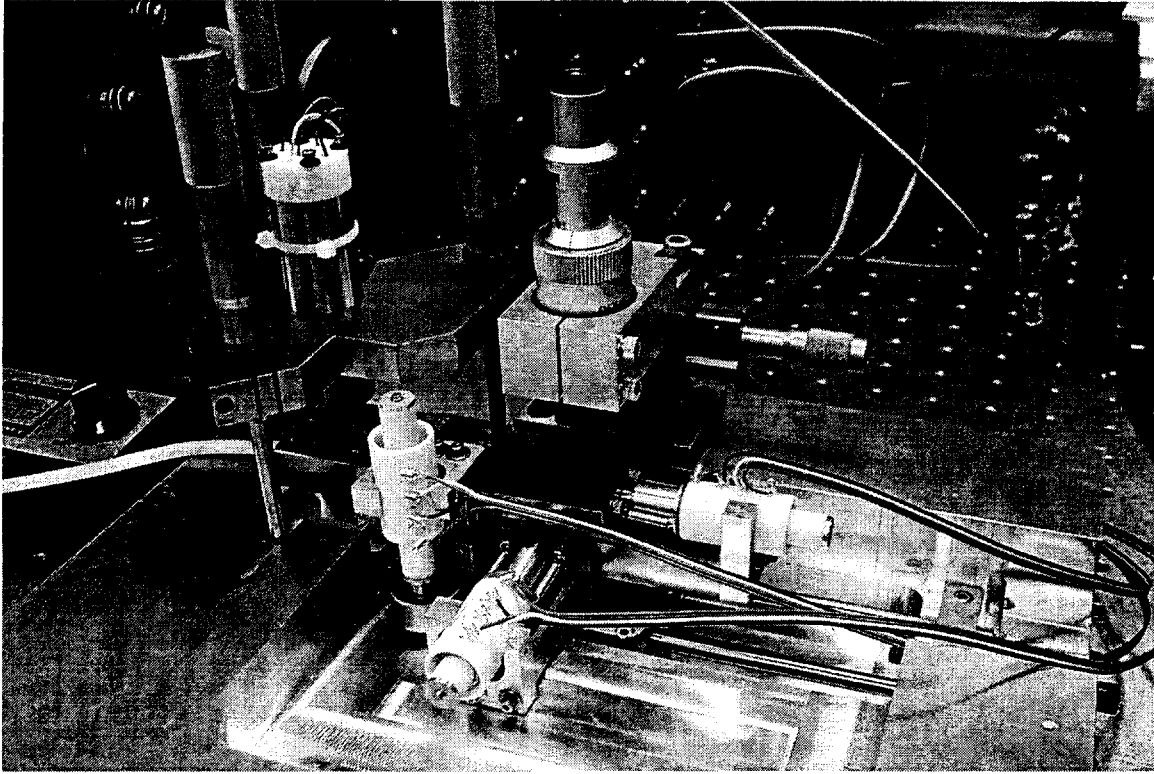


Figure 99. Detail of the IFM currently under construction.

APPENDIX 1

PROCEDURES FOR GC ANALYSIS OF GAS SAMPLES FOR MEASUREMENT OF OXYGEN CONSUMPTION RATES

J. Wise

December 7, 1995

1 Introduction

This document describes the procedures for our system of measuring oxygen consumption rates using gas chromatography. There are two primary parts to this document. Section 2 describes how to design and assemble a sample container; sections 3 to 6 give specific instructions for using the gas chromatograph to perform the analysis.

2 Sample Preparation

To prepare a sample for oxygen uptake measurements, it is necessary to consider what information is desired from the measurement, so that appropriate trade-offs between sample mass and time interval of the measurement can be made. For example, if the goal is to obtain a series of measurements to determine how the consumption rate changes with time, it may be preferable to use smaller sample masses and correspondingly longer time intervals. The advantage in this case is that fewer measurements would be required, allowing the overall set of measurements can be completed in less time (note that there can be significant amounts of idle time between oven aging segments). Conversely, if the goal is to obtain only one or two measurements rather than a series, it may be preferable to use more massive samples so that data can be obtained quickly. Obviously, it is necessary to consider the available sample mass when designing a set of experiments. When determining the time interval for which a sample is aged, I have adopted the standard of rounding to the nearest 24 hr increment. Because of uncertainty in the time required for sample containers to equilibrate at their aging temperature, I have set 72 hr as an arbitrary minimum aging time. For series of consumption measurements, 7 day or 14 day intervals are often convenient.

1. To establish the specific lengths of time and sample masses for specific aging tests, we use the relation

$$\frac{W}{V_f} = \frac{C_1}{\phi t}, \quad (1)$$

which is derived from the ideal gas law; W is the sample mass [g], V_f is the free (gas) volume of the container [cm^3], C_1 is a constant whose value is described below [mol/cm^3], ϕ is the (anticipated) oxygen consumption rate [$\text{mol}/\text{g}\cdot\text{s}$], and t is the aging time [s]. From the ideal gas law, the constant C_1 is given by

$$C_1 = \frac{\Delta p}{RT}, \quad (2)$$

where Δp is the change in gas pressure (measured at the aging temperature) in the container during aging, R is the gas constant, and T is the absolute temperature at which the aging occurs. From eqn. 2 it is clear that C_1 varies with temperature and also with the desired Δp . Values of C_1 such that the average pressure during aging will be ~ 130 Torr (or ~ 40 Torr, for measurements of β) for many common designs of aging tests are listed in Table 1.

Table 1: Design constants for backfilling containers.

Aging $T, ^\circ\text{C}$	$\Delta p = 60$ Torr (160 \rightarrow 100)		$\Delta p = 40$ Torr (150 \rightarrow 110)		$\Delta p = 20$ Torr (50 \rightarrow 30)	
	C_1	$p_{\text{backfill}}, \text{Torr}$	C_1	$p_{\text{backfill}}, \text{Torr}$	C_1	$p_{\text{backfill}}, \text{Torr}$
160	2.23×10^{-6}	109.4	1.48×10^{-6}	102.7	7.43×10^{-7}	34.2
140	2.33×10^{-6}	114.3	1.55×10^{-6}	107.1	7.79×10^{-7}	35.8
125	2.42×10^{-6}	119.4	1.61×10^{-6}	111.9	8.08×10^{-7}	37.2
110	2.51×10^{-6}	123.1	1.67×10^{-6}	115.4	8.40×10^{-7}	38.6
96	2.61×10^{-6}	128.0	1.74×10^{-6}	120.0	8.72×10^{-7}	40.1
80	2.73×10^{-6}	134.4	1.82×10^{-6}	126.1	9.11×10^{-7}	41.9
65	2.85×10^{-6}	140.3	1.90×10^{-6}	131.6	9.52×10^{-7}	43.8
52	2.95×10^{-6}	145.5	1.97×10^{-6}	136.4	9.90×10^{-7}	45.5
40	3.07×10^{-6}	150.9	2.05×10^{-6}	141.5	1.03×10^{-6}	47.3
23	3.26×10^{-6}	160.0	2.17×10^{-6}	150.0	1.09×10^{-6}	50.0

2. After the appropriate sample mass is determined, the sample must be cut so that it will fit into the sample container. Additionally, the sample must be cut sufficiently thin to avoid diffusion-limited oxidation (DLO) effects. We calculate L_c , the critical thickness to preclude DLO effects as

$$L_c = \left(\frac{2pP_{\text{ox}}}{\phi} \right)^{0.5}, \quad (3)$$

where p is the average oxygen partial pressure surrounding the sample, P_{ox} is the oxygen permeability coefficient, and ϕ is the oxygen consumption rate.

Because setting up new containers or modifying the contents of existing containers is a time-consuming process, it is prudent to initially cut the samples so that they will be suitable

for the broadest possible range of consumption rate measurements that may be anticipated. This means that calculation of L_c should be done assuming that the sample will be used to measure β ; i.e., that the average pressure will be 40 Torr rather than the normal 130 Torr (Albuquerque ambient). This means evaluating eqn. 3 using $p = 30$ Torr (the ending pressure). Samples can easily be cut to ~ 1 mm thickness and, with little extra effort, to $\sim 1/2$ mm thickness. Samples can be cut as thin as $1/3$ mm, but because this requires special care and effort, the masses of samples of this thickness should be minimized.

3. The sample is placed in its container, and the mini Conflat flange joint between the container and the valve is sealed with a silver-plated copper gasket. To preclude leaks, this flange must be very tight. (I have not measured the torque required on the bolts, but I frequently shear off the bolts when tightening these flanges.) After sealing, the containers are pumped on the vacuum manifold, typically for 24 hr. They are then removed from the manifold and left, under vacuum, for typically 24 hr before being backfilled with O_2 . At the time of the first backfill, the pressure inside the container is measured to determine whether the container leaks. In general, I assume that the container does not leak if its pressure after 24 hr is less than 1 Torr. This guideline is only approximate, however; if the sample container has a high fill factor, higher pressures may result from outgassing rather than being indicative of leaks. If the container does not leak, it is backfilled to the desired oxygen pressure. Design constants for backfilling are listed in Table 1.
4. To ensure that the sample contains dissolved oxygen in equilibrium with the gas in the container, the samples are allowed to equilibrate for time t given by

$$t \geq \frac{2L^2}{D} , \quad (4)$$

where L is the sample thickness and D is the oxygen diffusivity within the sample. Note that this equilibration occurs at room temperature, and the appropriate (room temperature) value of D must therefore be used in eqn. 4. Equilibration typically takes 7 days; the sample containers are typically evacuated and backfilled two or three times during this period.

5. A critical parameter used to calculate oxygen consumption rates is the ratio $V_f/(V_f + V_m)$ where V_f is the free volume of the flask and V_m is the volume of the manifold. That is,

$$r = \frac{P_2}{P_f} = \frac{V_f}{V_f + V_m} . \quad (5)$$

This ratio is important because it relates measured properties (pressure, partial pressures) of the gas *after expansion into the manifold* to those properties of the gas *while confined to the container*. It is, obviously, possible to calculate r from V_f and V_m (~ 11.5 cm³). However, I always measure r . This is easily accomplished by attaching the container to the

manifold, backfilling to a known (measured) pressure, sealing the container by closing its valve, evacuating the manifold, then opening the container valve and measuring the resulting pressure. I normally measure this ratio approximately six times before aging the container.

3 GC Setup

1. Load GC method 3 (on the GC keypad, type: SHIFT, LOAD, 3, ENTER), which contains the parameters (Table 2) for analyzing gas samples. Settings listed in the right-hand column Table 2 are irrelevant to the gas analysis procedure, but should be maintained for instrumental stability.

Table 2: Settings of GC control parameters. Settings listed in the right-hand column are irrelevant to the gas analysis procedure but should be maintained for instrumental stability.

Parameter	Value	Parameter	Value
OVEN TEMP	70	RATE	0.0
INIT VALUE	70	FINAL VALUE	70
INIT TIME	8.75	FINAL TIME	8.00
DET A TEMP	150	DET B TEMP	300
SIG 1	A	INJ A TEMP	175
		INJ B TEMP	none
		EQUIB TIME	1?

2. Verify that the settings are as shown in Table 2. Adjust settings as necessary to match those listed in Table 2.
3. Verify that the TCD detector reference gas is flowing (2nd valve from top at left on GC front panel).
4. Verify that the TCD detector is ON (DET, A, ON).
5. Verify the proper valve timing in the table.
6. Verify that the helium carrier gas is on and that gas is flowing (the flowrate at the TCD output can be measured with the gas flow meter). The carrier gas must always be left on. Check that bottle valve is open, that bottle pressure is sufficient > 200 psi, and that regulator output pressure is ~80 psi.

7. Verify that the control gas to actuate the valves is on. (This gas is normally on.) Check that bottle valve is open and regulator output pressure is ~ 65 psi.
8. (Optional: only necessary if planning to backfill containers with oxygen.) Turn on oxygen backfill gas. Open bottle valve and verify that regulator output pressure is ~ 10 psi.)
9. (Optional: only necessary if planning to obtain GC calibration curve.) Turn on calibration gas. Open bottle valve and verify that regulator output pressure is ~ 14 psi.)
10. Delete any existing **integrator** time program (On the integrator keypad, type: DEL, TIME, ENTER). Verify that the time program has been deleted by printing the current time program (LIST, TIME, ENTER).
11. Desirable, although optional, settings for the integrator are: attenuation = 2^0 (ATT 2 \uparrow , 0, ENTER), threshold = 0 (THRSH, 0, ENTER), and chart speed = 1 (CHT SP, 1, ENTER). The parameters attenuation and threshold affect only the appearance of the printed output; they do not affect the integration calculations. Chart speed is set to its minimum value to conserve paper. To print all current integrator parameters, type LIST, LIST on the integrator keypad.
12. Turn on the vacuum pump. The switch is on the pump, which is on the floor under the bench.
13. Turn on the pressure gauge. The switch is on the digital pressure meter, which is on the bench, in the monkey bars.
14. Open valves V_B and V_C , to evacuate the manifold.
15. Open the calibration gas valve (V_D) to purge the calibration gas supply line. Close the calibration gas valve V_D .
16. Open the oxygen valve (V_E) to purge the oxygen supply line. Close the oxygen valve V_E .

4 Calibration.

The GC must be calibrated using the external standard gas mixture. The composition of this gas is given in Table 3. As a practical matter, it is best to begin the calibration procedure with one or two analyses of pure O_2 at pressures of ~ 100 Torr; this seems to help stabilize the detector. Typically 10–15 calibration points with the standard gas are required for the detector to stabilize. I recommend beginning the calibration at ~ 1200 Torr of calibration gas and taking points at intervals of ~ 200 Torr as the pressure is reduced and then at intervals of ~ 200 Torr as the pressure is increased. That is, taking points at 1200, 1000, 800... 200, 100, 300... 900, 1100. The first four or five points will typically fall below the calibration that is established by the remaining

Table 3: Composition of calibration gas. Matheson bottle code GW5831.

Component	Nominal %	Analyzed %
O ₂	10.0	10.01 ± 0.02
N ₂	2.0	1.99 ± 0.02
CO ₂	2.0	1.99 ± 0.02
CO	0.5	0.499 ± 0.005
CH ₄	0.3	0.301 ± 0.003
C ₂ H ₆	0.2	0.200 ± 0.002
He	Bal	Bal

points. The O₂ calibration is typically the most variable; the CO and CO₂ calibrations are usually much more stable. Calibrations of CH₄ and C₂H₆ can vary considerably, but this is of little concern because neither of these gases appear to be produced in thermal aging. It is good practice to obtain additional calibration points between analyses of samples to determine whether the calibration has changed, as is often the case. Long-term drift can be monitored by observing the oxygen/nitrogen ratio.

The calibration curve is produced in the form

$$\text{TCDcounts} = mp + b,$$

where p is the gas partial pressure in Torr. For all gas components, the calibration can be treated as linear over the range 0–1200 Torr total calibration gas pressure. The calibration line is established with a least-squares regression and qualified by the fit parameter r^2 . The fit parameter, r^2 , is typically > 0.98 . If $r^2 < 0.98$, the calibration should be considered to be suspect.

Each calibration point is obtained in a manner similar to that described in section 5, making the obvious substitution of V_D (calibration gas) for V_{Flask} (sample gas container).

5 Analysis

1. Attach container to be analyzed to the manifold using one of the two the Cajon Ultra-Torr fittings.
2. Open V_{A_1} (or V_{A_2} , as the case may be), to connect the manifold to the (sealed) container.
3. Open V_B if it is closed; it should already be open.
4. Open V_C , to evacuate manifold.

5. Verify that the pressure gauge reads 0.00 Torr. Zero the pressure reading if necessary using the fine adjustment.
6. Close V_C , to disconnect the vacuum pump from the manifold. The pressure gauge should continue to read nearly zero.
7. Verify that V_B is open.
8. Open V_{Flask} , to allow gas from the container to expand into the manifold and sample loop. I refer to this expansion, when the manifold is evacuated, as a “Full expansion” (i.e., an expansion into the *full* volume of the manifold).
9. Press the GC “start” button to start the first GC analysis run.
10. Close V_{Flask} , to isolate the container. This is a safety precaution that preserves the integrity of the gas composition inside the container.
11. Close V_B , to isolate the manifold.
12. Record relevant parameters into a table in a log book as shown in Table 4. Be sure to record room temperature (there is a thermocouple with meter on the bench).
13. At the end of the first GC run, the pressure in the manifold will increase as the high-pressure helium carrier gas from the sample loop expands into the manifold.
14. Verify that V_B is closed.
15. Open V_C , to evacuate the GC sample loop. I typically keep V_C open for 20 sec.
16. Close V_C .
17. Open V_B , to allow sample gas to expand into the sample loop.
18. Open V_{Flask} to allow more of the sample gas to expand from the container into the sample loop. I refer to this expansion, when the manifold contains some sample gas at the pressure of the first expansion, as a “Partial expansion” (i.e., an expansion into the *partial* volume of the manifold).
19. Press the GC “start” button to start the second GC analysis run.
20. Close V_{Flask} , to isolate the container.
21. Close V_B , to isolate the manifold.
22. Record relevant parameters in a log book, as shown in Table 4.

Table 4: Information normally recorded into log book. (These data copied from log book 6, page 65.)

FLASK	P_{expanded}	RUN#	Date/Time	EXPANSION	COMMENTS
93	41.1	1061	1-11-95 14:35:51	FULL	
93	35.8	1062	1-11-95 14:44:24	PARTIAL	expand \rightarrow 20.3 ratio = 0.567
94	42.5	1063	1-11-95 14:55:28	FULL	
94	37.5	1064	1-11-95 15:03:53	PARTIAL	expand \rightarrow 21.4 ratio = 0.571

RUN#	PRESSURE	CO ₂	C ₂ H ₆	O ₂	N ₂	CH ₄	CO	COMMENTS
1061	41.1	17161	—	228765	19763	—	4791	O ₂ low?
1062	35.8	14932	—	357148	23008	—	5490	
1063	42.5	15520	—	496006	22493	—	6493	
1064	37.5	8603	—	296930	13951	—	3799	CO ₂ low?

Flush & backfill with O₂.

FLASK	P_{backfill}	P_{expand}	ratio	P_{backfill}	P_{expand}	ratio	P_{backfill}	TIME
93	142.4	79.5	0.558	145.2	81.1	0.558	160.6	14:00
94	161.8	91.0	0.562	158.2	88.8	0.561	160.1	14:19

23. After both analyses, the container is evacuated and backfilled with O₂ as shown in Table 4.
24. The container is then left to equilibrate before being aged again.

I have chosen to do two analyses of each container, as described above. I believe this is prudent because of the occasional bad separation. My standard analysis procedure is to use one full and one partial expansion; this was derived from an attempt to conserve sample gas between runs when the sample was particularly valuable (i.e., the container volume was small or the container had been aged for an especially long time). When, as happens occasionally due to operator error, the sample gas stored in the manifold is contaminated or lost, it is possible to perform the analysis as two full expansions.

6 GC Shutdown

1. Load GC method 1 (SHIFT, LOAD, 1, ENTER), to put the GC into its standby mode.
2. Verify that valves V_D (calibration gas) and V_E (oxygen) are closed, to isolate the manifold from the calibration gas and oxygen supplies.
3. Verify that valves V_{A1} and V_{A2} (at Cajons Ultratorr ports) are closed.
4. Verify that V_B is open.
5. Remove all sample containers from the manifold.
6. Open V_C, to evacuate the manifold.
7. Close V_C.
8. Turn off the vacuum pump.
9. Open the bleeder valve, to bleed the line between the manifold and the vacuum pump.
10. Close the bleeder valve.
11. Turn off the pressure gauge.
12. Close the valve on the calibration gas bottle.
13. Close the valve on the oxygen bottle.

7 Miscellany

1. When reading pressures on the digital pressure meter, the observed reading must be multiplied by 10 to give the pressure in Torr. This is true regardless of whether the pressure meter is set to the high or low range.
2. When I refer to a valve as being “open,” the only critical valves are V_{A_2} , V_B , and V_{Flask} . I define the first two of these valves as open when the handle has been turned just to the point when the internal spring no longer exerts pressure on the handle. I define V_{Flask} as open when cracked open plus approximately 1/4 turn.

APPENDIX 2

```
program lamx2

c * * * * *
c * A program to calculate oxygen concentration *
c * profiles in laminates of up to 20 layers, each *
c * layer having different oxygen consumption rate, *
c * diffusivity, and solubility. Calculations assume *
c * BAS kinetics and Fickian diffusion, solved *
c * numerically as per Cunliffe and Davis (Polym. Deg.*
c * Stab., v4 (1982) p17.). Constant flux is assumed *
c * across layer boundaries. Relative oxidation in *
c * each inner layer is calculated as if that specific*
c * layer were at the surface. *
c * * * * *

c      local variables
c      integer*2 i,test1
c      character*12 fname

c      common block variables
c      real*8 sol0,beta0,dens0,perm0,phi0
c      dimension sol0(1:20),beta0(1:20),dens0(1:20)
c      dimension perm0(1:20),phi0(1:20),thick0(1:20)

c      real*8 p_ref,p_in,p_out,tot1
c      integer*4 nl,thick0

c      common /params/ sol0,beta0,dens0,perm0,phi0,thick0,
1      p_ref,p_in,p_out,tot1,nl

c      get input data (lines 100-300)

100  continue
c      write (6,*)
c      * ('Enter number of layers in the laminate
c      * (max = 20):')
c      read (5,*,err=100) nl
c      if ((nl .le. 0) .or. (nl .gt. 20)) goto 100
110  continue
c      write (6,*) ('Enter inside (cavity) oxygen pressure
c      * (cmHg):')
c      read (5,*,err=110) p_in
c      if (p_in .lt. 0.) goto 110
120  continue
c      write (6,*) ('Enter outside oxygen pressure
c      * (cmHg):')
c      read (5,*,err=120) p_out
c      if (p_out .lt. 0) goto 120
130  continue
```

```

c   for our data in Albuquerque, use p_ref = 13.2
   write (6,*) ('Enter reference oxygen pressure
* (cmHg):')
   read (5,*) p_ref
   if (p_ref .lt. 0) goto 130
140  continue
   write (6,*) ('Enter total laminate thickness
* (cm):')
   read (5,*,err=140) totl
   if (totl .le. 0) goto 140
150  continue
   write (6,*)
* ('Enter filename in which to save calculated
* profile:')
   read (5,'(a12)',err=150) fname
11   format ('Enter thickness [total = 1000] of layer
* ',i2,':')
21   format (' Enter O2 consumption rate (mol/g-s) of
* layer ',i2,':')
31   format (' Enter O2 permeability (ccSTP/cm-s-cmHg)
* of layer ',i2,':')
41   format (' Enter solubility (ccSTP/cm3-cmHg) of
* layer ',i2,':')
51   format (' Enter density (g/cm3) of layer ',i2,':')
61   format (' Enter beta of layer ',i2,':')

   test1 = 0
   do 300, i = 1,nl
211  write(6,11) i
      read(5,*,err=211) thick0(i)
221  write(6,21) i
      read(5,*,err=221) phi0(i)
231  write(6,31) i
      read(5,*,err=231) perm0(i)
241  write(6,41) i
      read(5,*,err=241) sol0(i)
251  write(6,51) i
      read(5,*,err=251) dens0(i)
261  write(6,61) i
      read(5,*,err=261) beta0(i)
      test1 = test1 + thick0(i)
300  continue

c   test that fractional thickness sum to unity
400  continue
   IF (test1 .ne. 1000.) THEN
      test1 = 0
      write (6,*)
*   ('Layer thicknesses did not sum to 1000')
      do 450, i = 1,nl
         write(6,11) i
         read(5,*) thick0(i)

```

```

        test1 = test1 + thick0(i)
450      continue
        if (test1 .ne. 1000.) goto 400
ENDIF

c      call subroutine to calculate oxidation profiles
call calc1(fname)

return
end

c      *****

subroutine calc1(fname)

c      constant flux across layer boundaries; assume no
c      reaction in intervals i+1 and i-1 adjacent to
c      boundary--this introduces only insignificant error.
c      Flux calculation with solubility change across
c      layers:
c       $D(i+1) * (\theta(j-1) - S(i+1)/S(i)*\theta(j))$ 
c       $= D(i) * (\theta(j) - \theta(j-1))$ 

integer*4 i,j,k,n,start,stop
real*8 iter2,p2,th0,c_in,c_out
real*8 theta,rel
character*12 fname

dimension theta(0:1000),rel(0:1000)

real*8 sol0,beta0,dens0,perm0,phi0
real*8 p_ref,p_in,p_out,totl,maxtheta
real*8 phi_i,alpha_i,beta_i
integer*4 nl,thick0

dimension sol0(1:20),beta0(1:20),dens0(1:20)
dimension perm0(1:20),phi0(1:20),thick0(1:20)

common /params/ sol0,beta0,dens0,perm0,phi0,thick0,
*           p_ref,p_in,p_out,totl,nl

c      number of intervals
k = 1000.

c_in = p_in*sol0(1)
c_out = p_out*sol0(nl)

c      boundary conditions
theta(k) = 1.
th0 = c_in/c_out

c      prepare initial iteration: guess theta(k-1)

```

```

maxtheta = max(th0,theta(k))
theta(k-1) = maxtheta
p2 = 1.
iter2 = maxtheta

c   calculate theta(k-2) ... theta(0)
c   i refers to a specific layer within the composite
write(6,*) 'Working...'
600 continue
start = k-1
stop = k-thick0(nl)+1
do 620, i = nl,1,-1
c   correct beta, phi for p_out .ne. p_ref
beta_i = beta0(i)*p_out/p_ref
phi_i = phi0(i)*(1+beta0(i))/((p_ref/p_out) +
*   beta0(i))
alpha_i =
* (22400*phi_i*totl*totl*dens0(i))/(p_out*perm0(i))
alpha_i = alpha_i*(beta_i+1)

do 610, j = start,stop,-1
theta(j-1) =
* (alpha_i*theta(j)/(((beta_i*theta(j))+1)*k*k))
* + (2*theta(j)) - theta(j+1)
if (j .eq. 1) goto 700
IF (theta(j-1) .lt. 0) THEN
c   theta(j) < 0 is physically meaningless.
c   To prevent math errors, terminate this
c   iteration and proceed to next iteration.
c   We set theta(0) = theta(j-1) < 0 to indicate
c   that the current trial value of theta(k-1) is
c   too small.
theta(0) = theta(j-1)
goto 710
ENDIF
610 continue
rel(stop-1) = rel(stop)
if (i .eq. 1) goto 620
j = stop - 1
theta(j-1) = (sol0(i-1)/sol0(i))*theta(j)
* + (perm0(i)*sol0(i-1))/(perm0(i-1)*sol0(i))*
* (theta(j)-theta(j+1))
theta(j) = theta(j)*sol0(i-1)/sol0(i)
start = start - thick0(i)
stop = stop - thick0(i-1)
620 continue

700 continue
c   test whether iteration is within specified
c   agreement
if (dabs(theta(0) - th0) .lt. 0.005) goto 800

c   prepare for next iteration

```

```

710  continue
      IF (theta(0) .le. th0) THEN
          p2 = 1.
      ELSE
          p2 = -1.
      ENDIF
      iter2 = iter2/2
      theta(k-1) = theta(k-1) + (p2*iter2)
      n = n + 1
      IF (n .ge. 500) THEN
          write(6,*) ('solution not converging')
          stop
      ENDIF
      goto 600

800  continue
c    calculate rel(j) for each layer i as if that
c    layer i is at the surface; i.e., as if rel(0) = 1
c    for each layer.
      start = k
      stop = k-thick0(nl)+1
      do 820, i = nl,1,-1
          beta_i = beta0(i)*p_out/p_ref
          do 810, j = start,stop,-1
              rel(j) = (sol0(nl)/sol0(i)) *
*                 (theta(j) * (beta_i + 1.))/
*                 (beta_i * theta(j) * sol0(nl)/sol0(i) + 1.)
810  continue
          if (i .eq. 1) goto 820
          start = start - thick0(i)
          stop = stop - thick0(i-1)
820  continue
      rel(0) = (sol0(nl)/sol0(1)) *
*            (theta(0) * (beta_i + 1.))/
*            (beta_i * theta(0) * sol0(nl)/sol0(1) + 1.)
c    reset iteration counter
      n = 0
      write(6,*) 'Done'

c    write output to file
      open(10,file=fname)

1001 format(2x,i4,2x,f6.4,2x,f6.4)
1002 format(' P_in = ',f5.1,'; P_out = ',f5.1,';
* P_ref = ',f5.1)
1003 format(' Thickness = ',f5.2)
1004 format(' LAYER THICK PHI Pox SOL
* DENS BETA')
1005 format
* (3x,i4,3x,i4,3(2x,(1p,e8.2)),0p,3x,f5.2,3x,f5.2)
1006 format(/,' j theta rel')
      write(10,1002) p_in, p_out, p_ref
      write(10,1003) totl

```

```
        write(10,1004)
        do 1100, i = 1,nl
            write(10,1005) i,thick0(i), phi0(i), perm0(i),
*                sol0(i), dens0(i), beta0(i)
1100 continue

        write(10,1006)
        do 1200, i = 0,k,10
            write(10,1001) i/10, theta(i), rel(i)
1200 continue
        close(10)

        return
    end
```

APPENDIX 3

MODULUS PROFILER- NOTES AND BLOCK DIAGRAMS

Turn on the computer and associated equipment. At the DOS prompt type WIN and press Enter. Windows Program Manager appears. Use the left mouse button to click on the "LABTECH NOTEBOOK PRO" icon; the LABTECH icons appear. Click on the LABTECH Build-Time icon; the Build-Time screen opens. Click on File in the menu bar; click on Open (be careful to not click on any other items in this screen). Double click on "C:\\" folder in the Directories box. Press the down arrow (keyboard) until NBP WIN appears and double click on it. In the File name box double click on "30SECNE1.LTC". This is the Labtech program that runs the Surface Modulus Profiler. Icons will appear in the Build-Time window. The program is now ready to run. Ensure that the linear actuator screw that raises and lowers the probe and weight is located at its maximum height. (This only needs to be done for the initial installation). Do this by unscrewing it from the aluminum block that holds the weight hook. Continue unscrewing it (ccw) until it is as high as it will go. Raise the aluminum weight block threads to the screw. Continue turning the screw ccw while holding the weight block threads to the threads on the end of the screw until a click or detent is felt. This happens when the leading edge of the threads are ready to engage. At this point turn the screw cw and screw it into the weight block. This is the starting position for a test run. The probe can be raised and lowered manually by selecting UP or DOWN with the UP-AUTO-DOWN switch and then pushing the JOG switch momentarily. This is convenient when mounting a new sample or to reposition the probe if the test is prematurely terminated. To establish the vertical location of the sample make sure there is no sample mounted. Set the switch to DOWN or UP as needed and while pushing down gently on the probe weight tray push the JOG switch momentarily until the DVM reads as close to zero as possible. This is the "balanced" position that will provide enough probe travel while remaining in the linear range of the LVDT. Carefully (sample surface must be below the probe tip) mount a sample. Use the microscope and DVM to adjust the Z-axis micrometer until the sample surface just touches the probe tip. JOG the probe UP until it just clears the sample surface (approx. 10 mv on the DVM). Switch back to AUTO.

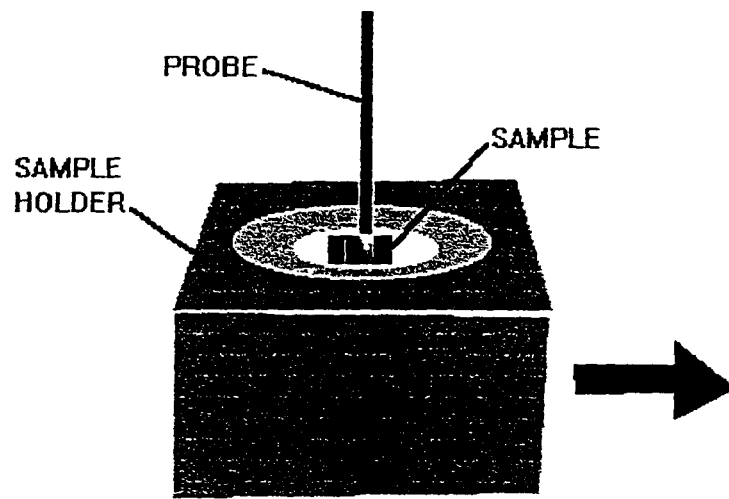
Ensure that the stepper (x axis) has enough travel to accommodate the thickness (span) of the sample. The stepper can be rotated manually. With the aid of the microscope position the sample just above the first data point on the right side of the sample. (The stepper motor moves the sample to the right; the last data point will be on the left side.) Use the X and Y micrometers on the XYZ stage to position the sample. Record the X axis micrometer reading. Rotate the stepper to the opposite side of the sample (the last data point) and record the reading. Subtract to get the total span of the sample. Return the stepper to the beginning position.

Using the left mouse button click on the RUN icon on LABTECH BUILD-TIME screen. The data display will appear (LABTECH VISION); wait until the display is complete - it will take a few seconds. Click and drag the SPAN slider until the digital display indicates the span that was measured then release the button. Click and drag the POINTS slider until the display indicates the number of points to be probed then release the button. Make certain that the MOTORS switch is on then click and hold on the red OFF button until it turns to green ON button. The probe motor will run and the probe will begin to move down. A solenoid will be pulsed to provide vibration to assist the descent of the probe. A trace (representing displacement of the probe in mils) will appear on the data display. The probe motor will run for 5 seconds then

stop for thirty seconds while the probe contacts the sample surface. The probe motor will then run for 5 seconds to lower the weight to the probe weight platform. The penetration of the probe can be seen on the data display. After 40 seconds the probe motor will run for 10 seconds to raise the weight and probe. It will remain off for 10 seconds while the sample stepper motor runs to position the sample at the next point, then the sequence repeats. Each sequence takes 100 seconds(or 100 seconds/point). When the test has ended the data display screen will be replaced by the RUNTIME screen. Manually return the stepper(x axis) to the beginning position to ensure that there is enough travel for the next run. The run can be terminated manually by clicking and holding on the green ON button until it turns to red OFF button. CAUTION: the solenoid may remain energized; switching the MOTORS switch off will disable it. CAUTION: the probe will probably need to be positioned manually to its starting position(approx. 18 mv on DVM).CAUTION: the stepper will probably have to be returned to its starting position.

Switch to File Manager and bring up c:\nbp_win.This is the directory where the data files are stored.Click on View in the menu bar then click on By File Type;enter *.prn(prn is the extension used by Labtech for data files) then click on OK. All of the .prn files will be displayed. The file name(prefix)will be MODPRO#.prn. The # is the file number supplied by Labtech and is incremented for each new test run so the highest # is the last test done. Ninety nine is the last # allowed since only 8 characters are available and the name "MODPRO" uses six of the eight. The name and count can be changed in the Labtech Build-Time screen by double clicking on the "1:MODPRO&.PRN" icon in the upper left hand corner of the screen. Click and drag down the NAME icon(upper left corner)and enter a new name in the LOG NAME box. Read the Help menu to learn about other options.

The data format is two columns of ASCII characters. The data may be reduced manually by selecting the mil value and time at which the weight was added and the mil value 30 seconds later. Enter these values into the equation for each data point acquired to generate the 30 second modulus of the sample. Software is available(Sigma-Plot,Excel etc.)to do this automatically.



SAMPLE MOVES TO THE RIGHT; THE FIRST POINT IS THE RIGHT SIDE OF THE SAMPLE.

BLOCK NAME	BIT #
------------	-------

PROBE DIR	7
-----------	---

UP-HI
DN-LO

PROBE LIFT	6
------------	---

ON-HI
OFF-LO

STEP DIR	5
----------	---

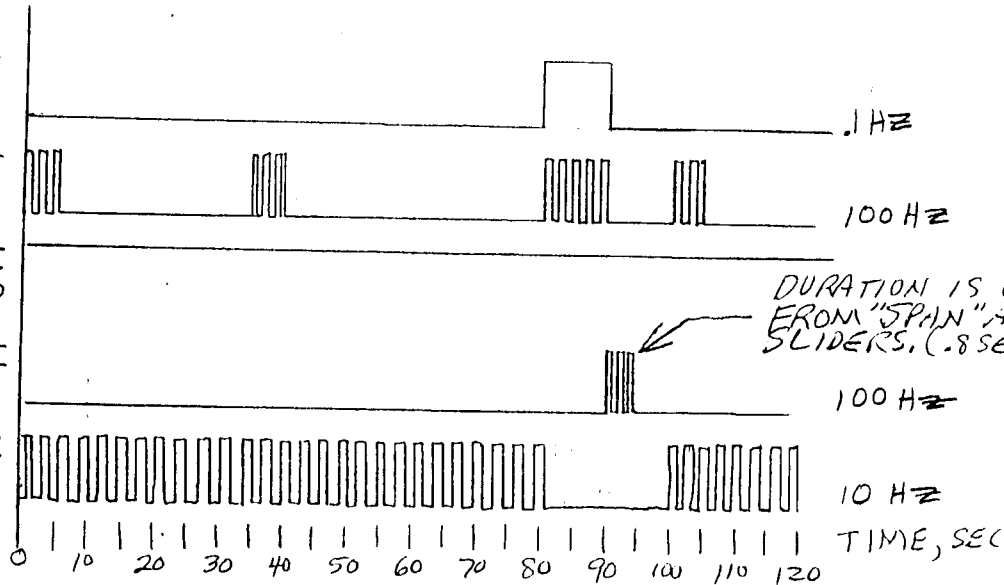
CCW-HI
CW-LO

STEP	4
------	---

ON-HI
OFF-LO

VIBE	3
------	---

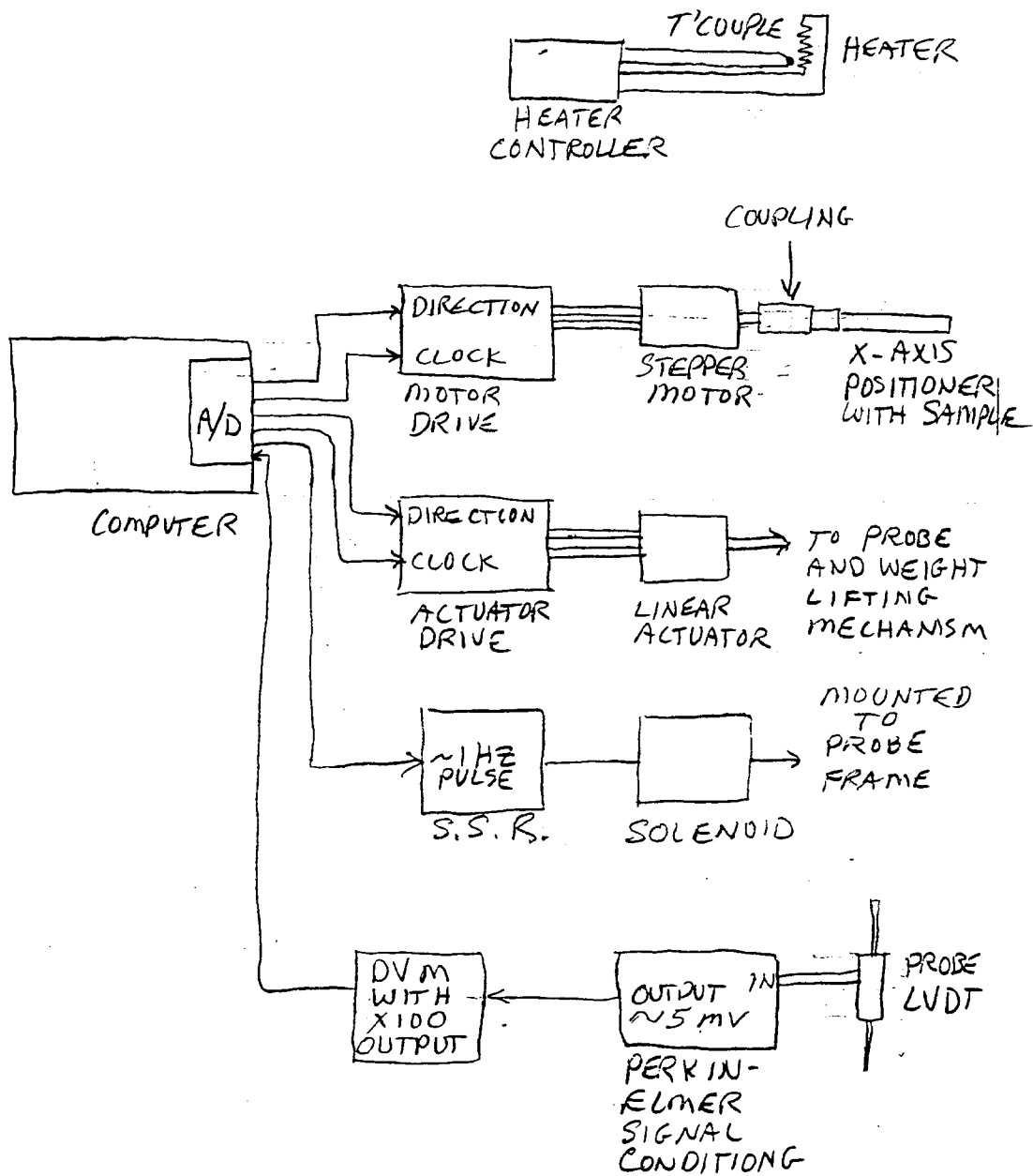
ON-HI
OFF-LO



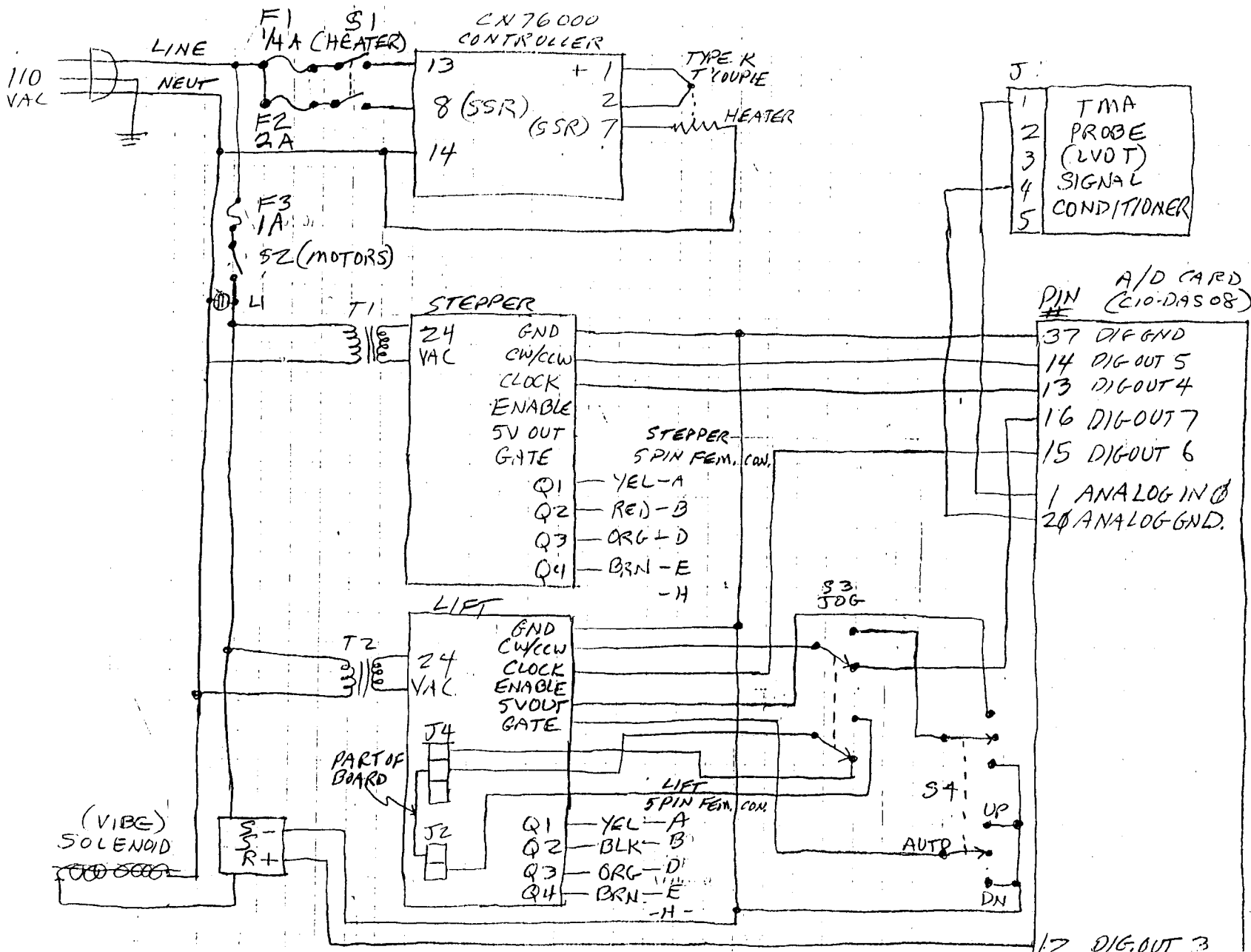
DURATION IS CALCULATED FROM "SPAN" AND "POINTS" SLIDERS. (.8 SEC @ 100HZ = .5min)

↑
100 SEC PER
SAMPLE POINT

MOTOR DRIVER TIMING



BLOCK DIAGRAM



Distribution

Former distribution in 1999 for SAND99-0465 under CRADA protection

1	MS1207	J. Wise, 5909
1	MS1407	P. Collins, 1811
1	MS1407	R.L. Clough, 1811
5	MS1407	K.T. Gillen, 1811
1	MS1435	A.K. Hays, 1800
3	MS9018	Central Technical Files, 8940-2
2	MS0899	Technical Library, 4916
2	MS0619	Review & Approval Desk, 15102 For DOE/OSTI
1	MS1380	Technology Transfer, 4212

Goodyear Distribution:

1	Al Causa
1	Dave Benko
1	Ed Terrill
1	John Lawrence
1	Dave Hargis
1	Library

The Goodyear Tire and Rubber Company
142 Goodyear Boulevard
Akron, OH 44305
Attention: Al Causa

New distribution in 2012 for SAND2012-7644

1	MS1411	Celina Mathias C.	1819
1	MS1411	Gillen, Kenneth T.	1819
1	MS0899	Technical Library	9536 (electronic copy)

